

In situ study of magnetocrystalline anisotropy in thin Fe films grown on GaAs (100) and (110)

Der Fakultät Physik
der Universität Duisburg-Essen
zur Erlangung des akademischen Grades
eines Doktors der Naturwissenschaften (Dr. rer. nat.)

vorgelegte Dissertation von

Babli Bhagat

aus Panna, India.

Tag der Disputation: 06.03.2023.

1. Gutachter: Prof. Dr. Michael Farle

2. Gutachter: Dr. Jürgen Lindner

“Religion is a culture of faith; science is a culture of doubt.”

— Richard P. Feynman

“I am inspired by those who have the courage to do things that have never been done before; things that were believed to be impossible.”

— Sandeep Maheshwari



Abstract

In this thesis, the growth, structure, magnetic anisotropy, g-factor, and Gilbert damping of thin Fe films grown on GaAs (110) and GaAs (100) are investigated using *in situ* ferromagnetic resonance (FMR), low energy electron diffraction, and Auger electron spectroscopy as a function of time, capping layer, and substrate doping. The time evolution of magnetic anisotropy and the surface morphology of uncapped Fe films of different thicknesses under ultra-high vacuum conditions is quantified. Reversal of in-plane uniaxial anisotropy as a function of time is observed at room temperature in 4 nm Fe/GaAs (110). While for other thicknesses, a gradual decrease of in-plane uniaxial anisotropy with time (1-5% per 24 hours for 1 and 2 nm) is observed. As the thickness of the film reduces, interface effects play a major role, and consequently, there is a lesser modification of magnetic anisotropy. On the other hand, Fe film grown on GaAs (100) having the same thickness of 4 nm shows a negligible change of magnetic anisotropy over time. It is demonstrated that the time stability of Fe film under vacuum conditions is correlated with the substrate orientation and the thickness.

The effect of Ag/Pt cap layers on the magnetic anisotropy, g-factor, and Gilbert damping parameter of 5 nm Fe film grown on GaAs (100) is studied. Angular-dependent and frequency-dependent ferromagnetic resonance measurements were performed to determine the mentioned properties. A significant reduction of the out-of-plane anisotropy (78%) is observed after capping Fe with Ag and Pt. The surface anisotropy and spin-orbit coupling are modified after capping Fe with Ag, which in turn alters the magnetic properties of laying Fe film. It is illustrated that the change in the Gilbert damping is correlated with the simple model proposed by Grate, which describes a proportional relation between Gilbert damping parameter ' α ' and density of states of ferromagnetic film. Uncapped Fe film showed an enhanced g-factor (3.7%) with respect to bulk Fe in [100] direction due to increased orbital moment at the surface. The Ag capping layer significantly suppresses the surface states, and the g-factor is reduced to bulk value ($g = 2.09$). The capping with the heavy metal Pt even after 2 nm of Ag can modify the magnetic relaxation mechanism by spin pumping (injecting pure spin current from Fe into Pt) since the spin diffusion length of

Ag is very high (132-152 nm) [1]. All these effects occurring at the Pt/Ag/Fe interface ultimately amend the electronic structure of Fe film, tailoring the magnetic anisotropy, g-factor, and damping mechanism.

Finally, the Pt/Ag/Fe/GaAs (110) heterostructure was studied for three different doping types of GaAs substrate (undoped, p-doped, and n-doped) using *ex situ* FMR. The influence of substrate doping on the magnetic properties, e.g., magnetic anisotropy, g-factor, and Gilbert damping, is determined using an angular- and frequency-dependent FMR. It is verified that the type of doping inside substrate can determine the deviation of magnetic properties of ferromagnetic film grown on top of it. The in-plane uniaxial anisotropy is significantly changed (55-85%) with the type of substrate doping. On the other hand, no dependence of the g-factor on the type of doping was found in these heterostructures. In addition, the intrinsic damping or ' α ' was found to be reduced by 20% in the p-doped sample with respect to the undoped sample. The origin of these minor effects might be due to spin-orbit interaction at Fe/substrate interface, which is modified after doping the substrate. The electronic property of the semiconductor is directly affected by the doping concentration, and this can alter the electronic structure at Fe/GaAs interface resulting in the change of Gilbert damping.

Zusammenfassung

In dieser Arbeit werden das Wachstum, die Struktur, die magnetische Anisotropie, der g-Faktor und die Gilbert-Dämpfung von dünnen Fe-Filmen, die auf GaAs (110) und GaAs (100) gewachsen sind, mit Hilfe von *in situ* ferromagnetischer Resonanz (FMR), Niederenergie-Elektronenbeugung und Auger-Elektronenspektroskopie als Funktion der Zeit, der Deckschicht und der Substratdotierung untersucht. Die zeitliche Entwicklung der magnetischen Anisotropie und der Oberflächenmorphologie von ungedeckten Fe-Filmen unterschiedlicher Dicke unter Ultrahochvakuumbedingungen wird quantifiziert. Die Umkehrung der in-plane uniaxialen Anisotropie als Funktion der Zeit wird bei Raumtemperatur in 4 nm Fe/GaAs (110) beobachtet. Bei anderen Schichtdicken ist eine graduelle Abnahme der in-plane uniaxialen Anisotropie mit der Zeit zu beobachten (1-5 % pro 24 Stunden für 1 und 2 nm). Mit abnehmender Schichtdicke spielen die Grenzflächeneffekte eine größere Rolle, so dass sich die magnetische Anisotropie weniger stark verändert. Andererseits zeigt ein Fe-Film, der auf GaAs (100) mit derselben Dicke von 4 nm gewachsen ist, eine vernachlässigbare Änderung der magnetischen Anisotropie im Laufe der Zeit. Es wird gezeigt, dass die Zeitstabilität des Fe-Films unter Vakuumbedingungen mit der Substratorientierung und der Dicke korreliert.

Die Wirkung von Ag/Pt-Deckschichten auf die magnetische Anisotropie, den g-Faktor und den Gilbert-Dämpfungsparameter von 5 nm Fe-Film, der auf GaAs (100) gewachsen ist, wird untersucht. Es wurden winkelabhängige und frequenzabhängige ferromagnetische Resonanzmessungen durchgeführt, um die genannten Eigenschaften zu bestimmen. Eine signifikante Verringerung der out-of-plane Anisotropie (78%) wird nach der Beschichtung von Fe mit Ag und Pt beobachtet. Die Oberflächenanisotropie und die Spin-Bahn-Kopplung werden nach der Bedeckung von Fe mit Ag verändert, was wiederum die magnetischen Eigenschaften des Fe-Films verändert. Es wird gezeigt, dass die Veränderung der Gilbert-Dämpfung mit dem einfachen Modell von Grate korreliert, das eine proportionale Beziehung zwischen dem Gilbert-Dämpfungsparameter α und der Zustandsdichte des ferromagnetischen Films beschreibt. Der nicht abgedeckte Fe-Film zeigte einen erhöhten g-Faktor (3,7 %) in Bezug auf das Fe-Volumen in [100]-Richtung aufgrund des erhöhten

Bahnmoments an der Oberfläche. Die Ag-Deckschicht unterdrückt die Oberflächenzustände erheblich, und der g-Faktor wird auf den Bulk-Wert reduziert ($g=2,09$). Die Bedeckung mit dem Schwermetall Pt kann sogar nach 2 nm Ag den Mechanismus der magnetischen Relaxation durch Spin-Pumping (Injektion von reinem Spinstrom aus Fe in Pt) verändern, da die Spindiffusionslänge von Ag sehr groß ist (132-152 nm) [1]. All diese Effekte, die an der Pt/Ag/Fe-Grenzfläche auftreten, verändern letztendlich die elektronische Struktur des Fe-Films und passen die magnetische Anisotropie, den g-Faktor und den Dämpfungsmechanismus an.

Schließlich wurde die Pt/Ag/Fe/GaAs (110)-Heterostruktur für drei verschiedene Dotierungstypen des GaAs-Substrats (undotiert, p-dotiert und n-dotiert) unter Verwendung von *ex situ* FMR untersucht. Der Einfluss der Substratdotierung auf die magnetischen Eigenschaften, wie die magnetische Anisotropie, den g-Faktor und die Gilbert-Dämpfung, wird mit winkel- und frequenzabhängige FMR bestimmt. Es wird nachgewiesen, dass die Art der Dotierung im Substrat die Abweichung der magnetischen Eigenschaften des darauf gewachsenen ferromagnetischen Films bestimmen kann. Die in-plane uniaxiale Anisotropie wird durch die Art der Substratdotierung erheblich verändert (55-85%). Andererseits wurde bei diesen Heterostrukturen keine Abhängigkeit des g-Faktors von der Art der Dotierung festgestellt. Darüber hinaus wurde festgestellt, dass die intrinsische Dämpfung oder " α " in der p-dotierten Probe um 20 % geringer ist als in der undotierten Probe. Der Ursprung dieser geringfügigen Effekte könnte auf die Spin-Bahn-Wechselwirkung an der Fe/Substrat-Grenzfläche zurückzuführen sein, die nach der Dotierung des Substrats verändert wird. Die elektronische Eigenschaft des Halbleiters wird direkt von der Dotierungskonzentration beeinflusst, und dies kann die elektronische Struktur an der Fe/GaAs-Grenzfläche verändern, was zu einer Änderung der Gilbert-Dämpfung führt.

Declaration

I, Babli Bhagat, hereby submit my dissertation on the topic:

In situ study of magnetocrystalline anisotropy in the thin Fe films grown on GaAs (100) and (110)

for the award of the academic degree of Doctor of Natural Science (Dr. rer. nat.). I hereby declare that I have written the submitted dissertation independently using only the materials listed and have cited all sources taken over verbatim or in content as such. I hereby declare that I have not submitted this dissertation for any other doctoral procedures.

Duisburg, 06.03.2023

Babli Bhagat



Acknowledgments

I want to express my gratitude and appreciation to all the persons who contributed directly or indirectly to the completion of this thesis.

First of all, I am grateful to Prof. Dr. Michael Farle, who gave me the opportunity to do my doctoral studies under his supervision. I would like to thank him for his constant support and guidance throughout all these years. Furthermore, I am very thankful to him for continuing my employment during the last year to finish my PhD thesis.

I am thankful to Dr. Florian Römer for inviting me to a research position and training at the UHV chamber. You taught me how to deal with such a complicated high vacuum chamber and conquer over the problems at the same time during non-stop failures.

I acknowledge the financial support from the German Research Foundation (DFG) projects RO 5030/2-1, 405553726 (CRC/TRR 270), and the University of Duisburg-Essen. Moreover, I would like to express my sincere thanks to our secretaries Mrs. Helga Mundt and Mrs. Sabina Grubba, for instant help in all administrative matters, especially in understanding German documents.

My dearest thanks go to the most helpful person during my PhD, Dr. Anna Semisalova, for her never-ending support, help, and guidance. Your immense encouragement and enthusiasm concerning my PhD and laboratory work pushed me to survive for research. You always supported me and my work over the last years and always took time to read and discuss my data and helped in analyzing and correcting my writing. Thank you for all the time we spent together. You are a great friend and a lovely supervisor.

I am very thankful to Dr. Ralf Meckenstock for fruitful discussions and insightful comments on my data. I have learned a lot from you regarding FMR data interpretation and Fe films. Without your expert advice, I could not publish the AIP paper.

My special thank goes to Dr. Detlef Spoddig for technical support in the laboratory. I learned a lot from you concerning the technical details of various lab equipment. Thank you for your moral support during my PhD. I am also grateful to Dipl. Ing. Michael Vennemann and Philipp Kükenbrink for helping during my experiments regarding engineering and mechanical aspects.

I would like to thank my colleagues, namely Tanja Strusch, Benjamin Zingsem, Dr. Ulf Wiedwald, Paul Wendtland, Thomas Feggeler, Irene Iglesias, Iuliia Novoselova, Dr. Marina Spasova, for their personal and professional support throughout my PhD. Thank you all for your encouragement, enthusiasm, and friendly help all the time. I would also thank Prof. i.r. Dr. Mehmet Acet, for your great comments during my talks. You are an inspiration to me. Thank you, Dr. Ulf, and Merve for the AFM measurements.

My dearest gratitude goes to my parents Dolly and Deep Raj Bhagat, for supporting me in my life decisions and allowing me to pursue my dreams in my way. Thank you for all your love and care. Thank you for believing in me and being always there by my side in all situations of life. Your nourishment and upbringing have brought me here.

Last but not the least, I am immensely thankful to the most wonderful person in my life, my husband, Manish Verma. Without your overwhelming support, love, care, and motivation, this thesis or my PhD work would not have been possible. I cannot imagine my time at Duisburg without you. Thank you very much for being a great friend and counsellor of mine for the rest of my life. Thank you so much for understanding me like no other, believing in me no matter what, accepting me what I am, and guiding me at every step. I would also thank my in-laws, Dr. Kanik Ram and Mrs. Purnima Singh, and my brother-in-

law, Ankit Verma, for their support and love during my Ph.D. and thesis writing. I am lucky to have you all.

Abbreviations

AES	Auger Electron Spectroscopy
AFM	Atomic Force Microscopy
BCC	Base-Centered Cubic
BLS	Brillouin Light Scattering
CMA	Cylindrical Mirror Analyser
CPW	Coplanar Waveguide
DC	Direct Current
DFT	Density Functional Theory
EPR	Electron Paramagnetic Resonance
FCC	Face-Centered Cubic
FM	Ferromagnet
FMR	Ferromagnetic Resonance
FWHM	Full Width at Half Maximum
GMR	Giant Magnetoresistance
IGP	Ion Getter Pump
LEED	Low Energy Electron Diffraction
LLG	Landau-Lifshitz-Gilbert equation
MAE	Magnetic Anisotropy Energy
MBE	Molecular Beam Epitaxy
ML	Monolayer
MOKE	Magneto-Optic Kerr Effect
PID	Proportional-Integral-Derivative
PSPD	Position-Sensitive Photodiode
RHEED	Reflection High-Energy Electron Diffraction
RT	Room Temperature
SC	Semiconductor
SEM	Scanning Electron Microscopy
SOC	Spin-Orbit Coupling
SQUID	Superconducting Quantum Interference Device
STM	Scanning Tunneling Microscopy

TMR	Tunneling Magnetoresistance
TSP	Titanium Sublimation Pump
UHV	Ultra-High Vacuum
XMCD	X-ray Magnetic Circular Dichroism
XRD	X-ray Diffraction

Table of Contents

1	Introduction	1
2	Fundamentals.....	7
2.1	Magnetic anisotropy	7
2.1.1	Intrinsic anisotropy	8
2.1.2	Dipole-dipole interaction.....	9
2.2	Landau-Lifshitz-Gilbert equation	13
2.3	Ferromagnetic resonance	15
2.4	Magnetic relaxation	18
2.4.1	Gilbert damping.....	20
2.4.2	Two-magnon scattering	21
3	Experimental techniques and methodology	24
3.1	UHV set-up.....	24
3.2	Advantages and limitations of the UHV system.....	27
3.3	In situ Techniques.....	29
3.4	Ex situ techniques	34
3.4.1	Atomic force microscopy (AFM).....	34
3.4.2	Ex situ FMR.....	36
4	Structural and magnetic characterization of Fe on GaAs (100) and GaAs (110) as a function of time	38
4.1	Introduction.....	38
4.2	Sample Preparation	39
4.3	Time-dependent structural and magnetic stability of Fe/GaAs (110)	40
4.4	Magnetic anisotropy as a function of time in Fe/GaAs (110)	52
4.5	Time-dependent structural and magnetic stability of Fe/GaAs (100)	54
4.6	Comparison of Fe (100) and Fe (110)	58
5	Influence of capping layer on the magnetic properties of Fe/GaAs (100)..	60
5.1	Fabrication and characterization of the sample	60
5.2	Magnetic anisotropy with and without capping layer	64

5.3	Frequency-dependent FMR measurements and g-factor	70
5.4	Effect of capping layer on relaxation mechanism (Gilbert damping)....	74
5.5	Summary.....	78
6	Influence of substrate doping on the magnetic properties of Pt/Ag/Fe/GaAs (110) heterostructure	80
6.1	Introduction	80
6.2	Sample growth and structural characterization	81
6.3	Magnetic anisotropy of Pt/Ag/Fe/GaAs (110) heterostructure	84
6.4	Magnetic relaxation (Gilbert damping).....	89
6.5	Summary.....	93
7	Conclusion and outlook	94
8	Appendix	98
8.1	Magnetocrystalline anisotropy of Fe films.....	98
9	List of Figures	102
10	List of Tables	107
11	Bibliography	108
12	List of publications and conference contributions	117

1 Introduction

Over the last three decades, the interest in ferromagnetic-semiconductor heterostructures has raised dramatically not only for the fundamental understanding of magnetism in ultrathin films but also for spintronics devices [2-6]. The discovery of several phenomena in ultrathin ferromagnetic films such as giant magnetoresistance (GMR), tunneling magnetoresistance (TMR), and spin injection has led to the development of new device concepts [7-9]. Fe/GaAs heterostructure is considered a promising candidate and has been extensively studied so far for spintronics devices. Formation of the Schottky tunnel barrier across the Fe/GaAs interface [10] enables spin injection leading to the development of spin transistors [11] and spin light-emitting diodes [12]. In addition, a robust spin-orbit torque found at a single crystalline Fe/GaAs (001) interface at room temperature [13], enabling spin-to-charge current conversion, facilitates efficient electrical magnetization manipulation.

Furthermore, this large spin-orbit fields at the Fe/GaAs (001) interface can be controlled with an electric field [14], which means that the electric field in a Schottky barrier can modify spin-orbit magnetic fields. The latter effect can be utilized in developing spin-orbit torque devices with low power consumption. A unique feature of the Fe/GaAs system from a fundamental point of interest is the observation of in-plane uniaxial anisotropy along with four-fold cubic anisotropy, which gives rise to spin reorientation in ultrathin films [15, 16]. The observation of anisotropic Gilbert damping in ultrathin Fe/GaAs (001) films [17, 18] is another distinctive property that helps to understand the magnetization relaxation mechanism in such systems.

GaAs is a compound semiconductor having a zinc blende cubic structure ($a_{\text{GaAs}} = 5.65 \text{ \AA}$), as shown in Figure 1.1 with a direct bandgap of 1.4 eV at 300K. GaAs (001) surface exhibits a wide range of reconstructions involving significant rearrangement of surface atoms, determining the surface and subsequent film properties. On the contrary, GaAs (110) surface shows no surface reconstruction but rather a bulk-like termination with zigzag chains of alternating Ga and As atoms and dangling bonds. GaAs (100) surface can be either Ga- or As-terminated depending on the substrate preparation. GaAs (001)

reconstructions can be pretty complex, and only a few surface science techniques are sensitive enough to precisely determine atomic arrangements in

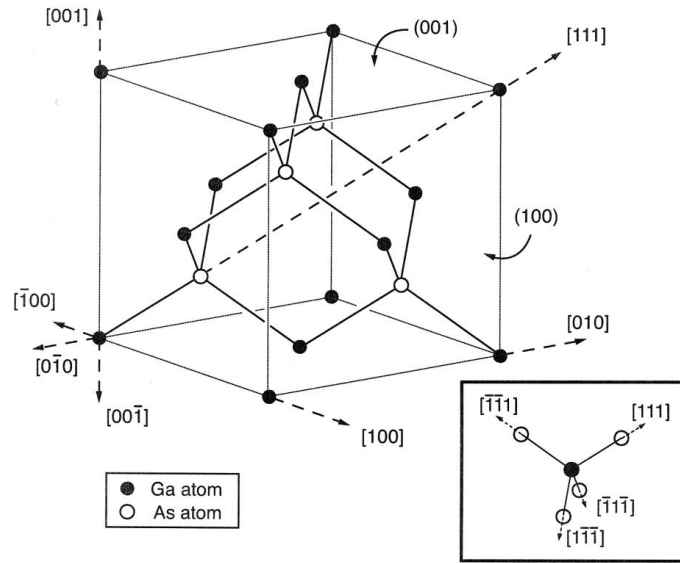


Figure 1.1 Zinc blende crystal structure of GaAs showing crystallographic directions and planes. The inset details the directions of the tetrahedral bonds on a Ga atom (taken from [19]).

surface/subsurface layers. Several reconstructions may have the same surface periodicity making them almost indistinguishable by techniques like low-energy electron diffraction (LEED) and reflection high energy electron diffraction (RHEED). In such cases, scanning tunneling microscopy (STM) studies are indispensable to determine the surface structure reliably. Domains of different reconstructions may coexist on a sample, especially if they are close in energy [19].

Fe is a ferromagnetic metal having a BCC structure ($a_{\text{Fe}}=2.87 \text{ \AA}$) with a Curie temperature of $770 \text{ }^\circ\text{C}$. In bulk α -Fe at room temperature, the saturation magnetization M_s is 1714 kA/m and a magnetic moment of $2.22 \mu_B$ per atom. The magnetic easy, intermediate, and hard axis lies along $\langle 001 \rangle$, $\langle 011 \rangle$, and $\langle 111 \rangle$ directions, respectively. Since the atomic magnetic moments depend on the atomic coordination and hybridization, the magnetic moment of thin films significantly differs from the respective bulk value. For example, Fe films deposited on GaAs (001) substrate can exhibit a significantly reduced average magnetic moment due to intermixed interfacial layer and As out-diffusion [20].

The epitaxial growth of Fe film on GaAs (100) was first reported by Waldrop and Grant [21]. They attributed this epitaxial growth to the fact that the lattice mismatch between Fe and GaAs is only 1.4%. However, this lattice mismatch also gives rise to epitaxial strain at the interface causing tetragonal distortions in the Fe film. Welder et al. [22] showed the evolution of stress during the epitaxial growth of Fe film on GaAs (001). Their results indicate additional tensile interface stress with compressive misfit stress, which increases with film thickness and falls in thicker films.

The reconstruction of the GaAs substrate depending on the different arrangement of the surface atoms significantly affects the initial growth and morphology of Fe film grown on it. Ga-rich surface, e.g. (4x6), c(8x2), (4x2) reconstructed GaAs (001), and GaAs (110) follow Volmer-Weber growth where nucleation of 3D islands due to large interface energy proceeds with quasi-layer-by-layer growth. On the other hand, in As-rich surfaces, e.g., α -(2x4) and c-(4x4), the growth proceeds via nucleation of 2D islands followed by layer-by-layer growth. Depending on the growth temperature and GaAs surface reconstruction, the Fe-As-Ga compound or intermediate layer is formed at the interface [23]. The width of this intermixed or reacted layer, also called the dead layer (no magnetization), increases with substrate temperature during growth, and its lattice constant is larger than both a_{Fe} and a_{GaAs} [24]. Theoretical calculations show that for low coverages Fe atoms prefer bonding with As over Ga, and Fe atoms prefer to be highly coordinated [25].

The out-diffusion and surface segregation during Fe deposition on GaAs (001) was reported by Sano and Miyagawa [26], where they measured AES intensities as a function of Fe film thickness and substrate temperature (300-573 K). Their findings indicate diffusion of both Ga and As atoms from the substrate and segregation on the film surface, but As is more pronounced than Ga at the same substrate temperature. However, they also claimed that this segregation could be easily removed by sputter etching, and re-segregations do not occur after that. Theoretical studies suggest that As out-diffusion or segregation can occur even at 0 K, while Ga out-diffusion or segregation only occurs at higher temperatures [27].

Xu et al. [28] first proposed the evolution of the ferromagnetic phase in ultrathin Fe films grown on GaAs (100)-4x6. They suggested that the initial growth of Fe film up to 3.5 ML thickness proceeds in the nucleation of small, isolated islands, giving a non-magnetic phase. However, these islands grow continuously in 3D mode to form bigger clusters, and

the exchange interaction within these clusters is strong enough, leading to internal ferromagnetic ordering, which leads to the superparamagnetic phase. This superparamagnetic phase is present for the thickness up to 4.4 ML (see Figure 1.2). After this thickness, the clusters coalesce together to form a continuous film with a long-range ferromagnetic order confirmed by the appearance of a clear LEED pattern at 6 ML. This indicates that the transition from superparamagnetism to ferromagnetism is a percolation phase transition within the film.

The magnetic anisotropy of bulk Fe is dominated by cubic anisotropy ($4.7 \times 10^4 \text{ J/m}^3$). However, with decreasing thickness of Fe film, it is generally found that the uniaxial anisotropy contribution becomes dominant over a four-fold cubic contribution. This uniaxial anisotropy in the initial stages (~ 8 ML) of film growth mainly arises from interfacial mechanism (surface reconstruction of GaAs), giving uniaxial easy axis along [110] direction for Fe/GaAs (001). The superposition of uniaxial anisotropy on cubic anisotropy in ultrathin limit causes in-plane reorientation of the easy and hard axis. This reorientation occurs below a critical thickness of 6-8 ML for Fe/GaAs (001) [16, 29] and 20-24 ML for Fe/GaAs (110) [15].

Several *in situ* studies have been performed to analyze the structural and magnetic properties of uncapped Fe films grown on GaAs (001) and GaAs (110) [30, 31]. Gillingham et al. [32] reported smoothening of uncapped Fe islands grown on GaAs (100) over 30 hours. On the contrary, Godde et al. [30] did not find a change in the surface morphology of either (001) or (110) uncapped Fe films grown at room temperature over 40 hours after deposition. These contradictory results on the same system can arise from different procedures applied during substrate preparation (the pressure during deposition is not mentioned for both samples). Secondly, the thickness range where smoothening was observed was far below one for the films in which no change in the surface morphology is reported. Therefore, it is crucial to understand the stability of surface morphology within different thickness range to know the critical thickness where the film surface is not affected over time. Furthermore, the influence of these time-dependent changes occurring on the film surface on the magnetic properties of Fe has never been measured under UHV conditions. Therefore, in this thesis the structural and magnetic properties of Fe film of different thickness grown on GaAs (100) and GaAs (110) as a function of time under UHV conditions at room temperature has been measured using LEED, AES and FMR. It has been found that Fe film sustains its crystal

structure at room temperature with time on both substrate orientations. However, the magnetic stability of Fe/GaAs (110) is affected, while Fe/GaAs (100) remains magnetically stable over time period of several tens of hours.

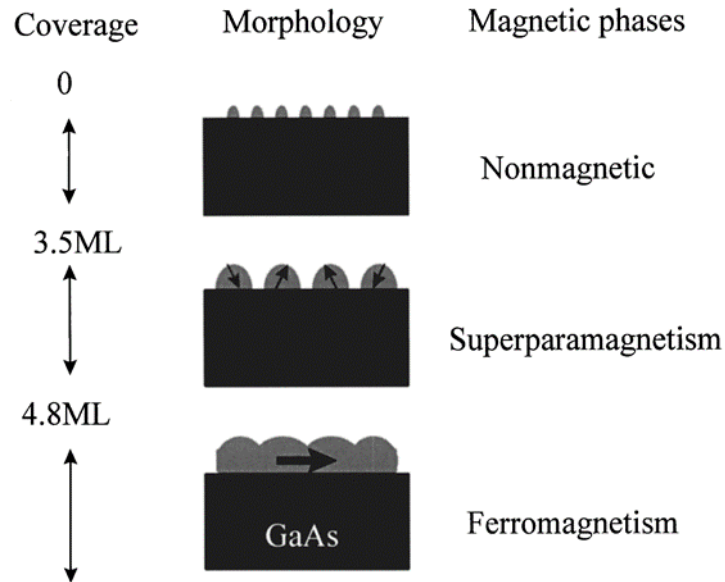


Figure 1.2 Correlation between the coverage, morphology, and magnetic phase of Fe films grown on GaAs (001)-4x6 substrate at room temperature [28].

A variety of experimental studies were carried out on capped Fe thin films using *ex situ* techniques [17, 33, 34], and few works were performed on uncapped Fe films using *in situ* techniques [31, 35, 36]. Therefore, it is necessary to study the same sample with and without the capping layer *in situ* under vacuum conditions to understand the influence of non-magnetic or metal capping on the magnetic properties of Fe film. Therefore, a 5 nm Fe film grown on GaAs (100) with and without capping layer has been measured *in situ* by FMR to study the influence of the capping layer on the magnetic anisotropy, g-factor, and damping of Fe film. These measurements reveal a significant change in the surface anisotropy of Fe film after capping with Ag and Pt. Furthermore, the magnetic relaxation, including different damping contributions (intrinsic and extrinsic), also changes with Ag and Pt capping.

Finally, the Pt/Ag-capped Fe films grown on GaAs (110) substrate with different doping of GaAs were studied using *ex situ* FMR. The influence of substrate doping on the magnetic anisotropy and damping of Pt/Ag/Fe/GaAs (110) heterostructure was observed by

measuring multifrequency FMR up to 40 GHz. A significant modification of in-plane uniaxial magnetic anisotropy has been observed in doped substrate sample with respect to undoped sample. Although the g-factor was found to be isotropic (no dependence on the type of doping), Gilbert damping showed a small change with substrate doping at different crystallographic directions of the film.

The thesis is organized as follows: **Chapter 2** includes the theoretical aspects of the magnetic anisotropy and magnetization dynamics to provide a relevant background for this thesis. **Chapter 3** provides a short overview of the different experimental techniques which have been utilized during this work. The experimental results and discussion of structural and magnetic characterization of Fe/GaAs (100) and Fe/GaAs (110) as a function of time at different thicknesses are presented in **chapter 4**. It also compares the time-dependent magnetic stability of Fe/GaAs (100) and Fe/GaAs (110) systems. The influence of the capping layer on the magnetic properties of Fe/GaAs (100) is discussed in **chapter 5**. **Chapter 6** presents the effect of substrate doping on the structural, chemical, and magnetic properties of Pt/Ag/Fe/GaAs (110) heterostructure. Finally, **chapter 7** conveys the major conclusions of the work and gives a short future outlook.

2 Fundamentals

In this chapter, the fundamental aspects of ferromagnetism in thin magnetic structures relevant to the analysis of the experimental results obtained in this thesis are summarized. First, the different contributions to the magnetic anisotropy are discussed. Then, the equation of motion, which describes the precession of magnetization M around an effective magnetic field, is explained. Finally, the different contributions of the magnetic damping to the relaxation mechanism and its relation to the ferromagnetic resonance linewidth are described.

2.1 Magnetic anisotropy

Magnetic anisotropy is the dependence of magnetic properties on the direction of the applied field with respect to the crystal lattice. Depending on the orientation of the applied field with respect to the crystal lattice, lower or higher energy in the form of the magnetic field is required to reach saturation magnetization. For example, for BCC Fe, the lowest density of atoms is in the $\langle 100 \rangle$ direction, and consequently $\langle 100 \rangle$ is the easy axis. In contrast, the atomic density is highest in $\langle 111 \rangle$ direction, and consequently $\langle 111 \rangle$ is the hard axis. In between the easy, and the hard axis, there lies an intermediate axis in $\langle 110 \rangle$ direction. The magnetization is not necessarily parallel to the applied field unless H is applied in an easy axis. The magnetization direction is given by the equilibrium condition, where the total energy of the material is minimal. The magnetic anisotropy energy (MAE) is the energy to rotate the magnetization of a single magnetic domain from its easy axis to the hard axis. In general, the magnetic anisotropy can be generated from the shape of the sample or can be induced by an external means e.g., during film growth, applying field during deposition, by irradiation, from substrate lattice mismatch, etc. The MAE is typically a small contribution on the order of a few $\mu\text{eV}/\text{atom}$ to the total (several eV/atom) of a cubic crystal [37]. The physical origin of the magnetic anisotropy energy is the interaction of the mean exchange field and the orbital moment of the atoms in the lattice. This is referred to as spin-orbit coupling. The only other mechanism responsible for the creation of magnetic

anisotropy is the dipole-dipole interaction which is responsible for shape anisotropy. It depends entirely on the sample shape.

Let's assume a small ferromagnet (single domain), inside which all the magnetization is pointing in the same direction. The energy of this ferromagnetic material in the absence of an external field is dominated by anisotropy energy described by:

$$E_a = K \sin^2 \theta \quad (2.1)$$

where K is the anisotropy constant with a unit of energy per unit volume (J/m^3), and θ is the angle between the magnetization M and easy axis. Now when the external magnetic field H is applied to the ferromagnet, the magnetization is pulled towards the field direction. Therefore, the total energy of the magnetization is given by

$$E = K \sin^2 \theta - \mu_0 MH \cos(\phi - \theta) \quad (2.2)$$

where $(\phi - \theta)$ is the angle between H and M .

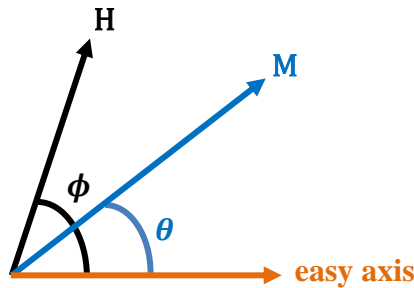


Figure 2.1 Schematic drawing of magnetization, applied field, and easy axis for a material.

2.1.1 Intrinsic anisotropy

The direct source of magnetic anisotropy is the spin-orbit coupling, which couples the spin to the orbital motion of an electron in a crystal structure. This coupling is generally a weak interaction. When the spin is reoriented by applying an external magnetic field, the orbit also tries to orient. However, the orbit resists rotating the spin axis due to the strong

interaction between orbit and lattice. The energy required to overcome this spin-orbit coupling, i.e., rotate the spin system from its easy axis, is called the anisotropy energy. The orbital angular momentum for 3d ions in a perfect cubic crystal is quenched. The magnitude of the spin-only moment is $m = g\mu_B S$, with $g = 2$. However, in thin films, a significant orbital moment appears due to reduced symmetry of the distorted lattice, which contributes to the spin-orbit coupling and, consequently, the anisotropy energy of the system.

The spin-orbit interaction leads to a coupling between magnetization and the atomic lattice of the material. Therefore, the interaction varies accordingly to the crystal structure. It is shown by a perturbation theory approach [38] that the anisotropy energy is proportional to the difference of orbital moment $\Delta\mu_L$ in easy and hard direction:

$$MAE = \phi \frac{\xi}{4\mu_B} |\mu_{L \text{ easy}} - \mu_{L \text{ hard}}| \quad (2.3)$$

where the parameter ϕ depends on the band structure and the magnitude of the orbital moment, ξ is the spin-orbit coupling constant.

2.1.2 Dipole-dipole interaction

Another source of magnetic anisotropy is the interaction between magnetic dipole moments μ_i and μ_j placed at a distance of r_{ij} given by:

$$E_{\text{dip}} = \left(\frac{\vec{\mu}_i \cdot \vec{\mu}_j}{r_{ij}^3} - \frac{3(\vec{r}_{ij} \cdot \vec{\mu}_i) \cdot (\vec{r}_{ij} \cdot \vec{\mu}_j)}{r_{ij}^5} \right) \quad (2.4)$$

The second term in equation 2.4 shows that the dipole energy depends on the orientation of the magnetic moment with respect to the distance between them. The dipole energy is the lowest when the magnetization M points parallel to r_{ij} and it costs energy to rotate the two dipole moments perpendicular to the r_{ij} axis. Shape anisotropy derives from the demagnetization field, which depends on the geometry of the sample. The demagnetizing

fields originate from a non-spherical sample where it is easier to magnetize along a long axis than a short axis. The demagnetization field H_d in a simple case for an ellipsoid can be expressed as:

$$H_d = -\mathcal{N}_{ij}M, i, j = x, y, z \quad (2.5)$$

where \mathcal{N}_{ij} is the demagnetizing tensor, which is generally represented by a symmetric 3×3 matrix with diagonalized \mathcal{N} ($\mathcal{N}_x + \mathcal{N}_y + \mathcal{N}_z = 1$). The magnetic anisotropy can be induced by applying stress or by depositing or annealing the sample in a magnetic field to create a micro-scale texture. The magnitude of the stress-induced anisotropy is $K_{u\sigma} = \frac{3}{2}\sigma\lambda_s$, where σ is the uniaxial stress and λ_s is the saturation magnetostriction ($\lambda_s \approx -7 \times 10^{-6}$ for Fe) [39]. The effect of tension on a single crystal or a thin film is to create a preferred direction of magnetization parallel to the direction of applied stress. A small strain may give rise to a significant anisotropy contribution. Therefore, it becomes more important in epitaxial structures, where film and the substrate have slightly different lattice parameters. The lattice mismatch between film and the substrate gives rise to a significant uniaxial anisotropy in thin films, specifically in the ultrathin limit.

The magnetic anisotropy energy density

Phenomenologically, the easy direction of magnetization is determined by minimizing the free energy density F , which is expressed as:

$$F = F_{zee} + F_{an} + F_d + F_{coupl} + F_{m.e.} \quad (2.6)$$

where F_{zee} is the Zeeman energy, F_{an} is the anisotropy energy density, F_d is the demagnetization energy as described by equation (2.5), F_{coupl} is the exchange energy which is connected to the spatial inhomogeneity of the magnetization, and $F_{m.e.}$ is the magneto-elastic energy, which is a function of the direction of the magnetization and the stresses. Zeeman part is generated by an external magnetic field $F_{zee} = -\vec{M} \cdot \vec{B}$. For a cubic crystal, the anisotropy energy density in terms of the power of directional cosines can be written as:

$$F_{cub} = K_0 + K_4(\alpha_1^2\alpha_2^2 + \alpha_1^2\alpha_3^2 + \alpha_2^2\alpha_3^2) + K_6(\alpha_1^2\alpha_2^2\alpha_3^2)$$

(2.7)

Here K_0, K_4 , and K_6 are the anisotropy constants and $\alpha_i = \left(\frac{M_i}{M}\right)$ $i = 1,2,3$ is the directional cosines with M_i as the projection of magnetization on the i^{th} crystal axis. K_0 being the isotropic part is generally neglected, and only higher-order terms are considered. If all the directional cosines are expressed in spherical coordinates

$$\alpha_1 = \sin \theta \cos \phi,$$

$$\alpha_2 = \sin \theta \sin \phi, \text{ and}$$

$$\alpha_3 = \cos \theta$$

(2.8)

The free energy of a cubic system is written as:

$$F_{cub} = K_4 \sin^2 \theta - \frac{1}{8} K_4 (\cos 4\phi + 7) \sin^4 \theta$$

(2.9)

Here θ is measured out-of-plane i.e., against the [001] direction, and ϕ is measured in the in-plane i.e., against the [100] direction as shown in Figure 2.2. Equation 2.9 is valid for α -Fe in the bulk symmetry. This means that the crystal anisotropy in bulk Fe, unlike thin film, is truly cubic ($K_{4\parallel} = K_{4\perp}$). Figure 2.3 (a) shows the free energy surface of the fourfold anisotropy with the crystal directions marked in easy $\langle 100 \rangle$, intermediate $\langle 110 \rangle$, and hard $\langle 111 \rangle$ axis for Fe. In the absence of an external magnetic field, the magnetization lies along the easy axis (100) direction. Along with fourfold cubic anisotropy, there exists uniaxial anisotropy in thin films in both in-plane and out-of-plane direction, which can be described as:

$$F_u^{\parallel} = K_{2\parallel} \sin^2 \theta \cos^2(\phi - \delta)$$

$$F_u^{\perp} = K_{2\perp} \sin^2 \theta$$

(2.10)

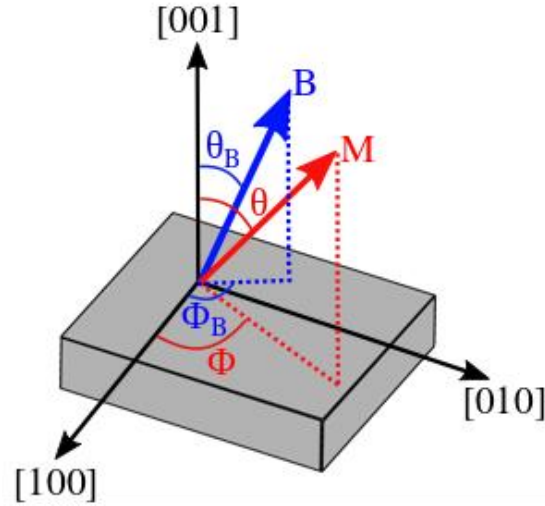


Figure 2.2 Schematic representation of the coordinate system for the film planes.

where δ is the angle between the easy axis of uniaxial in-plane direction with respect to the easy axis of cubic in-plane direction. Figure 2.3 (b) shows the free energy surface of the two fold uniaxial in-plane anisotropy for the Fe crystal system. The uniaxial anisotropy contribution becomes significant in the case of ultrathin films since it originates from strain induced at the surface and interface of the film. Thus, the total intrinsic anisotropy of a thin film can be divided into volume and surface contribution depending on the thickness ‘d’ of the film

$$K_i = K_i^v + \frac{K_i^{s,eff}}{d} \quad (2.11)$$

Here $K_i^{s,eff} = K_i^{s,substrate} + K_i^{s,vacuum}$ contains both surface contributions from the substrate surface and interface as well as vacuum surface. d is the thickness of the film. Usually, $2K_i^{s,eff}$ is taken since there are two surfaces, and it is difficult to separate the contributions from both properly. Note that this is an energy density and K_i^v is a constant contribution originating from the inner part of the sample. The subscript i stands for various contributions mentioned in equation 2.6, 2.18, and 2.19.

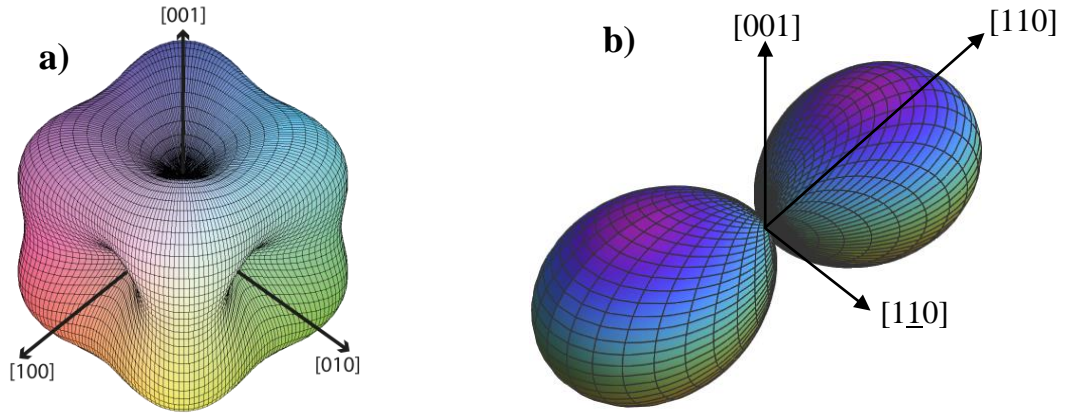


Figure 2.3 Free energy surface of a cubic system with (a) $K_4 > 0$, (b) uniaxial in-plane anisotropy with $K_{2\parallel} > 0$. The color scale does not contain any physical information.

There is a temperature dependence of all the anisotropy energies depending on several factors, for example, thickness. The general temperature dependence of anisotropy according to the Callen-Callen model [40] is given by

$$\frac{K_i(T)}{K_i(0)} \propto \frac{M(T)^{\frac{i(i+1)}{2}}}{M(0)} \quad (2.12)$$

where i is the order of the constant. Therefore, uniaxial anisotropy $K_2 \propto M^3(T)$ and cubic anisotropy $K_4 \propto M^{10}(T)$.

2.2 Landau-Lifshitz-Gilbert equation

The motion of the magnetization M around its equilibrium position is described by the Landau-Lifshitz-Gilbert (LLG) equation [41]:

$$\frac{\partial \vec{M}}{\partial t} = -\gamma(\vec{M} \times \vec{B}_{eff}) + \frac{\alpha}{M} \left(\vec{M} \times \frac{\partial \vec{M}}{\partial t} \right) \quad (2.13)$$

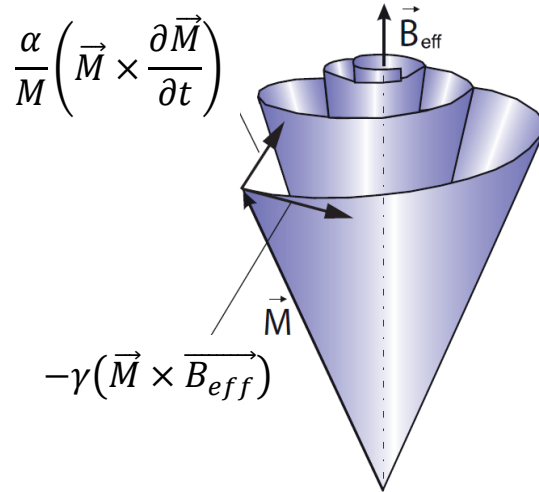


Figure 2.4 Trajectory of magnetization according to equation 2.13 [42].

The first term in the right-hand side of equation 2.13 represents the precession of the magnetization around effective magnetic field B_{eff} which includes the driving rf-microwave field (trajectory shown in Figure 2.4), the demagnetizing field, the external field, and the anisotropy field. The second term on the right-hand side represents the damping, which pushes the precession back to its equilibrium position. α is the damping parameter and is related to the Gilbert damping parameter G according to

$$\alpha = \frac{G}{\gamma M} \quad (2.14)$$

where γ is the gyromagnetic ratio given by $\frac{g\mu_B}{\hbar}$, where g is spectroscopic splitting factor, usually called the g-factor (in general the g-tensor). The g-factor describes the ratio of spin and orbital momentum:

$$g = 2 \left(\frac{\mu_l}{\mu_s} + 1 \right) \quad (2.15)$$

2.3 Ferromagnetic resonance

Ferromagnetic resonance (FMR) is the resonant absorption of external electromagnetic radiation in a ferromagnetic substance [43]. The measurement technique is analogous to Electron spin resonance (ESR) or Electron paramagnetic resonance (EPR). On applying an external magnetic field to paramagnetic material, the separation between energy levels of an unpaired electron spin increases and the resonance occurs when the frequency of microwave matches with the energy difference $\Delta E = h\nu = g\mu_B B$ (Zeeman effect). Here g is the g -factor described in section 2.2. However, the resonance in ferromagnet differs from paramagnet or isolated atom. EPR deals mainly with individual isolated atoms (spin or orbital moment), which are weakly interacting, whereas FMR deals with a complex system of strongly interacting electrons (exchange-coupled spins) [43]. When the magnitude and orientation of the magnetization inside a ferromagnetic crystal change, the resonance condition can be significantly changed. The most common form of resonance condition is

$$\omega_0 = \gamma B_{eff}, \gamma = \frac{g\mu_B}{\hbar} \quad (2.16)$$

Therefore, the resonance condition can be experimentally observed either by keeping the external field constant and varying the microwave frequency or by keeping the microwave frequency constant and varying the magnetic field. The latter case is adopted in this work (also at different $f < 40$ GHz). Since B_{eff} depends on the crystal symmetry, the shape of the sample, direction of the external field, and magnetization direction, the magnetic anisotropy contributions can be determined by analyzing the resonance field. The resonant absorption line is also characterized by its intensity and linewidth (ΔB), which is the full-width at half maximum (FWHM) of the absorbed signal. The linewidth gives information about the relaxation process (magnetic damping) inside the ferromagnet.

Smit and Beljers [44] have suggested a very convenient method to determine the resonance frequency of FMR. They took spherical coordinate system where the orientation of the magnetization M is defined by polar and azimuthal angle ϕ and θ , respectively. The

resonance frequency is given by the double derivatives ($F_{\theta\theta}, F_{\phi\phi}$) of the anisotropic part of the magnetic free energy density F after the spherical coordinates:

$$\omega_{res} = \frac{\gamma}{M \sin \theta} (F_{\theta\theta} F_{\phi\phi} - F_{\theta\phi}^2)^{\frac{1}{2}} \quad (2.17)$$

In this approach, the sample is assumed to be homogeneously magnetized, and dynamical effects (damping) are neglected. This means the precession of magnetization is described by only the first term in LLG equation 2.13. In the FMR experiment, F is varied by sweeping the external magnetic field at a constant microwave field, which perturbs the magnetization. The field at which resonance frequency matches the employed microwave frequency is called the resonance field $B_{res} = \mu_0 H_r$. The characteristic feature of the resonance frequency in a single crystal is that it depends on the angle of the magnetizing field with respect to the crystallographic axes. This dependence is caused by magnetocrystalline anisotropy. At a fixed microwave frequency, the resonance field B_{res} is lowest near the easy axis of the magnetization and highest in the hard axis. This change defines the anisotropy energy of the system, which comes from the crystal structure, as explained in section 2.1. In a ferromagnetic thin film (Fe/GaAs used in this work) having a BCC structure containing tetragonal distortion, the free energy F is given by:

For Fe (100)

$$F = -M \cdot B (\sin \theta \cdot \sin \theta_B \cdot \cos(\phi - \phi_B) + \cos \theta \cos \theta_B) + K_{2\parallel} \sin^2 \theta \cos^2(\phi - \delta) - \frac{1}{8} K_{4\parallel} (3 + \cos 4\phi) \sin^4 \theta - \left(\frac{1}{2} \mu_0 M^2 - K_{2\perp} \right) \sin^2 \theta \quad (2.18)$$

For Fe (110)

$$F = -M \cdot B (\cos \theta \cos \theta_B + \cos(\phi - \phi_B) \sin \theta \sin \theta_B) + K_{2\parallel} \sin^2 \theta \cos^2(\phi - \delta) + \frac{1}{4} K_{4\parallel} \left(\cos^4 \theta + \sin^2 2\theta \left(\cos^2 \phi - \frac{1}{2} \sin^2 \phi \right) + (\sin^4 \theta * (\sin^4 \phi + \sin^2 2\phi)) \right) + \left(\frac{1}{2} \mu_0 M^2 - K_{2\perp} \right) \cos^2 \theta \quad (2.19)$$

Here θ_B and ϕ_B are the polar and azimuthal angle of external field B with respect to [001] and [100]-direction, respectively. δ is the angle between the easy axis of uniaxial in-plane

anisotropy $K_{2\parallel}$ and easy axis of in-plane cubic anisotropy $K_{4\parallel}$. $K_{2\perp}$ is the out-of-plane uniaxial anisotropy. The coordinate system for the film used in this work is shown in Figure 2.2.

The anisotropy field $\mu_0 H_a = 2K_{2\perp}/M$ in Tesla can be determined by measuring the angular dependence of the resonance field B_{res} at a fixed microwave frequency and fit the data with equation 2.17 evaluated at equilibrium angles of the magnetization θ and ϕ . When the external magnetic field is oriented along the film plane, the resonance field can be simplified as equations (2.18) and (2.19). These equations are valid for samples with saturated magnetization, which means the field applied is enough to align all the magnetic moments parallel to the equilibrium angle of the magnetization (saturated or linear mode). When the magnetization of the sample is not fully saturated, a small signal (lower intensity) is observed at lower fields called unsaturated or non-linear mode. Equation 2.20 and 2.21 indicates that f^2 versus B_{res} makes a parabolic function. Therefore, the g-factor of the film (by using γ from equation 2.16) can be determined by measuring the frequency-dependent resonance field. This kind of measurement and analysis was performed in this work described in chapter 5.

For $B \parallel [1\bar{1}0]$ direction

$$\left(\frac{\omega}{\gamma}\right)^2 = \left(B_{res\parallel} - \frac{2K_{4\parallel}}{M} - \frac{2K_{2\parallel}}{M}\right) \left(B_{res\parallel} + \mu_0 M_{eff} + \frac{K_{4\parallel}}{M}\right) \quad (2.20)$$

For $B \parallel [100]$ direction

$$\left(\frac{\omega}{\gamma}\right)^2 = \left(B_{res\parallel} + \frac{2K_{4\parallel}}{M}\right) \left(B_{res\parallel} + \mu_0 M_{eff} + \frac{K_{4\parallel}}{M}\right) \quad (2.21)$$

In typical FMR experiments, the absorption of microwave power as a function of the external magnetic field is measured. Conventionally a resonance cavity is employed to measure FMR. However, other ways can be used also, for example, using a coplanar

waveguide where microwaves are transmitted through a microstrip line. The absorbed power in the microwave set-up is directly proportional to the derivative of the imaginary part of susceptibility $\partial\chi''/\partial B$. The relation between absorbed power and susceptibility is given by

$$P = 0.5\omega\chi''b^2 \tag{2.22}$$

where b is the amplitude of the microwave field. High sensitivity can be achieved at Eigen resonance of the cavity when all the microwave power is absorbed, and there is zero reflection, albeit in the ideal case. In reality, some power is always lost during transmission, which is measured subsequently as the reflected power.

2.4 Magnetic relaxation

The resonance linewidth ΔH is a measure of relaxation processes inside a ferromagnet, e.g., spin relaxation, spin fluctuation, and scattering. Two principal mechanisms are responsible for magnetic relaxation: spin-lattice relaxation and spin-spin relaxation [45]. The spin-lattice relaxation, also called intrinsic or viscous damping, is the direct energy dissipation from the magnetic system to the thermal bath – an irreversible process. The spin-spin relaxation is the energy scattering to the other spin-wave keeping the energy within the magnetic spin system. Figure 2.5 illustrates both the processes during magnetization dynamics. The uniform motion of the magnetization with $k = 0$ (uniform mode) in an FMR experiment may scatter with energy dissipation into the thermal bath (path 1). It can also scatter into non-uniform spin waves (path 2) with $k \neq 0$ – a reversible process. In the long run, this energy also travels along path 3 into the heat sink. For both processes, the structural or magnetic phase transition is crucial since any spin fluctuation influences the linewidth as a function of temperature. The theoretical description of these processes was given by the Bloch-Boembergen equation [46, 47]

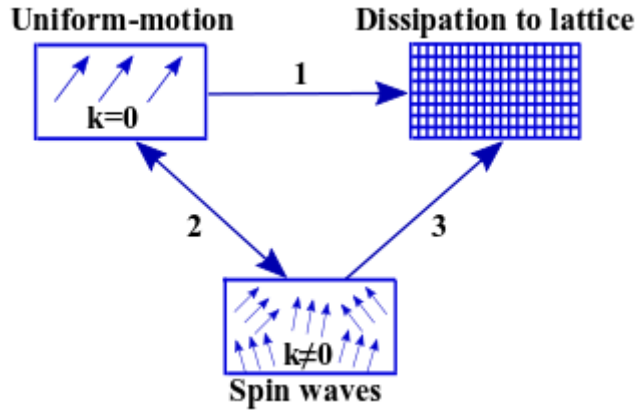


Figure 2.5 Schematic illustration of different relaxation processes. Reproduced from [45].

$$\frac{\partial \vec{M}}{\partial t} = -\gamma(\vec{M} \times \vec{B}_{eff}) - \frac{M_x}{T_2} \hat{e}_x - \frac{M_y}{T_2} \hat{e}_y - \frac{M_z - M_s}{T_1} \hat{e}_z \quad (2.23)$$

In this case, two different relaxation rates T_1 and T_2 are introduced in the Landau-Lifshitz equation. T_1 denotes the longitudinal relaxation rate which follows the direct path 1, and T_2 is the transverse relaxation rate in which the energy is scattered to the transverse components of the magnetization M_x and M_y [45]. Figure 2.6 illustrates both phenomena. The projection of the magnetization vector on the effective field remains constant, and energy is scattered into the transverse components.

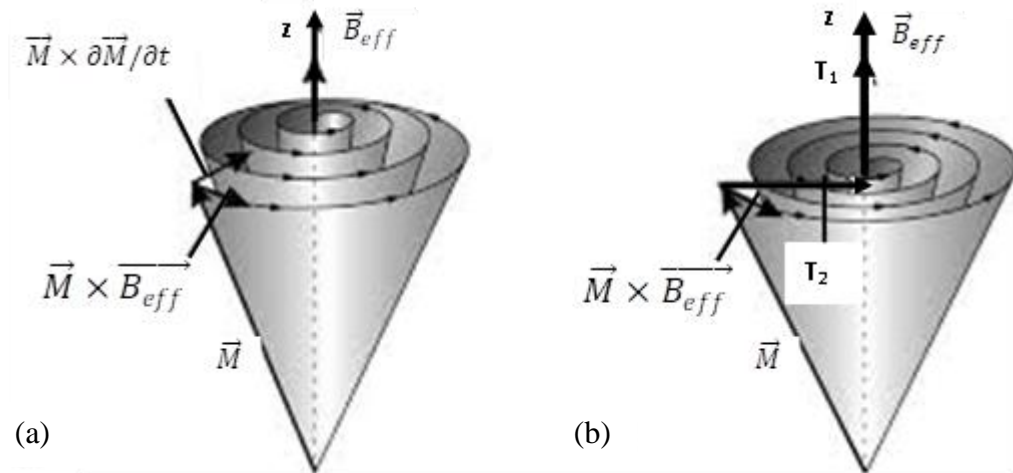


Figure 2.6 Schematic illustration of (a) LLG equation and (b) Bloch-Bloembergen process of spin-spin relaxation taken from [48].

2.4.1 Gilbert damping

The second term in the LLG equation 2.13 describes the Gilbert damping [41], which includes Gilbert damping parameter G (equation 2.14) which gives the relaxation rate in sec^{-1} while α is a dimensionless quantity. The origin of Gilbert damping is assumed to be spin-orbit coupling. The effect leads to spin-flip scattering of electrons resulting in the transfer of angular momentum and energy from spin degrees of freedom to the lattice [49]. The value of parameter α determines the rate of damping precession in a ferromagnet. Therefore, it is of great importance in spintronics devices where a fast switching process is advantageous.

Two modes of electronic transition have been suggested in bulk ferromagnetic systems leading to spin-orbit interaction responsible for Gilbert damping. The first is when magnon annihilation leads to electron-hole pair generation that occupies the same band called intraband damping. This makes the damping inversely proportional to the temperature. The dependence of this mode on the temperature shows metallic phenomena, hence it is termed as ‘conductivity-like’. The second mode also involves magnon annihilation leading to electron-hole pair generation, but in this case, the pairs occupy different bands called interband. This mode also shows a temperature dependence but has the opposite dependence, so it is termed ‘resistivity-like’ [49-51]. These modes show that the damping is correlated with the density of states, showing the importance of the 3d band in ferromagnets and that it strongly depends on the spin-orbit parameter for both the intraband and interband processes [52, 53] at the Fermi edge. The Gilbert parameter α can be determined by measuring frequency-dependent FMR linewidth ΔH . A standard FMR experiment assuming uniformly magnetized sample leads to a linear dependence of linewidth ΔH_G on ω

$$\Delta H_G(\omega) \approx \frac{2}{\sqrt{3}} \frac{G}{\gamma^2 M} \frac{\omega}{\cos \beta} \quad (2.24)$$

where β is the angle between \vec{B}_{eff} and \vec{M} . The linear slope of linewidth ΔH as a function of frequency as shown in Figure 2.7 gives α parameter.

$$\mu_0 \Delta H_{pp} = \mu_0 \Delta H_0 + \frac{2}{\sqrt{3}} \frac{\alpha}{\gamma} 2\pi f$$

(2.25)

ΔH_{pp} represents the peak-to-peak linewidth $\Delta H_{pp} = \frac{1}{\sqrt{3}}\Delta H_{FWHM}$, where ΔH_{FWHM} (full-width at half maximum) is extracted from complex Lorentzian fit. ΔH_0 is the inhomogeneous broadening which comes from inhomogeneities present in the sample. Inhomogeneity can arise from imperfection or defects present in the crystal structure or polycrystalline sample. This gives an offset ΔH_0 in the frequency-dependent linewidth plot, as shown in the shaded area in Figure 2.7. It is important to note that the Gilbert damping contribution is anisotropic [17, 18, 54, 55]. It is because the spin-orbit coupling, and the resonance linewidth are always angular-dependent. The magnetization precession can be easily damped in the easy axis as compared to the hard axis.

The model of intrinsic damping is valid for a pure ferromagnet, but if a ferromagnetic film is capped with a non-magnetic or metallic layer, other contributions may exist. The enhancement of Gilbert damping is due to the transfer of spin angular momentum to the adjacent non-magnetic layer known as spin pumping [56]. The effective magnetic damping is considered then as a sum of intrinsic damping (ΔH_G), inhomogeneous broadening (ΔH_0), and spin pumping (ΔH_{sp}), which decays inversely with the ferromagnet film thickness.

$$\Delta H_{eff} = \Delta H_0 + \Delta H_G + \Delta H_{sp} \quad (2.26)$$

2.4.2 Two-magnon scattering

A second important magnetic damping also called extrinsic damping represents the non-uniform magnon modes ($k \neq 0$) as shown in Figure 2.5 in path 2. The scattering process or energy transfer from uniform to non-uniform modes is termed as two-magnon scattering. Extrinsic damping originated from inhomogeneities (such as point or line defects, impurities, non-uniform film, and strained film due to lattice mismatch) present in the ferromagnet. The sample which cannot be treated as a single domain, the interaction between multiple domains (magnetization precession), can give rise to excitation of magnon scattering. The theoretical description of two-magnon scattering is given by Bloch-Bloembergen (equation 2.23). This

equation describes the energy dissipation through two major relaxation channels (paths 1 and 2) to the final thermal bath of the lattice. The linewidth from the Bloch-Bloembergen equation by taking T_2 relaxation into account [48] is given by

$$\Delta H_{BB} = \frac{\partial H_{res}}{\partial \omega_{res}} \frac{1}{T_2} \quad (2.27)$$

Here H_{res} is the resonance field and $\partial H_{res}/\partial \omega_{res}$ can be easily calculated from the resonance equation (for example, equation 2.20 or 2.21). Unlike Gilbert damping described by equation 2.24, the frequency dependence of two-magnon scattering is not linear with ω . It saturates to a linear slope at a very high frequency but gives a steep non-linear slope at a low frequency (see Figure 2.7). The result for resonance linewidth is given by

$$\Delta H_{2M}(\omega) = \Gamma \sin^{-1} \frac{\sqrt{\omega^2 - \left(\frac{\omega_0}{2}\right)^2} - \omega_0/2}{\sqrt{\omega^2 - \left(\frac{\omega_0}{2}\right)^2} + \omega_0/2} \quad (2.28)$$

$$\text{with } \omega_0 = \gamma 4\pi M_{eff} \quad (2.29)$$

Here Γ gives the strength of the two-magnon scattering mechanism, effective magnetization $4\pi M_{eff}$ includes the anisotropy fields. The two-magnon scattering can also be anisotropic since it depends on the direction of the misfit dislocations. The experimental evidence of non-linear linewidth in Fe films on GaAs (001) capped with Au, Pd and Cr was reported by G. Woltersdorf et al. [57] using time and spatially resolved Kerr effect measurements. They have found that three capping layers behave differently in terms of the spin relaxation process. Au cap layers give only bulk Gilbert damping of the Fe film, while Pd cap layers cause an additional Gilbert damping due to spin pumping. On the other hand, Cr cap layers lead to robust extrinsic damping, which can be described by two-magnon scattering. Thus, the combination of Gilbert damping, inhomogeneous broadening, and two-magnon scattering gives a better understanding of spin dynamics in thin films and multilayers.

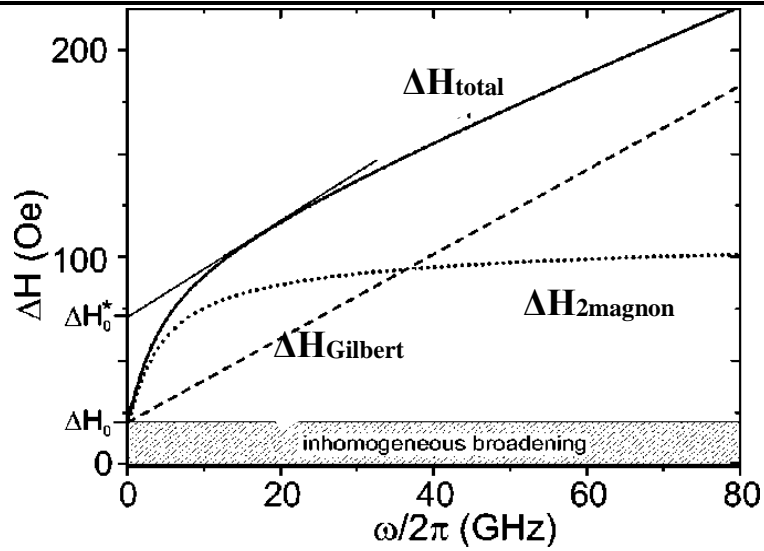


Figure 2.7 Schematic diagram of FMR linewidth as a function of frequency taken from [58]. The dashed line corresponds to pure Gilbert damping represented by equation 2.24, the dotted curve corresponds to two-magnon scattering represented by equation 2.28, and the solid curve is the sum of all contributions. The shaded area shows the offset in the linewidth coming from inhomogeneous broadening.

3 Experimental techniques and methodology

3.1 UHV set-up

The experiments performed for this thesis were carried out in an ultra-high vacuum (UHV) chamber maintained at a base pressure of $\leq 5 \times 10^{-11}$ mbar. To reach such high vacuum conditions, the chamber has a combination of ion getter pump (IGP) (Varian VacIon Plus 300) along with a Varian TM titanium sublimation pump (TSP) and the turbomolecular pump (Pfeiffer TM Compact Turbo TMU 521 P). It is also attached to a load lock chamber maintained at a base pressure of $\leq 6 \times 10^{-6}$ mbar. A rotary pump serves as a pre-pump for the turbomolecular pump with a base pressure below 10^{-2} mbar. An ion gauge measures the absolute pressure in the UHV chamber. A manipulator allows sample movement in Z, X, Y, and ϕ (rotation in the x-y plane) directions. Z-direction by 800 mm and ϕ by 360° movements are controlled by stepper motor using the computer (Labview program) with a precision of 0.01 mm and 0.5° , respectively. Two-micrometer screws move the sample manually in the x-y plane within a circle of radius 25 mm. The manipulator is equipped with a flow cryostat for liquid nitrogen cooling and a resistive heater to control the temperature, allowing a sample temperature variation from 297 to 960 K.

An integrated current loop inside the sample holder connected to the manipulator is used to heat the sample up to 960 K for sample preparation. Along with the heater, a K-type thermocouple is assembled in the copper sample holder to measure the sample temperature. The UHV chamber is equipped with an electron beam evaporator for film deposition, an Ar⁺ ion gun (sputter gun) to prepare the substrate, low energy electron diffraction (LEED), and Auger electron spectroscopy (AES) for structural analysis. Additionally, the UHV chamber contains a microwave short made of semirigid cable for *in situ* FMR measurement up to 40 GHz. A sketch of the setup is shown in Figure 3.1.

The electron beam evaporator has four pockets having targets of Fe, Ag, Pt, and permalloy (Ni₈₀Fe₂₀). The evaporator used is an Oxford Scientific TMOS VAP4p; the way it works is shown in the schematic sketch Figure 3.2. 99.99% pure Fe turns to positive high voltage potential brought by $U_{HV} = 1.25$ kV. A tungsten wire generates free electrons through glow emission, leading to emission current (I_{emis}). These electrons are accelerated towards

Fe and generate heating. This makes Fe partially ionized by collisions with the electrons. These ions partially meet the Flux meter, on which a compensation current (flux) in the range of 100-200 nA is generated and can be measured. The PID controller measures and holds the flux constant by controlling the filament current. Depending on the filament current, the filament power, the temperature of the W-wire, and thus also the number of the free electrons change. The resulting electrical power, via high-voltage potential, is converted into heat at evaporator material. The deposition rate can thus be kept constant by controlling the flux. The Quartz microbalance, used to measure the thickness of the film, is attached to a metal sheet with two square apertures. It is to prevent the sample from being contaminated by evaporating material while waiting for the stabilization of flux. Through the aperture, a film of shape $4 \times 4 \text{ mm}^2$ or $2 \times 2 \text{ mm}^2$ can be deposited. The pressure during evaporation can be maintained below 7×10^{-10} mbar, which is a very pure condition for epitaxial deposition. The Ar^+ ion gun works on the principle of sputtering: bombarding ionized Ar^+ on the substrate under applied high voltage of 3 keV. The partial pressure during sputtering is kept at 1×10^{-6} mbar. The plasma chamber was used as a load lock chamber for this work e.g., to transfer the sample in and out from the UHV chamber. During the LEED and AES measurement of the sample, it can be rotated with a ϕ motor. For FMR measurements, it has to be turned downwards. It is done by a screwdriver installed in the UHV chamber to rotate the sample holder from an out-of-plane position to an in-plane position inside the chamber. More details of the UHV chamber and its components can be found in [42, 59]. Further techniques e.g., LEED, AES, and *in situ* FMR are described in later section 3.3.

Construction of the vacuum system: The UHV chamber consists of a central sphere, in which the preparation and chemical and structural characterization of the epitaxial films can be performed. Attached to this sphere is the area in which FMR can be measured *in situ*. To be able to approach the different preparation and measurement positions, the specimen is mounted on a VG Scienta TM Omniax 800mm manipulator. A schematic diagram of the whole set-up is shown in Figure 3.1, and Figure 3.3, also contains a block diagram, which makes the complexity of the UHV chamber easier to read. This diagram shows that the evaporator chamber and the transfer chamber can be ventilated and pumped out without affecting the vacuum in the other chamber areas. All the essential parameters, like sample temperature and pressure inside the main chamber, are monitored and saved in a file through a program interfaced with the chamber.

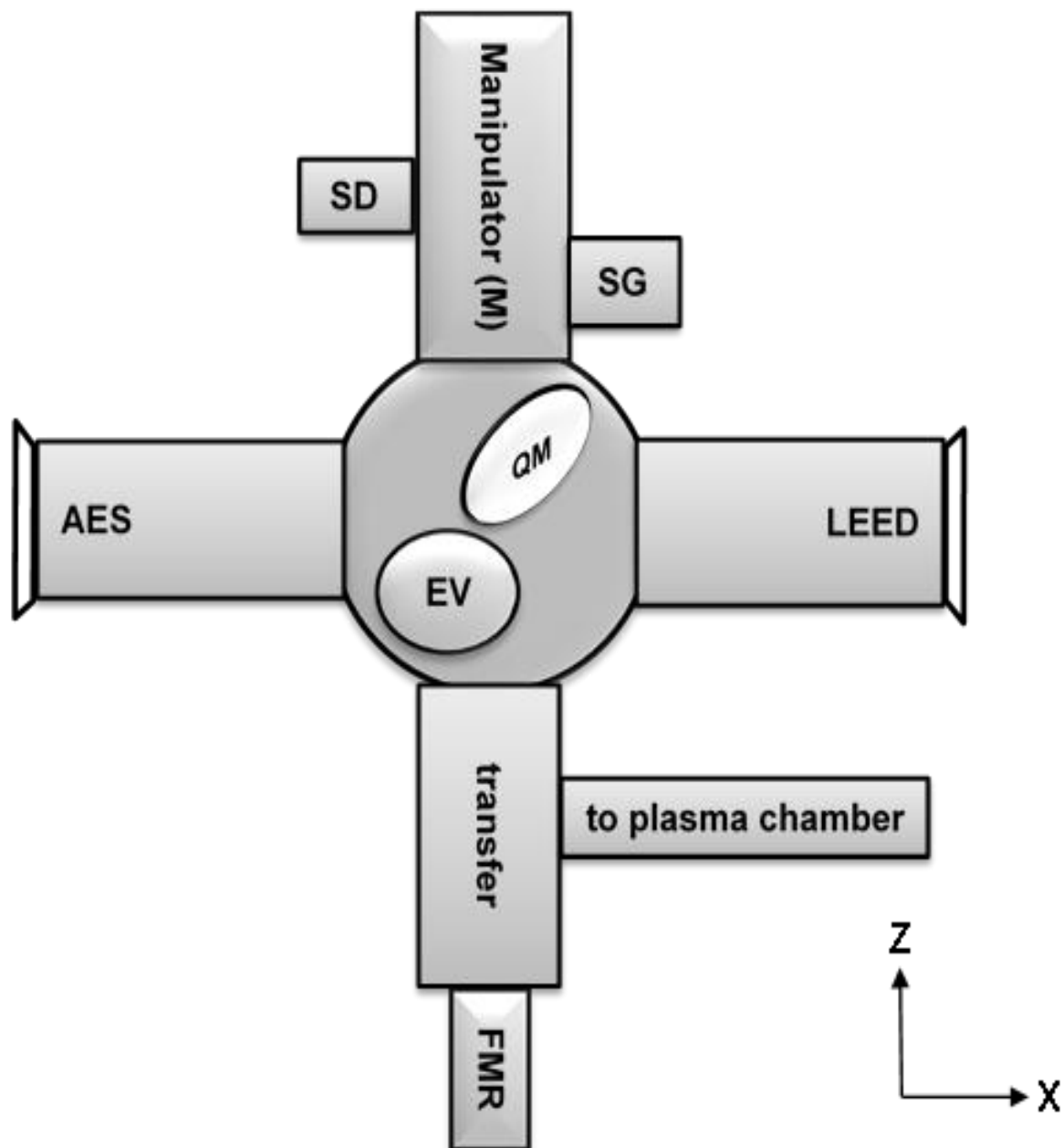


Figure 3.1 The UHV set-up is showing essential elements in a cross-section of the vacuum chamber in the x-z plane. Manipulator (M), *in situ* screwdriver (SD), evaporator (EV), quartz monitor (QM), sputter gun (SG).

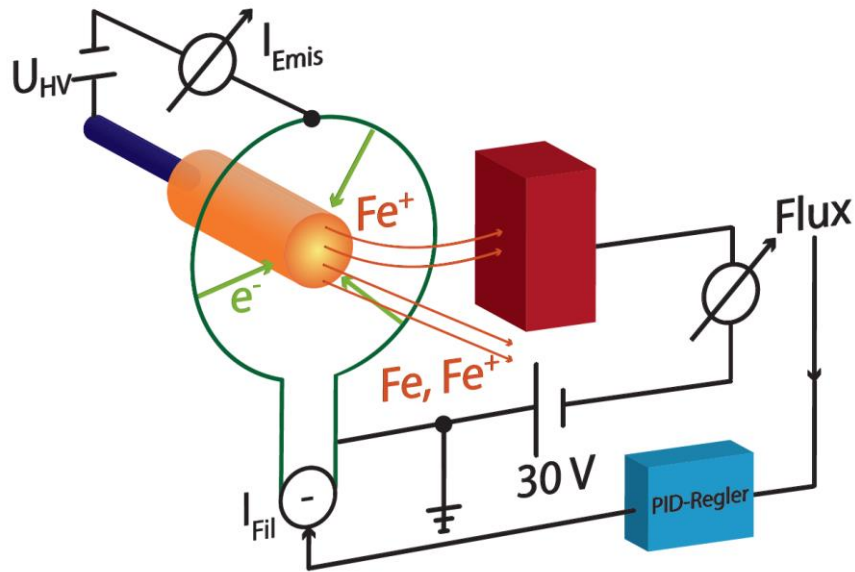


Figure 3.2 Schematic diagram of the evaporation process [42].

3.2 Advantages and limitations of the UHV system

In general, most of the thin-film studies are either performed *ex situ* or in embedded systems, where the ultra-thin magnetic film is covered with a protective nonmagnetic layer. However, in both cases, the oxidation of the surface or nonmagnetic protective layer can significantly modify the magnetic as well as transport properties. In contrast to this, *in situ* magnetic and structural measurements under the ultra-high vacuum condition are more useful to obtain a genuine property of the ultra-thin magnetic layer itself without a capping layer. Furthermore, *ex situ* measurements, as a function of film thickness, involve growing a series of samples of varying film thicknesses. By continuously monitoring the electron diffraction pattern and ferromagnetic resonance of a growing magnetic film *in situ*, a detailed thickness dependence curve can be obtained during the growth of a single sample. The *in situ* method thus makes it practical to vary growth parameters, such as substrate temperature, pressure in the chamber, and film growth rate.

We have *in situ* synthesis and characterization facility which has been utilized for the sample preparation and measurements. In experimental physics, "*in situ*" typically refers to a method of data collection or manipulation of a sample without exposure to an external environment. This prevents the sample from oxidation and thus reveals the genuine

properties during growth. During sample growth, we can visualize various parameters as well as perform different measurements at a glance. The *in situ* setup we have used for the purpose has three characterization tools (LEED, AES, and FMR) attached and one synthesis method (e^- beam evaporation) for the sample preparation. However, as there are some limitations for the *in situ* set up e.g., deposition of a sample can be done only by e^- beam technique, and for the magnetic property's measurements, the field is limited (~ 1.2 T).

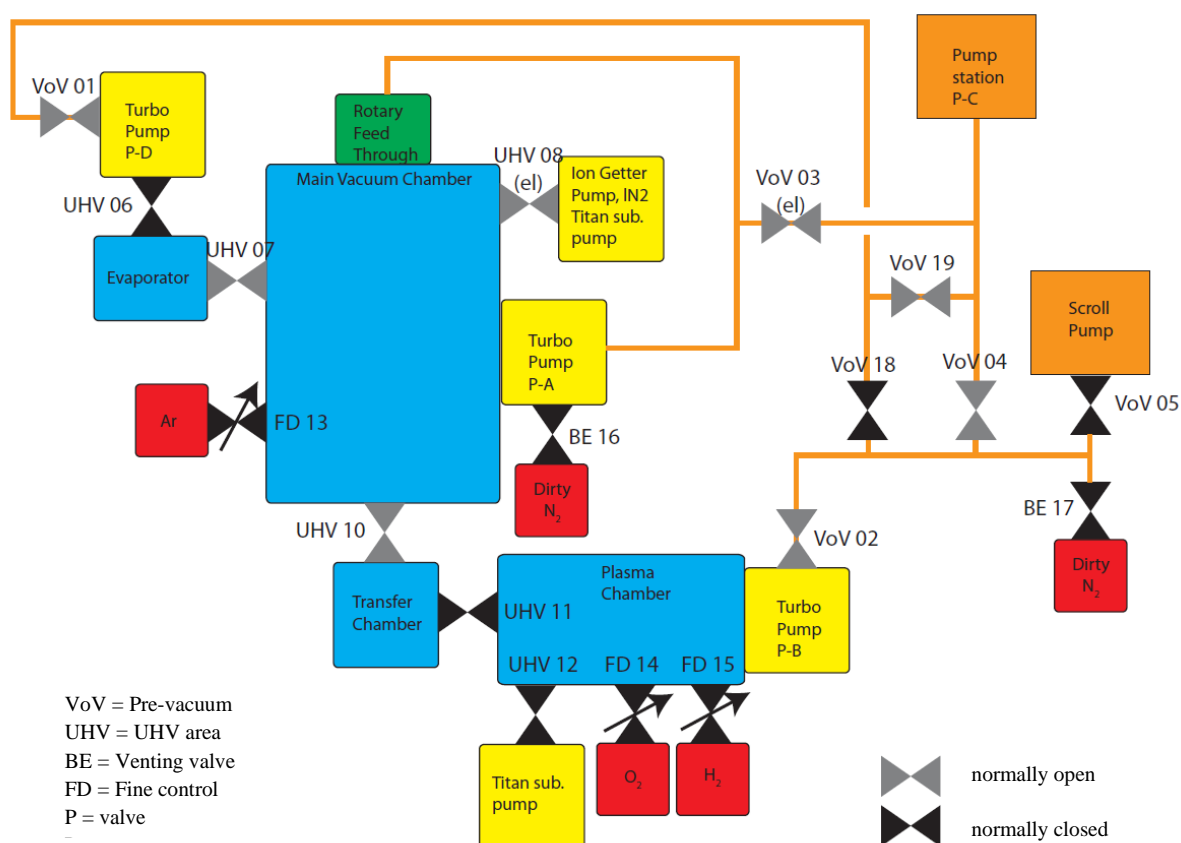


Figure 3.3 Block diagram of the UHV setup describing the connections in a simplified form. The UHV valves separate the UHV area from one part to another, venting valves BE facilitating the venting through dry Nitrogen, 'el' stands for electrically controlled valves which prevent unintentional ventilation of the main chamber in case of power failure, and FD is for the finely metered intake of gases like Ar for sputtering [42].

3.3 In situ Techniques

3.3.1. Low energy electron diffraction

Low energy electron diffraction (LEED) is a technique for the determination of the surface structure of single-crystalline thin films. The basic principle of a standard LEED experiment is the following: a collimated mono-energetic beam of electrons is directed towards a single crystal surface, and the diffraction pattern of the elastically back-scattered electrons is recorded using a position-sensitive detector. Due to the small inelastic mean free path of electrons in low energy range (10-100 eV), typically around 1 nm, as shown in Figure 3.4, sample diffraction is only from the topmost atomic layers of a crystal and is, therefore, best suited for the analysis of surface geometries. The LEED pattern is recorded using a camera with suitable image processing software. As with all methods that use electrons as probes, vacuum conditions are required because electrons cannot penetrate a gas atmosphere at normal pressures. In general, however, the vacuum conditions required to avoid contamination of clean surfaces are more rigorous ($< 10^{-9}$ mbar) than those imposed using electrons (typically $< 10^{-6}$ mbar).

The electrons of the De-Broglie wavelength $\lambda = h/\sqrt{2mE}$ are accelerated parallel to the film normal onto the sample and elastically diffracted at the sample. Here m is the mass of the electron and E is the kinetic energy of the electron. The wavelength at the energies mentioned corresponds to the order of magnitude of atomic distances and can be used for Bragg diffraction. The Bragg condition in vector notation in the reciprocal space is as follows:

$$\Delta\vec{k} = \vec{k} - \vec{k}_0 = \vec{G}_{hkl} \tag{3.1}$$

where k is the wave vector of the diffracted electron, k_0 is an incident wave vector, and G_{hkl} is a reciprocal lattice vector. In the case of a two-dimensional surface, the reciprocal lattice points are arranged infinitely close along the normal direction forming lattice rods, as can be seen in Figure 3.5. The direction of the scattered wave vector can be determined by Ewald construction with a circle of radius $r = |k_0|$. However, the electrons under consideration have a small penetration depth into the material, so the idealization no longer applies. Thus, the

resulting transition from the ideal two-dimensional case to a few atomic layers gives rise to periodic swelling of vertical rods along z-direction as indicated by lens shape in Figure 3.5 (b). The diffraction spots are allowed for a wide range of kinetic energies. This does not mean, however, that the intensities of spots are constant with the energy. Although the electrons do not experience the full periodicity of the crystal perpendicular to the surface, there is still interference of electrons scattered from different atomic layers parallel to the surface. Since the penetration depth is very small, the back-scattered electrons only interact with a few layers of atoms giving rise to broad maxima at the Bragg peak positions and non-zero intensities in the intermediate energy regimes [60].

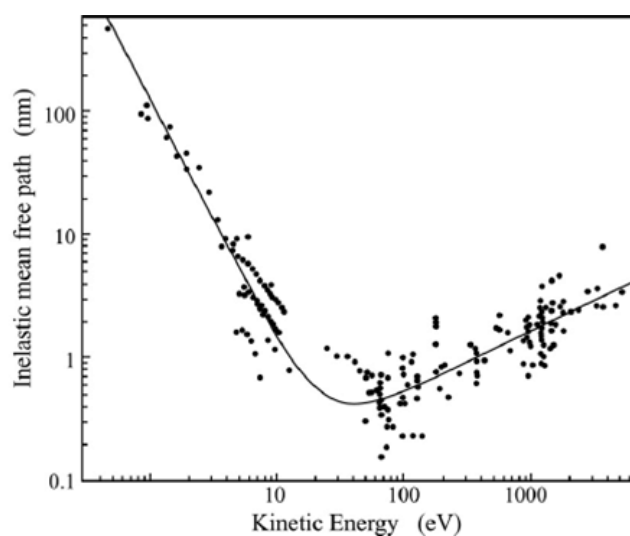


Figure 3.4 Experimental inelastic mean free path as a function of energy for different materials [61].

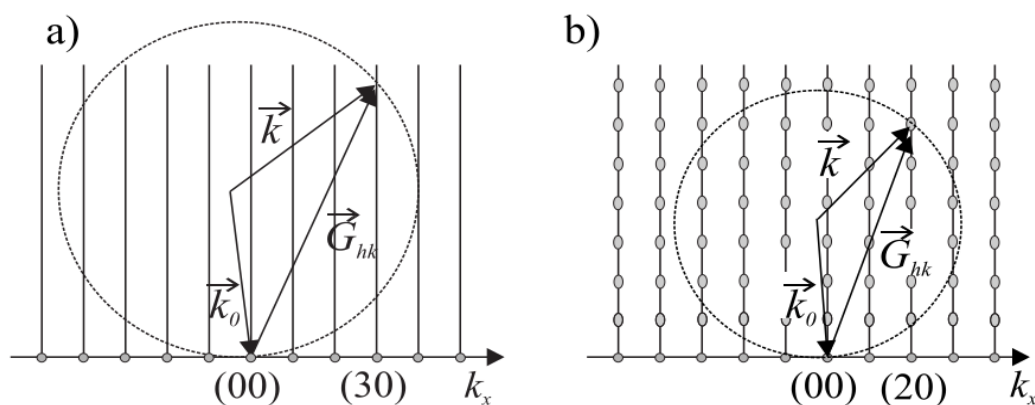


Figure 3.5 (a) Ewald construction for diffraction from a 2D surface (b) with lattice periodicity [62].

3.3.2. Auger electron spectroscopy

Auger electron spectroscopy (AES) is based on the Auger process shown in Figure 3.6, which involves the ionization of a core-level atom, which is followed by de-excitation of an outer-level electron decaying to fill the core hole. The excess energy difference either generates an X-ray photon or is transferred to another outer level causing the ejection of an electron, which is, by definition, an Auger electron. The transition of Auger electron, denoted by the electron levels involved e.g., KL_1L_2 , is independent of the excitation source, and Auger electron leaves the atom with constant kinetic energy. This kinetic energy is calculated by the differences in binding energies of the three levels i.e., $E_K - E_{L_1} - E_{L_{2,3}}$ minus a correction term for the work function and electron wave function relaxation. Each element has a unique set of Auger transitions, which may be used to identify the composition of solid surfaces. The high surface sensitivity of Auger spectroscopy, which dictates the need for an ultrahigh-vacuum system, is due to the limited mean free path of electrons in the 0-3000 eV kinetic energy range, which lies within the range of 5-30 Å. The Auger peaks decay exponentially with overlayer coverage, which is consistent with an exponential dependence of escape probability on the depth of the parent atom.

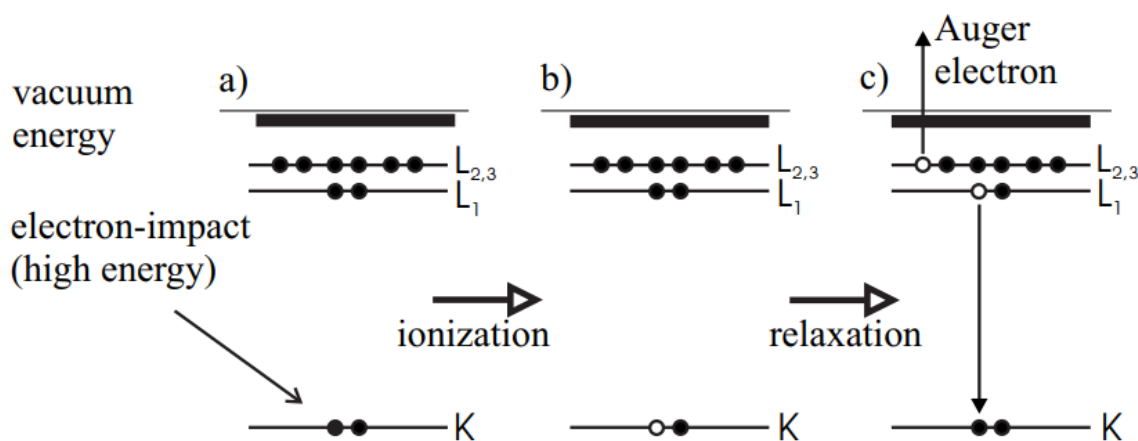


Figure 3.6 Schematic of the Auger process (a) high energy electron impacts on an atom (b) ionization of core-level electron (c) excess energy transferred to outer-shell electron leading to ejection [62].

In the experiment, an electron beam with a kinetic energy of 3 keV is focused on the sample diameter of 0.5 mm and hits the sample at perpendicular incidence guiding the Auger

process there. The emitted Auger electrons are passed through an aperture and then enter the analyzer. A cylindrical mirror analyzer (CMA) with a coaxial electron gun is employed to analyze the energies of Auger electrons. A spectrum is obtained in which the number of detected electrons $N(E)$ is plotted against the kinetic energy. Since the Auger electron intensity is small ($10^{-4} - 10^{-3}$) and is superimposed upon the high background caused by inelastically scattered electrons, Auger electron spectra are typically taken in the derivative mode. The derivative $dN(E)/dE$ is obtained by superimposing a small sinusoidal potential modulation on the analyzer pass energy and synchronously detecting the current passed through the analyzer. By electronically varying the modulation voltage, one has versatile control over the signal-to-noise ratio.

Auger electron transitions require three electron levels so that only elements with atomic numbers greater than three can be detected. The rate of core-level ionization, being one of the critical factors in Auger transition intensity, can be adjusted by varying the primary electron beam energy so that the relative KLL, LMM, and MNN intensities are altered. The KLL Auger transitions are the most intense for low-atomic-number elements, but the LMM transitions increase in intensity with increasing atomic number, and subsequently, the MNN transitions increase as well. By progressively using the KLL, LMM, and MNN series of Auger transitions, the elemental sensitivity variation across the periodic table can be held to a factor of less than fifty.

Assuming that the transition intensities can be measured for the pure elements under a set of controlled conditions, the atomic concentration of element X can be expressed as

$$C_x = \frac{(I_x/S_x)}{\sum_a (I_a/S_a)} \quad (3.2)$$

where S_x is the relative sensitivity and I_x the Auger transition intensity of element X.

3.3.3. In situ ferromagnetic resonance

Ferromagnetic resonance is by far the most powerful technique to study the magnetic anisotropy energies, g-factor, interlayer exchange coupling, and damping mechanism in

magnetic thin films. In experiments, the sample is irradiated with a transverse radiofrequency microwave field (typically GHz), and when the radio frequency coincides with the precession frequency of magnetization, the resonance condition is fulfilled, and the microwave power is absorbed by the sample. In a conventional FMR experiment, one places a ferromagnetic sample in a microwave resonant cavity, in which a standing wave is formed with a magnetic component $h_{m\omega}$ perpendicular to the external magnetic field H_0 . The magnetization of the sample precesses around the effective magnetic field H_{eff} , which comprises of the externally applied field H_0 , the microwave field $h_{m\omega}$, and other internal fields H_{int} , which are responsible for anisotropies and the strong interaction of individual spins in a ferromagnet. For this thesis, however, a self-built *in situ* multi-frequency FMR setup is being utilized, which is mounted in the UHV chamber and can work up to the frequency of 40 GHz.

The schematic of *in situ* FMR setup is shown in Figure 3.7. The measuring probe is located in the middle of a glass adapter, which is placed between the shoe poles of a magnet. Around the glass adapter, the modulation coils are mounted, which modulates the magnetic field in the range of 10-100 kHz. The microwaves are applied from feedthrough connected below the glass adapter suitable for the frequency range of 1-40 GHz. The detection is performed via reflected microwave power. A circulator circuit 'C' is placed between microwave synthesizer and microwave feedthrough, which reduces the microwave power in the forward direction of six circulators (7-40 GHz) connections. The microwave power is directed to the shortcut 'S' made on the semirigid cable and reflected back to the microwave diode. This directs the electrical component of the microwave and allows a DC measurement of microwave power. The generated dc voltage is detected by a lock-in amplifier with the modulation frequency of the external magnetic field by 9 kHz. The external magnetic field is swept while keeping microwave frequency constant. For the lock-in technique, modulation, control of the external magnetic field, and recording of the data, a Bruker TM EMX EPR spectrometer is used here.

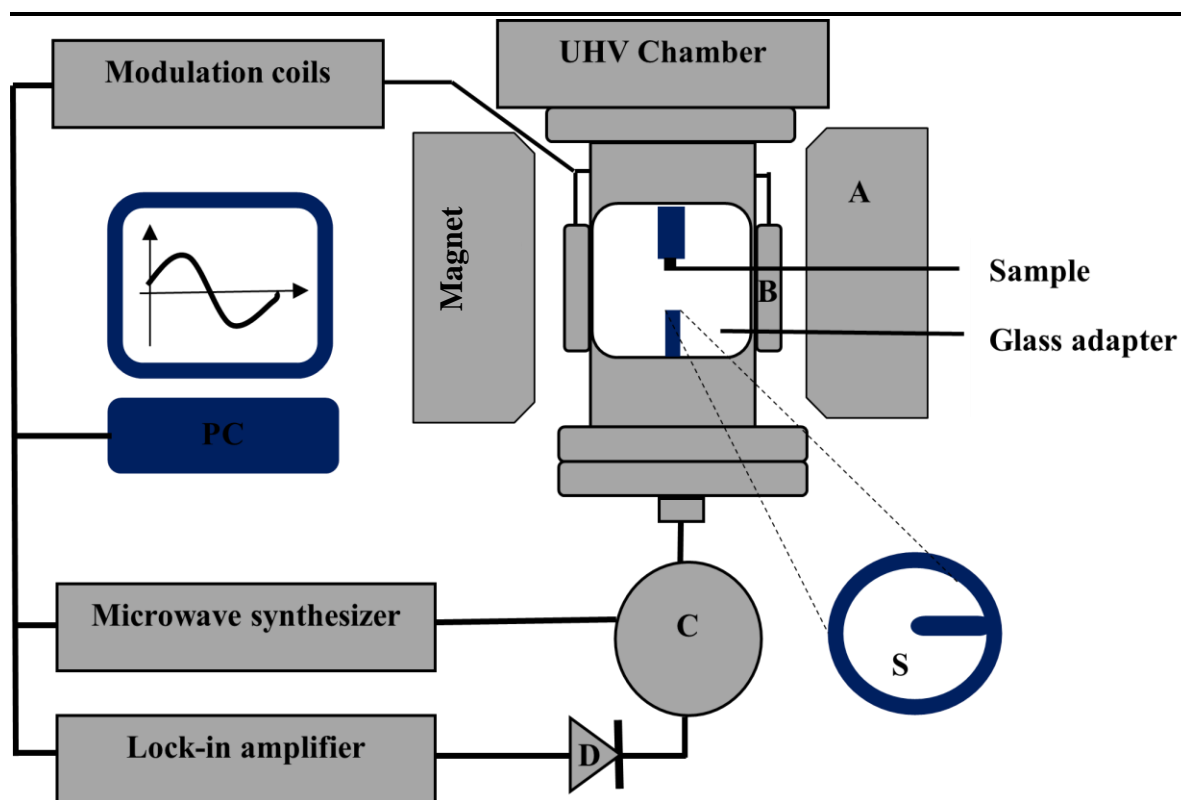


Figure 3.7 The schematic detection path of FMR for *in situ* set-up. Microwave power is transmitted from the synthesizer via circulator (C) and to a short circuit (S). The sample is approached from above and is then in the high-frequency field. Additionally, in the glass area where the short circuit an external magnetic field (A) and a modulation field (B) are applied. The reflected microwave power is transmitted via the circulator (C) to the microwave diode (D) guided. The signal rectified there goes to the lock-in amplifier.

3.4 Ex situ techniques

Apart from *in situ* techniques with the UHV chamber, some *ex situ* techniques were also used to measure the surface morphology and FMR in air.

3.4.1 Atomic force microscopy (AFM)

Atomic force microscopy is a surface analytical technique used in air, liquids, or a vacuum to generate high-resolution topographic images of a surface, down to atomic resolution. Compared to traditional scanning electron microscopy (SEM), it allows the

imaging of dielectric material surfaces without the need for applying conductive layers and allows the determination of surface roughness parameters without the need for additional tests. An AFM uses a cantilever tip to scan over a sample surface. A piezoelectric scanner is attached to the x-y stage of the sample for precise and accurate movement during scanning. A z scanner controls the distance between tip and surface. As the tip approaches the surface, an attractive force between the surface and the tip causes the cantilever to deflect towards the surface. However, as the cantilever is brought closer to the surface, such that the tip contacts it, increasingly repulsive force takes over and causes the cantilever to deflect away from the surface. A laser beam is used to detect cantilever deflections towards or away from the surface. By reflecting an incident beam off the flat top of the cantilever, any cantilever deflection will cause slight changes in the direction of the reflected beam. A position-sensitive photodiode (PSPD) can be used to track these changes. Thus, if an AFM tip passes over a raised surface feature, the resulting cantilever deflection and the subsequent change in the direction of the reflected beam are recorded by the PSPD. An AFM images the topography of a sample surface by scanning the cantilever over a region of interest. The raised and lowered features on the sample surface influence the deflection of the cantilever, which is monitored by the PSPD. By using a feedback loop to control the height of the tip above the surface, thus maintaining a constant laser position, the AFM can generate an accurate topographic map of the surface features [63]. The analysis of the surface in terms of the shape and location of characteristic points most often carried out utilizing AFM is in three modes, namely contact mode, non-contact mode, and tapping mode. In contact mode, the tip contacts the sample surface. The detector monitors the changing cantilever deflection, and the force is calculated using Hooke's law:

$$F = -kx \tag{3.3}$$

where F is the force, k is the spring constant, and x is the cantilever deflection. In non-contact mode, the cantilever oscillates near the surface of the sample but does not contact it. The oscillation is slightly above the resonant frequency. In tapping mode, the cantilever oscillates at or slightly below its resonant frequency. The tip lightly "taps" on the sample surface during scanning, contacting the surface at the bottom of its swing.

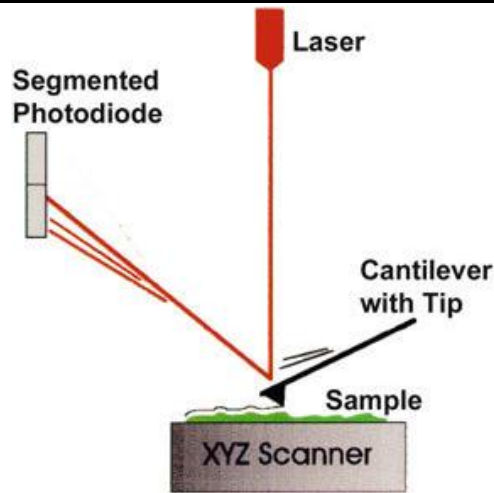


Figure 3.8 Atomic force microscopy diagram showing scanning cantilever with the optical lever (laser and photodiode), which amplifies tiny deflections of cantilever [64].

3.4.2 Ex situ FMR

To perform FMR in an ambient environment, a coplanar waveguide (CPW) is utilized along with a microwave synthesizer and detection technique. The schematic of the set-up is shown in Figure 3.9. The devices used here are Rohde and Schwarz microwave synthesizer SMA 40 and Krytar microwave detector for 40 GHz. The Lock-in technique is the same as for *in situ* FMR setup. The CPW has been lithographically printed on Roger's substrate. The CPW structure on the top side of the substrate consists of a center conductor enclosed by ground planes to both sides. An alternating voltage with a microwave frequency is applied to one end of the center conductor. On the other end, the voltage is measured. According to Biot-Savart law, the current through the center conductor leads to a magnetic field. Since the center conductor is not circular but rectangular, the field lines are somewhat elliptical. Based on the microwave field, the magnetic field oscillates. The sample on top of the CPW interacts with this field, which results in a varying transmission through the CPW, and thereby in a varying voltage at the detector side.

The sample itself is positioned on top of the CPW, as shown in Figure 3.9, and fixed with a sample holder in a goniometer. The external magnetic field is oriented parallel to the film plane. The strength of the magnetic field is measured with a Hall probe. The modulation

coils are specially designed for the set up to fit inside the magnet poles which can modulate the microwave frequency up to 30 kHz.

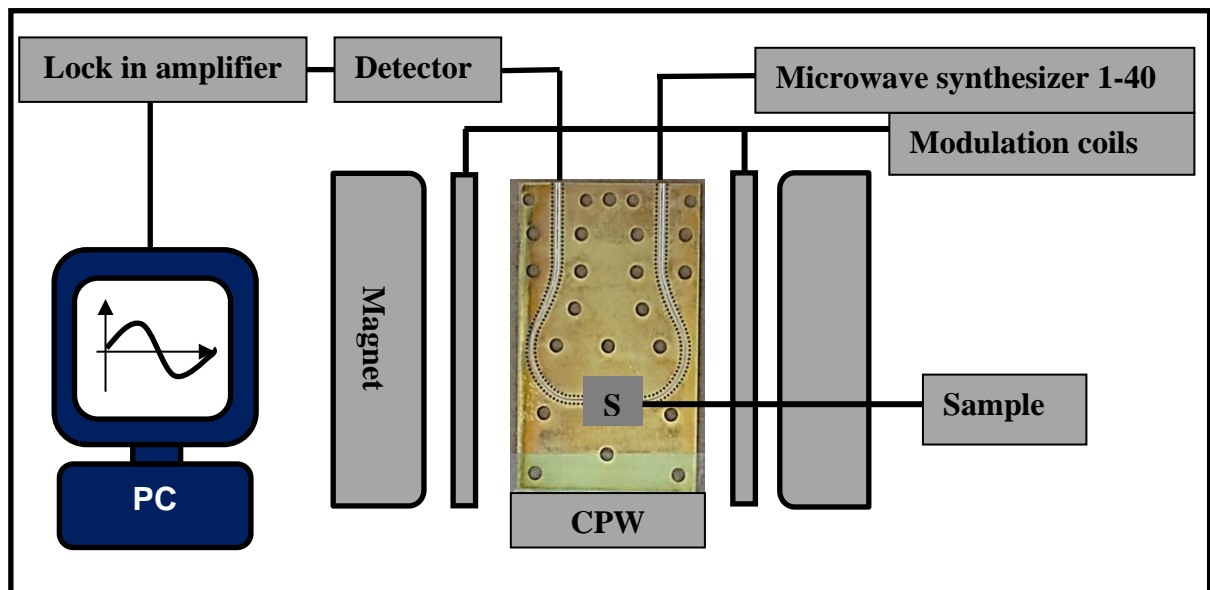


Figure 3.9 Schematic of *ex situ* FMR setup.

4 Structural and magnetic characterization of Fe on GaAs (100) and GaAs (110) as a function of time

In this chapter, the experimental results of the *in situ* LEED, AES, and FMR of epitaxial Fe thin films grown on GaAs (100) and GaAs (110) as a function of time are presented. The time evolution of structural and magnetic properties of uncapped Fe films was studied at room temperature under UHV conditions. It is observed that Fe/GaAs (110) is magnetically unstable with changing anisotropy, while Fe/GaAs (100) is significantly stable with negligible change in anisotropy and relaxation over several hours kept in a vacuum after deposition. A magneto-morphological transition in 4 nm Fe/GaAs (110) was found over 6 days at room temperature. However, for lower thicknesses of Fe (1 nm and 2 nm), the transition was faster. The time-dependent changes of in-plane and out-of-plane anisotropy constants were determined, indicating a sign reversal of in-plane uniaxial anisotropy in 4 nm Fe/GaAs (110), while a decrease of in-plane uniaxial anisotropy in 1 and 2 nm Fe/GaAs (110) was observed. On the other hand, 4 nm Fe/GaAs (100) shows a negligible change in the resonance field over time. The magnetic stability of 4 nm Fe film grown on GaAs (100) and GaAs (110) over several days is compared.

4.1 Introduction

Fe/GaAs heterostructure has been extensively studied for its structural, magnetic, and spin transport properties in the last three decades and is considered as a model system for spintronics devices [19, 23, 28, 65]. Although numerous works on structure, surface morphology, and magnetic properties of uncapped Fe films grown on GaAs have been reported [24, 30, 31, 66, 67], very few studies were focused on time-dependent stability of the structure and magnetic properties of this system [32, 68]. In particular, the effect of structural and morphological changes, acting on the film surface, on the magnetic properties of Fe/GaAs with time is unknown. The smoothening of ultrathin Fe islands grown on GaAs (100) studied by Gillingham et al. [32] is contradictory with the studies by Godde et al. [30], where authors found no change in the surface morphology in Fe on GaAs (100) or GaAs

(110) at room temperature several hours after deposition. Excellent time stability of covered 200 nm thick Fe film grown on GaAs (100) was shown by Weissman et al. [68].

Thomas et al. [69] and Lu et al. [70] demonstrated that the strain relaxation in Fe/GaAs (100) system proceeds in an anisotropic fashion causing in-plane uniaxial anisotropy in thin films. However, they have analyzed the strain relaxation as a function of thickness and temperature. This anisotropic strain relaxation can also affect the magnetic anisotropy of the Fe film even at room temperature if the system is kept in ultra-high vacuum conditions. The Fe/GaAs samples studied here were grown, characterized, and measured *in situ* under UHV conditions and in a broader range of time than in the previously reported experiments. Furthermore, the magnetic stability of such a system at room temperature and under UHV conditions was analyzed using *in situ* FMR measurements.

4.2 Sample Preparation

All the samples discussed in this chapter were prepared with the same synthesis method as described below. In some cases, there was a change in temperature during substrate preparation, which will be mentioned in the individual sample description. A 4×4 mm² cut from commercially available undoped GaAs (100) and GaAs (110) wafer was used as a substrate. The substrate was pre-cleaned with ethanol in an ultrasonic bath before transferring to the UHV chamber. The substrate is then pasted on the sample holder using silver paste, and it is heated up to 150°C for 5 minutes. After transfer into the UHV chamber, the substrate was ion etched with Argon gas at a partial pressure of 1×10^{-6} mbar along with slow heating up to 960 K for one hour. The substrate was placed perpendicularly facing the sputter gun. Argon sputtering was performed at 1 keV during heating, which was reduced to 0.5 keV when the temperature reached a maximum value e.g., 960 K. Subsequently the substrate was annealed at around 920-960 K (exact temperature value for a particular sample will be stated later) for 30 minutes at a pressure of $\leq 8 \times 10^{-9}$ mbar. After the sputtering and annealing process, the substrate was cooled down to room temperature. The substrate preparation yields a clean, well-ordered, oxygen-free, reconstructed GaAs surface seen by LEED and AES. The LEED and AES results will be discussed in section 4.3.

The Fe film named film 1 was grown at room temperature by molecular beam epitaxy using an electron beam evaporator with a deposition rate of 0.11 ± 0.02 nm/min, which was monitored by a quartz crystal microbalance. The base pressure of the UHV chamber was about 5×10^{-11} mbar while it rose to about 7×10^{-10} mbar during Fe deposition. It should be noted that all the samples described in this chapter were characterized without any capping layer on the Fe film. LEED and AES were measured after Fe deposition to confirm the good epitaxial growth. After LEED and AES measurements, the sample was transferred to the FMR position by rotating it downwards using a screwdriver as described in section 3.1. The FMR measurements were carried out using a microwave probe with the external magnetic field applied perpendicular to the microwave magnetic field component and parallel to the film plane. The *in situ* FMR setup has been described in detail in [36, 42].

4.3 Time-dependent structural and magnetic stability of Fe/GaAs (110)

The zinc blende structure of the (110) surface of GaAs can be viewed as two staggered face-centered cubic (FCC) lattices as shown in Figure 4.1 (a). The LEED pattern shows the reciprocal space of the crystal surface plane with a more significant reflex distance in $[\underline{1}10]$ direction. The ratio between two side lengths in $[\underline{1}10]$ and $[100]$ directions should be $\sqrt{2} = 1.414$ in a simple cubic structure for (110) plane, and our LEED pattern as shown in Figure 4.1 (b) results in a ratio of 1.35 ± 0.05 , which is close to the theoretical value. The crystal structure of deposited 4 nm Fe film on cleaned GaAs (110) substrate is again determined by LEED. Figure 4.2 (a) shows a typical LEED pattern of Fe film taken at an energy of 186 eV confirming epitaxial growth of body-centered cubic (BCC) structure. The rectangular LEED pattern also has an aspect ratio of $1:1.43 \pm 0.05$. The broadening of diffraction spots indicates a rough surface which is due to Volmer-Weber growth. STM studies have shown that Fe grows with a 3D cluster on GaAs (110) surface followed by 2D growth for higher film coverage [30, 71]. To see the roughness profile of the film, *ex situ* AFM was performed on surface-oxidized (in air) Fe film. The AFM scan in Figure 4.2 (b) shows a very rough surface with terraces of height 6-8 nm and RMS roughness of 3.4 nm confirming island-like growth of the film. The AES measurement of the film after deposition showed Fe peaks.

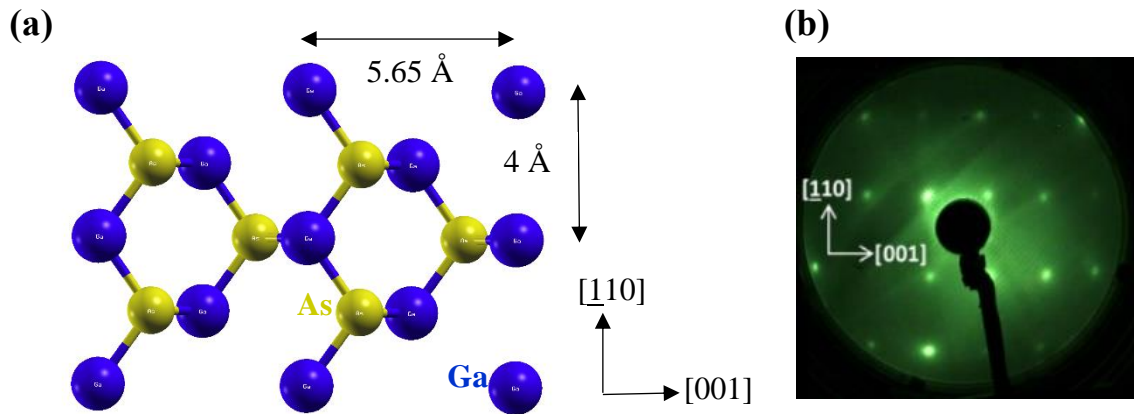


Figure 4.1 (a) Top view of GaAs (110) surface. (b) LEED pattern of cleaned GaAs (110) substrate at an energy of 117 eV.

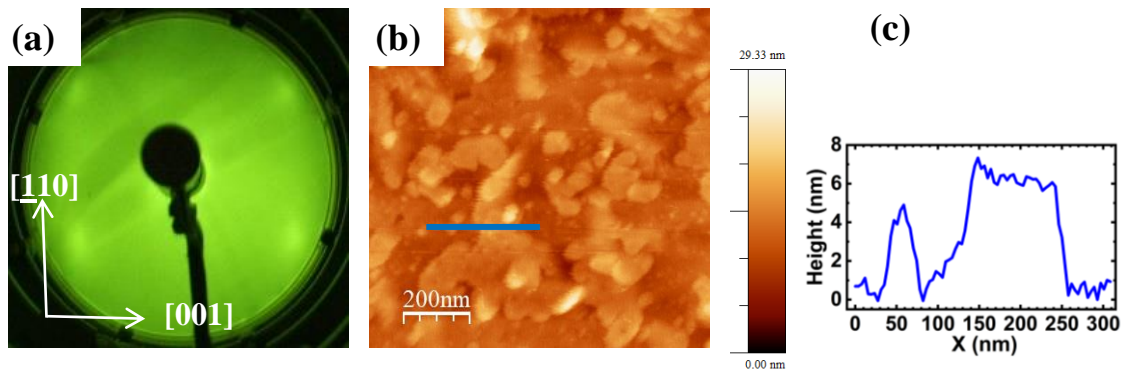


Figure 4.2 (a) LEED pattern of 4 nm Fe/GaAs (110) taken at an energy of 186 eV. (b) AFM scan of the same film (1x1 μm area) oxidized in air. (c) Line profile of the blue line in the image (b) [72].

The magnetic measurement was carried out using *in situ* FMR with the magnetic field applied parallel to $[\bar{1}10]$ direction in the film plane. The time used to measure LEED, AES, and transfer of the sample to FMR position along with setting up *in situ* FMR components was roughly one hour. Therefore, the first FMR spectrum measured of the sample was around 55 minutes after deposition. The FMR spectra were measured every hour at room temperature. Microwave absorption derivative spectra were recorded at a frequency of ~ 13 GHz with a modulation frequency of 9 kHz. The microwave power was calibrated to 12.9 dBm (power calibration using the LabVIEW program). The time constant and conversion time on the lock-in amplifier was set to 40.96 ms and 81.92 ms, respectively. The modulation amplitude was set to 2 mT and the modulation phase to 200° . The pressure during the FMR measurement was maintained at $\leq 1 \times 10^{-10}$ mbar.

The resonance field (fit by complex Lorentzian function) is shifted to 89.4 mT from 89.1 mT after one hour as shown in Figure 4.3 (a). Along with the resonance position shift, the line shape of the FMR spectra is also changed (red curve) after 105 minutes. Figure 4.3 (b) shows the time dependence of FMR spectra taken at 12.93 GHz (constant frequency during measurement) where greyscale represents the normalized amplitude of microwave absorption derivative which is proportional to $\partial\chi''/\partial B$. It is visible in the time dependent FMR spectra that initially a single resonance is present up to 1-4 hours after deposition. However, after 4 hours a second resonance line appears at a higher magnetic field which grows with time to an even higher field and slowly saturates after 40 hours. The lower resonance line shifts drastically to a higher magnetic field in the first 24 hours after deposition. The two resonance lines are visible in the 12th-hour FMR spectrum shown in Figure 4.3.

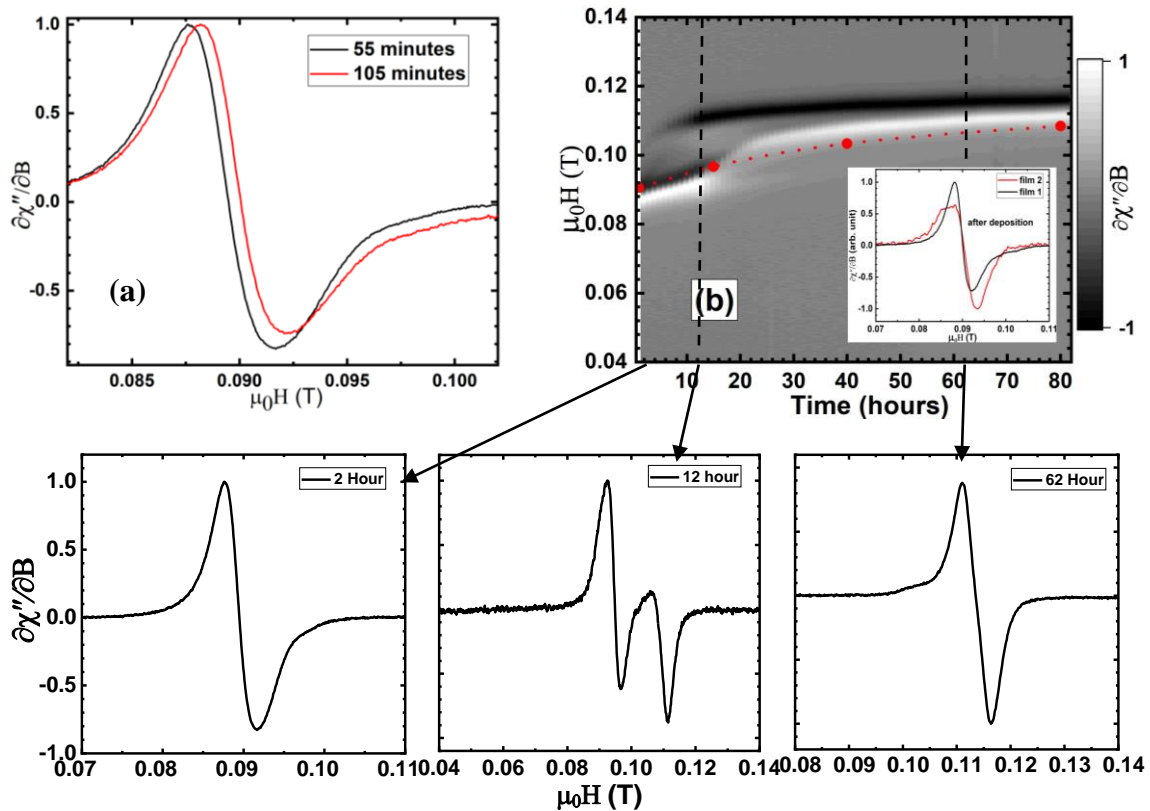


Figure 4.3 (a) Normalized FMR spectra of 4 nm Fe/GaAs (110) film 1 in the first hour after deposition. (b) Time-dependent FMR of 4 nm Fe/GaAs (110), starting from two hours after deposition with the magnetic field applied parallel to the $[1\bar{1}0]$ direction. Red dots show the resonance field of film 2 at different time intervals. Inset shows the overlapped FMR spectra

of film 1 and film 2 measured after deposition in $[\bar{1}10]$ direction. Single FMR spectra at the 2nd, 12th, and 62nd hour of film 1 are shown separately.

The two resonances are due to the change from a rough surface with larger areas of thinner Fe to a smoother surface with a quasi-uniform thickness of 4 nm [72]. Directly after the preparation of the film, the anisotropy field is given by the roughness of the island-like morphology only. After 4 hours and beyond, the final magnetic surface state forms with the narrower resonance at higher fields as expected for an almost flat film. During the time-dependent evolution, both resonances can be observed because both morphological conditions coexist across the few mm² large areas of the film. As time goes on, the intensity of the second line increases. The substantial shift of the lower resonance field (0.3-0.4 mT/h) in the first 24 hours indicates a rapid morphological change of the Fe film. In this period (10-35 h) these two areas with different roughness are large enough to act as separate magnetic regions that are only weakly coupled to each other. This is also the reason why the upper line is asymmetric [72].

After 30 hours, the rate of resonance field shift decreased to 0.1 mT/h and the two lines are merging as seen in the 62nd FMR spectrum in Figure 4.3. The formation of big terraces (Figure 4.2 (b and c)) is also evidenced by a decrease in the linewidth over time. The apparent change in the resonance field is caused mainly by the change of the anisotropy constants. To confirm this, angular-dependent FMR measurements at different times on another 4 nm Fe film on GaAs (110) named as film 2 grown with the same synthesis conditions were performed. GaAs substrate of film 2 was prepared by annealing at 916 ± 3 K for 30 minutes resulting in the same LEED pattern of GaAs (110) substrate as before. The Fe (4 nm) film 2 was deposited with a rate of 0.081 nm/min and flux of 20 nA. The resonance field of both samples (film 1 and film 2) matches quantitatively as well as qualitatively at $[\bar{1}10]$ direction as shown in the inset of Figure 4.3 (b) and red dots. Therefore, both samples can be easily compared.

The FMR spectra of film 2 were fitted with a complex Lorentz function (equation 5.2) for each in-plane angle. This fit yields the FMR resonance fields, linewidth, and intensity.

The resonance fields were plotted as a function of azimuthal angle and were fitted using free energy density (equation 2.19). All the fits were performed, keeping magnetization $M = 1600$ kA/m and $g = 2.09$, which is close to the Fe bulk value. This fit yields the anisotropy constants of film 2 discussed in section 4.4.

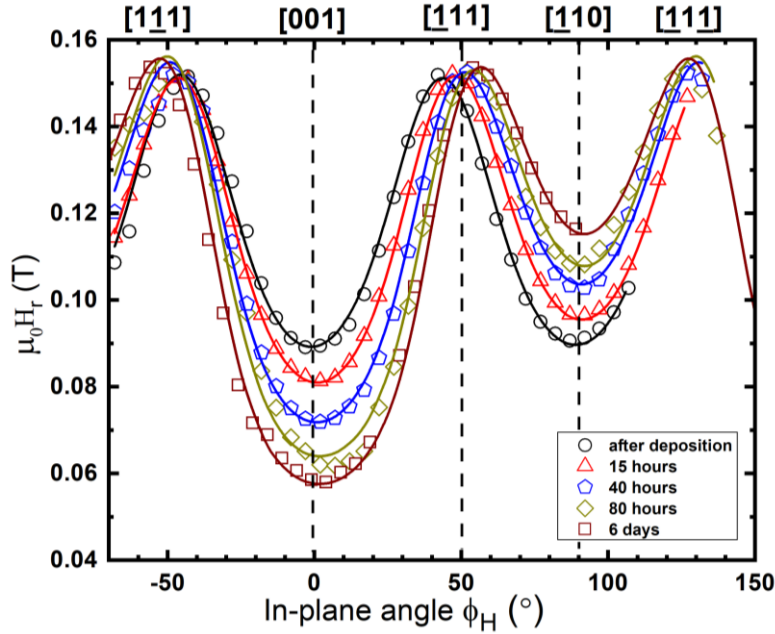


Figure 4.4 Azimuthal angular dependence of the resonance field of 4 nm Fe/GaAs (110) film 2 at a microwave frequency of 13.054 GHz at different times. The solid lines are fit to the experimental data (open symbols) according to equation 2.19 [72].

The in-plane angular-dependent resonance field measured at a microwave frequency of 13.054 GHz at different periods is shown in Figure 4.4. All the angular-dependent FMR measurements were carried out at room temperature (300 K) and UHV conditions ($\leq 2 \times 10^{-10}$ mbar). The microwave power was calibrated to 15.2 dBm and other modulation parameters were the same as before. The two resonances near the $[110]$ direction of the film plane were also obtained for this sample. However, only the prominent resonance peak positions were taken to analyze angular-dependent behavior. The first angular-dependent FMR measurement after deposition (black circles in Figure 4.4) depicts a four-fold-like symmetry which is not expected for a Fe (110) film. The expected (110) crystal symmetry has two-fold geometry with three principal directions namely $[100]$, $[110]$, and $[111]$ as easy, intermediate, and hard axis respectively reported by Roemer et al. [36] and Prinz et al. [73]. However, this is not the case in the black curve of Figure 4.4, which is unusual. Nevertheless,

as time evolves, the expected crystal symmetry slowly grows and becomes visible e.g., after 40 hours (blue curve in Figure 4.4). This indicates that the film is grown on the (110) oriented substrate is initially unstable, but slowly relaxes over time and reaches its final state after several hours. The first 20-30 hours are very crucial in this transformation since the shift of the magnetic resonance line is very fast in this period [72].

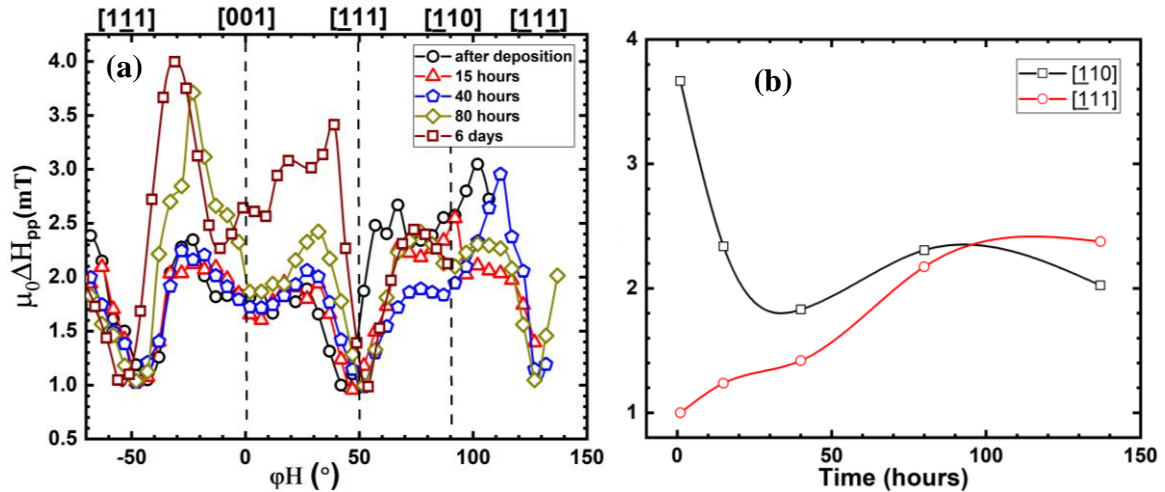


Figure 4.5 (a) Angular-dependent peak-to-peak linewidth of 4 nm Fe/GaAs (110) film 2 at different periods. (b) Linewidth at intermediate and hard direction as a function of time.

The smoothening of the film surface is also supported by the decrease of the linewidth at the intermediate $[110]$ direction and increase of the linewidth in the hard $[111]$ direction after several hours as can be seen in Figure 4.5 (b). Similar behavior was observed for the previous sample measured at $[110]$ direction. The influence of surface roughness on the magnetic properties of thin Co films was reported by Steinmuller et al. [74]. They measured by Brillouin Light Scattering (BLS) the spin-waves dispersion and observed a considerably broader linewidth for the rough film as compared to the flat film. They attributed this broadening to the tilting of the magnetization M following the roughness of the film surface. The tilting of the spins away from the easy axis (a local variation of alignment of M) due to surface roughness will lead to the local variation of the magnetic anisotropy energy, giving rise to new allowed spin-wave modes, increasing the spin-wave peak linewidth inhomogeneously. This model explains that our Fe films in the initial state after deposition with a rough surface have broader linewidths, which gets smoother over time resulting in a decrease of the linewidth. Thus, the changes in resonance field and linewidth are explained

by the island relaxation of the film surface with time at room temperature under UHV conditions.

The AES peaks of Fe film measured after deposition as well as after several days in the UHV chamber are shown in Figure 4.6. The AES peak of Fe at 47 eV is the best surface-sensitive test in terms of changes of the valence band electronic structure of Fe due to oxide formation or chemisorption of other gases (CO, CO₂ for example). It has been shown by Kebe et al. [75] and Smentkowski et al. [76] that the sub-monolayer absorption of oxygen on Fe films and the formation of iron oxides give a significant shift as well as the change in the shape of Fe (47 eV) peak. Furthermore, they also observed a decrease in the magnetization of the Fe film with increasing oxygen exposure. However, in our samples, as can be seen from Figure 4.6, the Fe peak shows no change in shape and shift in energy after 6 days. The small peak of oxygen at 512 eV can be due to a sub-monolayer of weakly bonded CO or CO₂, which shows a slight relative increase in intensity. It is known that at 1.33×10^{-10} mbar pressure (assuming sticking coefficient = 1) inside the chamber, 1 monolayer of contamination will be formed in ~8.4 hours. So, we cannot avoid contamination of any film over time even under UHV conditions. Along with this, the angular-dependent resonance field at different periods does not give any change in magnetization. Therefore, the oxidation of uncapped Fe film over time can be quickly ruled out. Seo et al. [77] found that AES is quantitative with respect to the iron oxides and the amplitude ratio s of O_{510eV}/Fe_{703eV} lines, to a first approximation, is proportional to the relative content of oxygen and iron in the chemical formula. In our case, at first the ratio $s \approx 0.1623$ in deposited Fe film which increases to $s \approx 0.3113$ after 6 days, which indicates a slight increase of oxygen atoms on the film surface after 6 days. However, these values are far below the value obtained by Seo et al. for iron oxides, confirming the absence of Fe oxide.

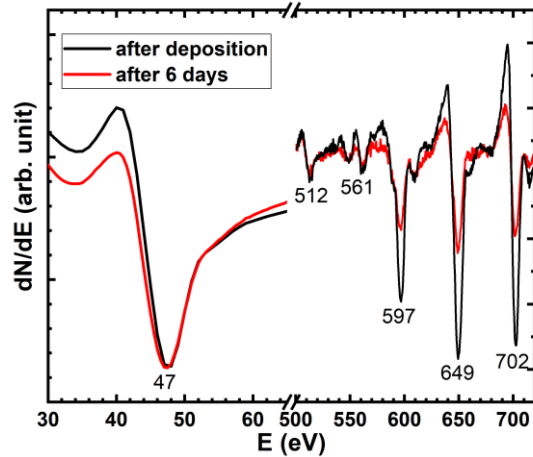


Figure 4.6 AES spectrum of 4 nm Fe/GaAs (110) just after deposition and after 6 days under UHV conditions.

To see if thinner Fe films also have a similar time-dependent structural and magnetic behavior under UHV conditions, two more samples with 2 and 1 nm thickness of Fe were studied in the same way. For the 2 nm Fe/GaAs (110) sample, the substrate was annealed at 940 K for half an hour, and Fe was deposited at a pressure of $\sim 1 \times 10^{-9}$ mbar. The LEED pattern of the substrate after sputter cleaning looks the same as the one of the previous samples (Figure 4.1). AES spectra of GaAs substrate after cleaning gives clear peaks of Ga and As as shown in Figure 4.7 (a). Further, after 2 nm of Fe deposition, no Ga or As peak was seen in AES spectra (even 3 days after deposition). This confirms no out-diffusion or segregation of Ga or As to the Fe film surface. This is because the film growth and all *in situ* measurements are performed at room temperature. The AES peak of Fe at 47 eV (Figure 4.7 (b)) again shows no change with time, confirming no oxidation of the pure Fe film.

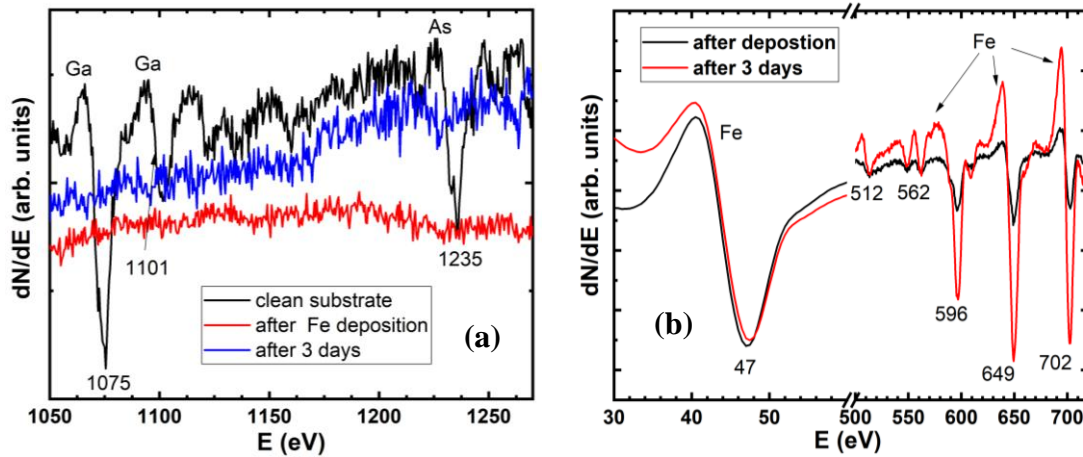


Figure 4.7 AES spectrum (a) showing Ga and As peaks before and after 2 nm Fe deposition on GaAs (110), and (b) showing Fe peaks after deposition and after 3 days in a vacuum.

The *in situ* azimuthal angular-dependent FMR of 2 nm Fe/GaAs (110) taken at a frequency of 12.069 GHz (microwave power = 15.1 dBm) is shown in Figure 4.8. Two resonance lines are observed for this sample also, while only the prominent resonance peak is used for fitting and analysis. It should be noted here that the typical Fe (110) symmetry is already formed after deposition unlike the 4 nm Fe sample, where it took several hours to reach this symmetry. This indicates that the crystal planes being closer to the substrate already align in (110) geometry after deposition. Since the desired crystal symmetry is already formed after deposition, the dynamic relaxation will be faster. However, the energy landscape observed for this sample is not completely symmetric with respect to the easy axis [100] as shown in Figure 4.8 (b). Moreover, the spectra measured for this sample are noisy resulting in a poor signal-to-noise ratio (Figure 4.9 (b)). These effects are due to a large inhomogeneity in the film. Due to noisy resonance lines, it is very difficult to fit with a perfect Lorentz shape to calculate and analyze resonance position and linewidth. Therefore, the prominent peaks were chosen to determine the resonance field from each spectrum. Figure 4.9 (a) shows the angular-dependent resonance field at different times. The shift in the resonance field at the intermediate $[1\bar{1}0]$ direction is in the opposite direction i.e., decreasing to lower field value with time. The resonance field fit was done by using the same free energy density model for Fe (110) described by equation 2.19 to see the change in anisotropy parameters for this thickness (discussed in section 4.4). Two distinct resonance lines visible after deposition at $[1\bar{1}0]$ direction as shown in Figure 4.9 (b) merge to a single

resonance peak after 69 hours indicating smearing of the islands into a quasi-uniform film.

However, the relaxation of islands does not lead to a homogeneous film after 70 hours.

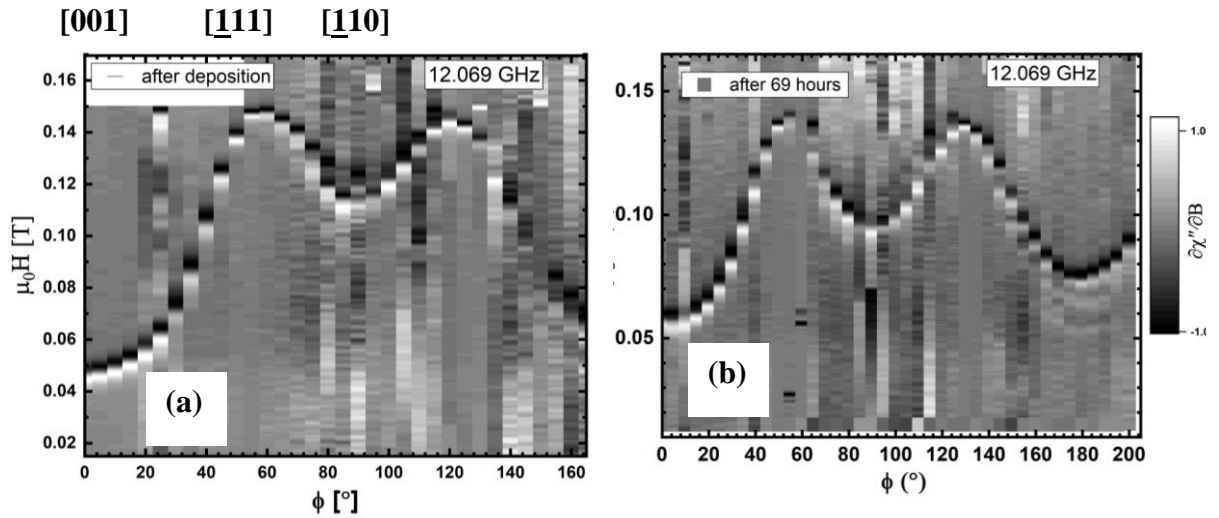


Figure 4.8 Angular-dependent FMR of 2 nm Fe/GaAs (110) measured (a) after deposition and (b) 69 hours after deposition. Greyscale represents the normalized amplitude of microwave absorption.

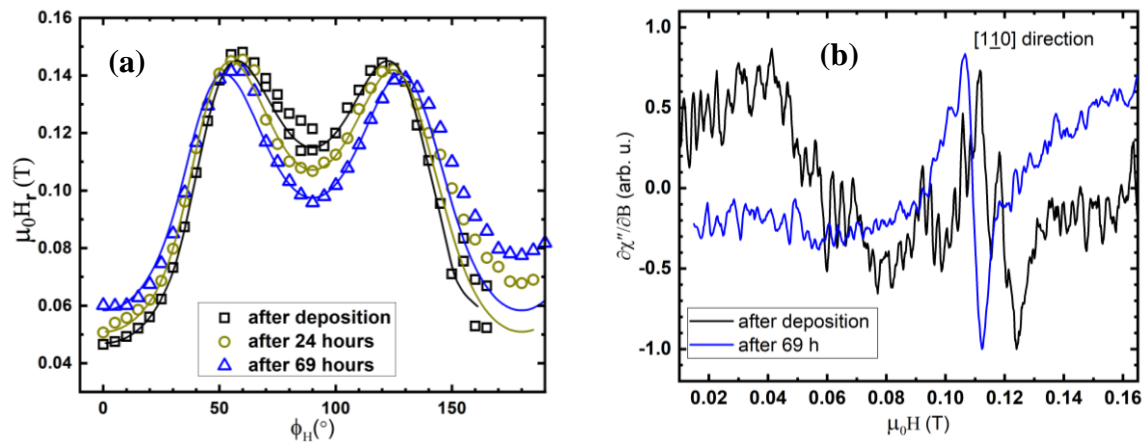


Figure 4.9 (a) Azimuthal angular dependence of the resonance field of 2 nm Fe/GaAs (110) at a microwave frequency of 12.069 GHz at different times. The solid lines are fit to the experimental data (open symbols). Only prominent resonance field positions were selected for fitting purposes. (b) FMR spectra taken at the intermediate direction ($\Phi_H = 90^\circ$) after deposition and after 69 hours.

The next step was to lower the film thickness to 1 nm, where the interfacial effects play a significant role in determining the magnetic properties and observe the time-

dependent transition. The LEED pattern of 1 nm Fe/GaAs (110) is visible as shown in the inset of Figure 4.10 (a) depicting a typical BCC structure. The peak distance ratio was determined using LEED images taken after deposition and after 9 days (not shown here). This ratio is 1.709 ± 0.05 after deposition, while it reduces to 1.423 ± 0.05 after 9 days. It has been found by several groups [78, 79] that the in-plane lattice expansion occurs in the thin Fe film grown in GaAs due to lattice mismatch causing tensile stress. This is also the case here for 1 nm Fe film where initially after deposition the film having tensile stress expands in the in-plane direction giving a bigger lattice distance ratio. But, with time this strain relaxes over time and the crystal symmetry tries to reach back its ideal structure. It has to be noted here that the crystal structure is maintained while the distortions present in the crystal planes are relaxing with time. The in-plane stress and strain are strongly affected by the interdiffusion of substrate Ga and As atoms especially for an ultrathin film [80]. On the other hand, Auger measurements of this sample surprisingly do not show any clear peak of Ga or As (Figure 4.10), indicating no out-diffusion or segregation of substrate atoms at the top of the film. In addition to this, the Auger peak of Fe at 47 eV does not give any shift in energy or change in shape with time confirming no oxidation after 9 days in the vacuum chamber.

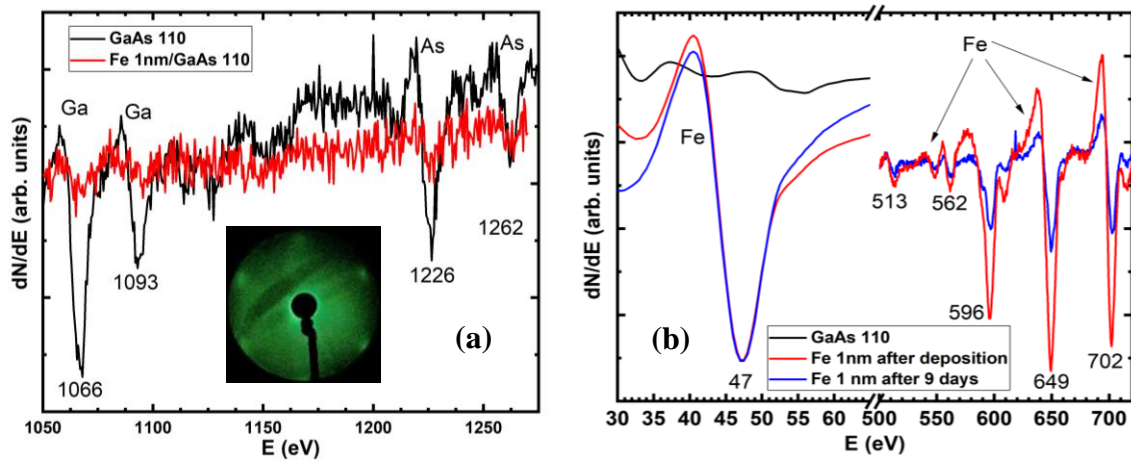
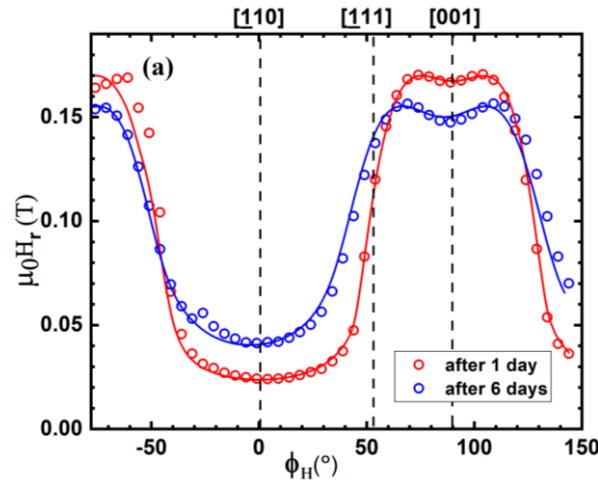


Figure 4.10 AES spectra of 1 nm Fe/GaAs (110) (a) Ga and As peaks before and after deposition. Inset shows the LEED pattern of 1 nm Fe/GaAs (110) taken at 113 eV after deposition. (b) Fe peaks before and after deposition as well as after 9 days in a vacuum.

The *in situ* angular-dependent FMR was measured at a frequency of 12.069 GHz with a microwave power of 13 dBm and a modulation frequency of 9 kHz. In Figure 4.11 (a), the resonance field as a function of the in-plane angle is plotted when measured ~ 24 hours and 6 days after deposition. The easy axis is rotated from its orientation towards $[1\bar{1}0]$ direction

and intermediate axis to [001] direction. This is due to the reorientation transition below critical thickness [15]. The shift of resonance field at intermediate direction [001] is of the same order of magnitude as for 4 nm Fe film (~20 mT) but in the opposite direction. Similarly, the resonance field at easy direction [110] is moving to a higher field instead of decreasing with time in the case of a 4 nm sample. The principal directions of the Fe (110) plane seem to shift with time. This is another indication that the crystal symmetry is relaxing over time by reducing the in-lattice expansion. The angular-dependent linewidth plot of 1 nm Fe (110) is shown in Figure 4.11(b). The variation of ΔH around [110] direction is larger than around [111] direction due to larger uniaxial anisotropic field. This is an indication of anisotropic damping at reduced Fe thickness as found in Fe/GaAs (100) [17]. There is no second resonance line observed in any direction for this sample as shown in Figure 4.11 (c), which indicates a homogenous film growth (signal to noise ratio for this sample was much higher than for the 2 nm sample). A clean FMR spectra of 1 nm~5 ML Fe film indicates a good quality microwave short which can detect few atomic layers of ferromagnetic film with a large sensitivity.



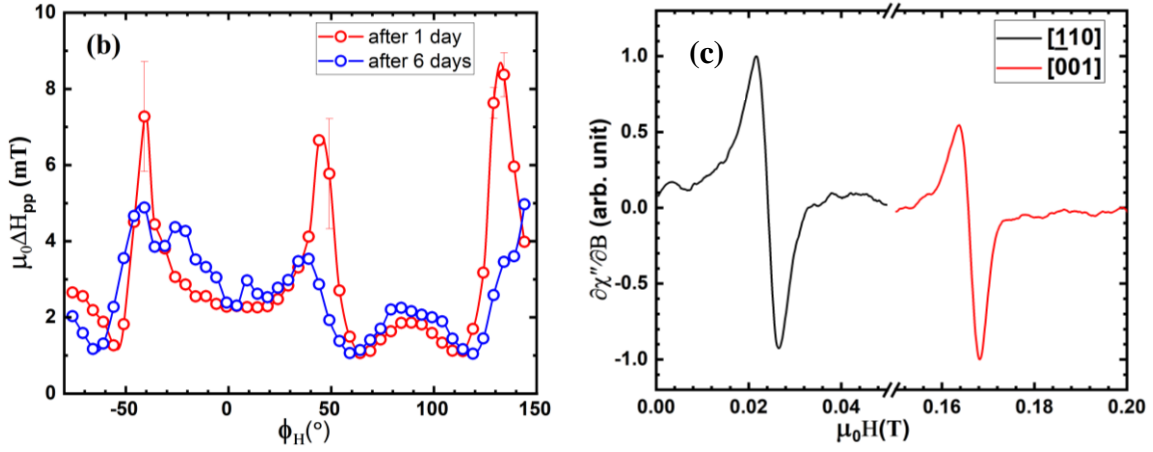


Figure 4.11 (a) Azimuthal angular dependence of the resonance field of 1 nm Fe/GaAs (110) at a microwave frequency of 12.069 GHz taken one day and 6 days after deposition. Open symbols are the experimental data, and the solid lines are the fit according to equation 2.19. (b) Angular-dependent linewidth of 1 nm Fe/GaAs (110) at different times. (c) FMR spectra of 1 nm Fe/GaAs (110) measured *in situ* after 1 day in $[1\bar{1}0]$ and $[001]$ directions.

4.4 Magnetic anisotropy as a function of time in Fe/GaAs (110)

The angular-dependent resonance field was analyzed using equation 2.19 for all three samples (1, 2, and 4 nm Fe/GaAs (110)) to determine in-plane and out-of-plane anisotropy constants. All the fits were performed assuming magnetization $M = 1600$ kA/m and g-factor 2.09 (bulk Fe), except for the 1 nm Fe sample where $M = 1570$ kA/m was used. The anisotropy parameter plot as a function of time for three thicknesses is shown in Figure 4.12. The change in four-fold cubic anisotropy $K_{4\parallel}$ over time is only 2-3% for 2 and 4 nm samples and $\sim 8\%$ for 1 nm sample. It is another confirmation for a stable cubic crystal structure of uncapped Fe films grown on GaAs (110) for all the thicknesses with time. The change of the out-of-plane uniaxial anisotropy $K_{2\perp}$ is only $\sim 3\%$ in the 1 nm Fe sample, indicating no significant contribution from the surface. It again confirms the homogeneity of thin film which remains stable over time. Similarly, there is only a $\sim 4.5\%$ decrease of $K_{2\perp}$ in 2 nm Fe sample after 69 hours and $\sim 10\%$ decrease in 4 nm Fe sample after 6 days. This is due to the rough surface morphology of these films, which gets smoother over time, reducing the surface contributions. Fe/GaAs and volume are not expected to relax over time, only Fe/vacuum interface is contributing to $K_{2\perp}$ giving a small change. Hence, we can conclude

that there is no significant effect on cubic and out-of-plane uniaxial anisotropy with time. The energy which is predominantly active during surface relaxation is the volume in-plane uniaxial anisotropy.

The in-plane uniaxial anisotropy $K_{2\parallel}$ gives a dramatic change over time for 4 nm Fe film with a sign reversal after 30 hours. Such a unique time-dependent change in the in-plane uniaxial anisotropy is very unusual for a Fe film at a constant thickness and temperature. This change is attributed to the process of surface relaxation, i.e., morphological changes occurring on the film surface at room temperature. We assume that the smoothening of the film surface takes place and the formation of the flat terraces within the initially rough film similar to that mentioned in [32] causes the change in the in-plane surface anisotropy [81] and continuous increase in the in-plane uniaxial anisotropy with a sign change [15, 81]. The free energy density behaviour in Fe (110) [81] matches qualitatively with our resonance line fit (Figure 4.4, solid lines). The thickness 4 nm is in the critical thickness range, where the spin reorientation of the easy axis occurs resulting in the sign change of the uniaxial anisotropy [16]. The slow relaxation over several days is since the magnetic system is kept under UHV conditions at room temperature. Annealing the sample can make the process faster but it will also introduce intermixing effect at the surface and interface [82], resulting in the modification of the crystallinity. In case of 1 nm, and 2 nm Fe (110) films there is a decrease of $K_{2\parallel}$ over time of 26%, and 68% respectively. Moreover, the transition over time in these films is much faster as compared to 4 nm film. This is because of the strong interfacial effects at Fe/GaAs interface and expected crystal symmetry of Fe (110) is already formed after deposition.

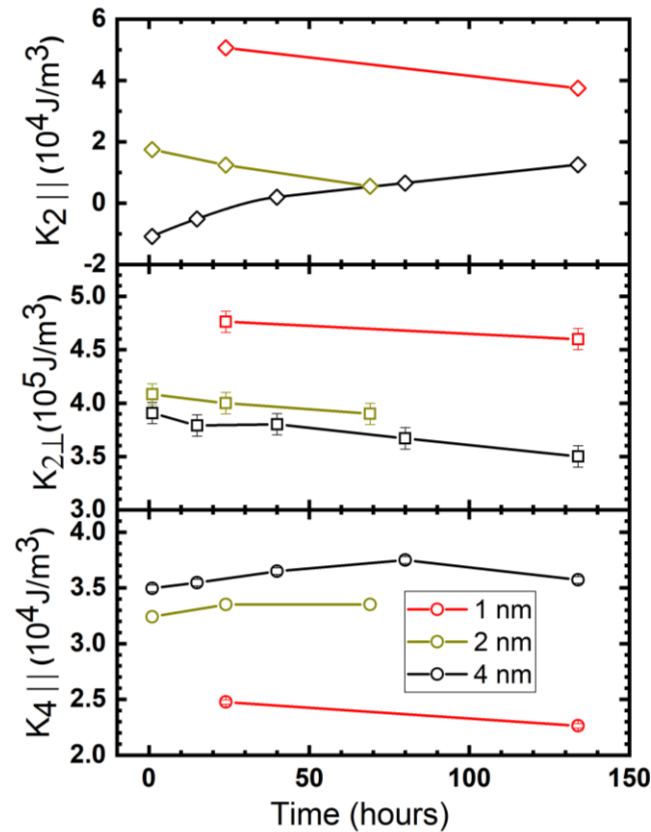


Figure 4.12 Anisotropy constants of Fe/GaAs (110) as a function of time for different thicknesses of Fe. The error bars of $K_{2||}$ are smaller than the symbol size ($\pm 0.05 \times 10^4$ J/m³).

4.5 Time-dependent structural and magnetic stability of Fe/GaAs (100)

GaAs (100), unlike (110) exhibits a range of surface reconstruction e.g., 2x4, 4x6, 2x6, depending on the substrate preparation and growth conditions [83]. This surface reconstruction has a significant effect on the initial growth morphology as well as the growth mode of Fe on GaAs (100). Depending on the chemical bonding and the surface free energy, either a Ga or As-rich surface termination is formed on GaAs (100). The substrate surface termination/reconstruction also decides the initial nucleation and growth of Fe [66, 84] and interdiffusion at the interface of Fe/GaAs (100) [23]. The preparation of the substrate GaAs (100) is similar to described in section 4.2, with an annealing temperature of 960 K. After cooling the substrate down to room temperature, the LEED pattern shows a (1x6) reconstruction, as shown in Figure 4.13 (b) taken at an energy of 63 eV. Figure 4.13 (a) shows the Auger spectra of the GaAs (100) substrate after sputter cleaning. A small carbon

peak at 283 eV and oxygen peak at 524 eV is still there along with all Ga and As peaks in the higher energy range. It has been found for other samples that further sputtering or heating leads to a very rough surface resulting in broad LEED spots and highly noisy Auger peaks. Therefore, no further treatment was done on the substrate. A 4 nm Fe film was deposited on this substrate at a rate of 0.1 nm/min, as described in section 4.2. Figure 4.14 shows the Auger spectra and LEED pattern taken after Fe film deposition. A 1x1 LEED pattern is obtained, showing a cubic (100) face of BCC structure with a lattice distance ratio of 1.02 ± 0.05 . Fe peaks are clearly seen in the Auger spectra of Fe/GaAs (100). After LEED and Auger measurement, the sample was transferred to the FMR position for magnetic measurement without any capping layer on top of it. The FMR spectra were taken every hour at room temperature to observe the time-dependent behavior of magnetic properties under UHV conditions. Since more than 30 minutes are spent in LEED, Auger measurement, and transfer of sample, the first FMR spectrum is recorded after 50 minutes.

Figure 4.15 (a) shows the two initial FMR spectra taken at 12.931 GHz with the magnetic field applied parallel to the [110] direction of Fe. The microwave power and modulation parameters are the same as the ones used for 4 nm Fe/GaAs (110) (section 4.3). The resonance line shape, as well as the resonance field (130 mT fit by complex Lorentz) after 100 minutes, is the same as after 50 minutes. The two resonance spectra are lying on top of each other with no change after 50 minutes in a vacuum ($< 2 \times 10^{-10}$ mbar). It indicates that there is no change in the magnetic properties of 4 nm Fe film grown on GaAs (100) within 1.5 hours after deposition. Figure 4.15 (b) shows further FMR spectra as a function of time in a greyscale plot where greyscale represents the normalized amplitude of $\partial\chi''/\partial B$. The filled red circles indicate the resonance field position of each spectrum. The resonance field decreases very slowly from 130.20 mT to 129.87 mT in 36 hours. The shift in the resonance field is only 0.33 mT after 36 hours in a vacuum. This indicates that the uncapped Fe (100) film is magnetically stable at room temperature under UHV conditions. This is due to the layer-by-layer growth of the Fe film on GaAs (100) substrate. The growth mode of Fe for (100) GaAs substrate gives a uniformly flat film with a surface roughness of 0.82 nm measured by AFM scan as shown in Figure 4.16 (b). The linewidth extracted from FMR spectra as a function of time is shown in Figure 4.16 (a). A tiny increase (less than 1%) in the linewidth after 36 hours reveals the stable magnetic relaxation of Fe film over time.

Hence, uncapped 4 nm Fe film grown on GaAs (100) is magnetically and structurally stable at room temperature under UHV conditions for more than 35 hours.

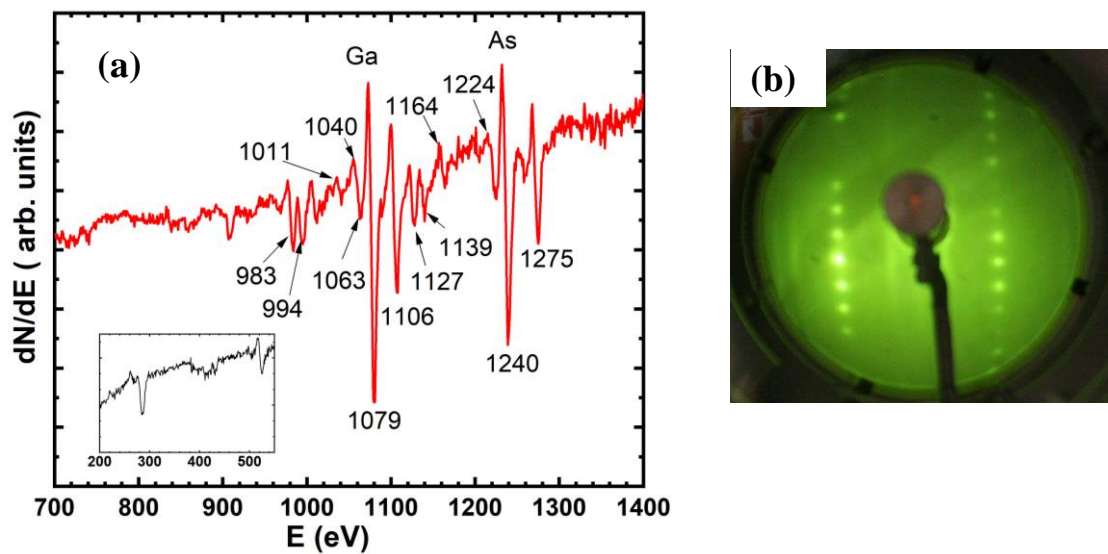


Figure 4.13 (a) Auger spectrum of a clean As-rich GaAs (100) substrate surface. The numbers show the energy in eV of Ga and As peaks. The inset shows the spectrum of the same substrate recorded at lower energies indicating the presence of carbon and oxygen. (b) A LEED pattern of ordered (1×6) reconstructed GaAs (100) substrate taken at an energy of 63 eV.

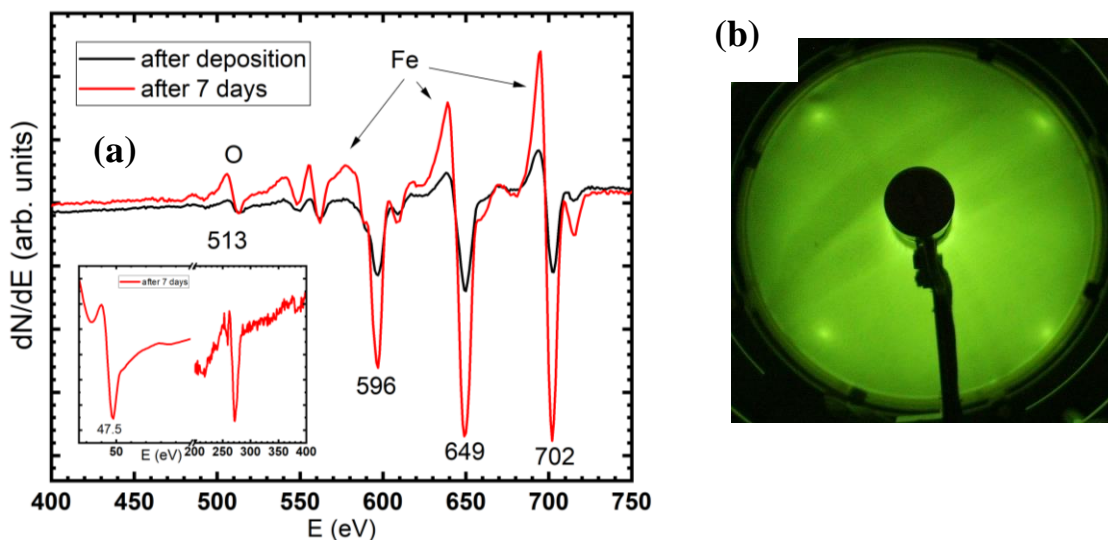


Figure 4.14 (a) Auger spectrum of 4 nm Fe/GaAs (100) just after deposition and 7 days after deposition. Inset of (a) shows the lower energy scan taken 7 days after deposition. (b) A LEED pattern of 4 nm Fe/GaAs (100) taken at an energy of 117 eV showing a well-ordered BCC structure.

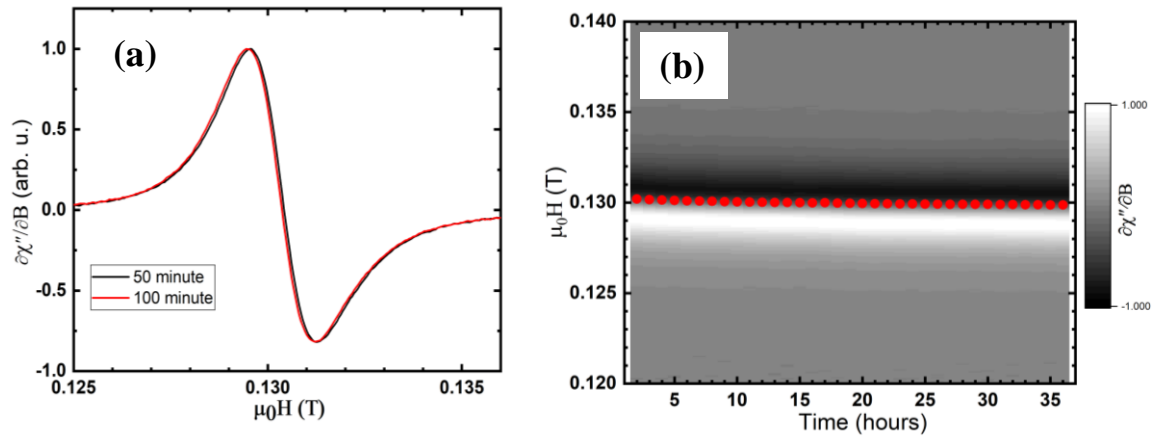


Figure 4.15 (a) FMR spectra of 4 nm Fe/GaAs (100) taken in [110] direction 50 minutes and 100 minutes after deposition (b) Time-dependent FMR of 4 nm Fe/GaAs (100) taken at room temperature and 12.931 GHz two with the magnetic field applied parallel to [110] direction. Greyscale reflects the normalized amplitude of the microwave absorption derivative, which is proportional to $\partial\chi''/\partial B$. Red dots show the resonance field position $\mu_0 H_r$ of each spectrum. The error bars of $\mu_0 H_r$ (red dots) are smaller than the symbol size.

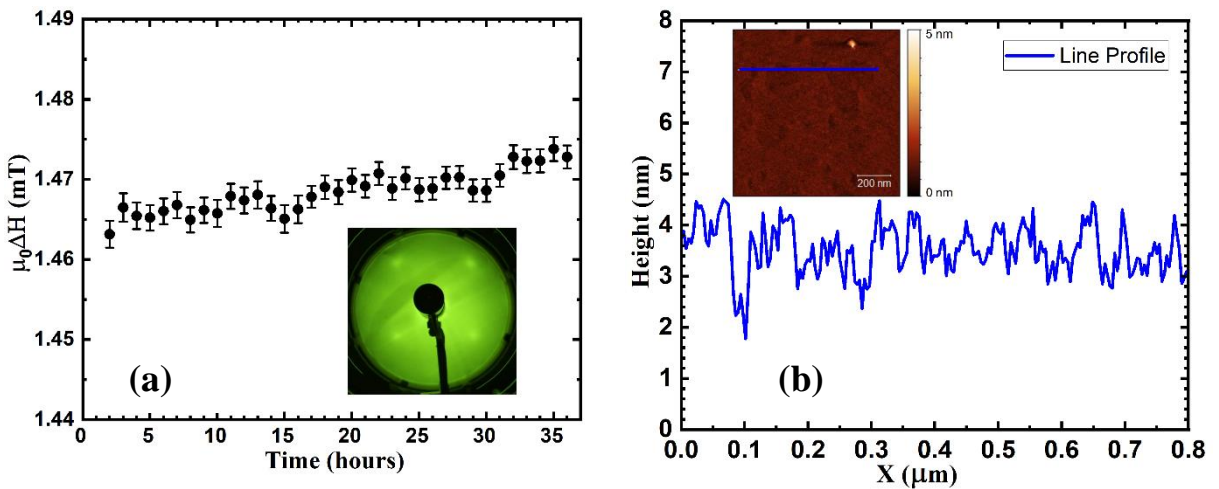


Figure 4.16 (a) Time-dependent FMR linewidth of 4 nm Fe/GaAs (100). Inset shows the LEED pattern of 4 nm Fe/GaAs (100) on the 7th day after deposition taken at 207 eV. (b) *Ex situ* AFM scan of same film (1×1 μm area) oxidized in air and line profile of the blue line in the image.

The LEED pattern taken seven days after deposition, as shown in the inset of Figure 4.16 (a) depicts a cubic (100) plane of BCC structure with a lattice distance ratio of

1.03 ± 0.03 again. This confirms that the cubic crystal structure of the uncapped 4 nm Fe film surface is maintained after 7 days under UHV conditions. However, the LEED spots observed after 7 days are a little broader as compared to the ones obtained after deposition. It is due to the adsorption of gases, which are unavoidable even under UHV conditions. This is also visible in the Auger spectra taken after 7 days from deposition, as shown in Figure 4.14 (a) and inset, where carbon and oxygen peaks are obtained at 271 and 512 eV, respectively. Nevertheless, this minor contamination does not disturb the crystal structure and stability of the film.

4.6 Comparison of Fe (100) and Fe (110)

Having established that the structural and magnetic properties of Fe are significantly affected by the surface reconstruction of GaAs [16, 30], we can compare the Fe/GaAs (100) with Fe/GaAs (110) system. Notably, the growth mode of the Fe film is different on GaAs (100) and GaAs (110). The difference comes from the surface reconstruction of GaAs for two different orientations. GaAs (100) with (1x6) surface reconstruction has As dimer rows along the [110] direction giving initially nucleation of Fe clusters followed by percolation of layer-by-layer growth on Fe (001). This reconstruction also gives rise to tetragonal distortions of the Fe crystal at the interface resulting in uniaxial in-plane anisotropy in Fe (100) film. On the other hand, GaAs (110) with no surface reconstruction gives 3D island growth with a change of morphology with increasing thickness. These differences in the film morphology result in dissimilar time stability. Fe (100) is magneto-structurally more stable than a Fe (110) film under UHV conditions at room temperature.

The FMR measurement of both Fe (100) and Fe (110) films with nominally the same thickness can be compared. Table 4-1 gives the resonance field and linewidth at different times. Both samples have completely different values at a particular point of time after deposition showing different magnetic behavior due to dissimilarities in growth and structural properties. Thus, we conclude that the time-dependent study on Fe films grown on GaAs with two different orientations gives fundamental information about the aging of Fe films which can be utilized for tuning the magnetic anisotropy.

Structural and magnetic characterization of Fe on GaAs (100) and (110) as a function of time

Sample	Time	$\mu_0 H_r$ (mT)	$\mu_0 \Delta H_{pp}$ (mT)
4 nm Fe\GaAs (100)	50 minutes	130.3	1.46
	100 minutes	130.2	1.46
	37 hours	129.8	1.47
4 nm Fe\GaAs (110) film 1	50 minutes	89.1	1.87
	100 minutes	89.4	1.81
	37 hours	109.5	2.71

Table 4-1 Comparison between two samples of resonance field and linewidth measured along [110] direction at different times. The error bars for all the values are less than 1%.

5 Influence of capping layer on the magnetic properties of Fe/GaAs (100)

In this chapter, the experimental results of *in situ* LEED, AES, and FMR of an epitaxial 5 nm Fe film grown on GaAs (100) with and without a capping layer are presented. Ag and Pt capping modifies the surface anisotropy and spin-orbit coupling at the interface of the Fe film. The in-plane angular-dependent FMR of the uncapped 5 nm Fe film was measured *in situ* to calculate the magnetic anisotropy parameters and compare it with the anisotropy constants of a Fe film capped with 2 nm Ag and 3 nm Pt measured *ex situ*. The g-factor, which is related to spin-orbit coupling parameter, Gilbert damping, and the spin pumping contributions were determined for uncapped and capped Fe film by frequency-dependent FMR.

5.1 Fabrication and characterization of the sample

A commercial $4 \times 4 \text{ mm}^2$ and 0.5 mm thick undoped GaAs (100) wafer was used as a substrate. The substrate was pre-cleaned with absolute ethanol in an ultrasonic bath and verified in an optical microscope for a scratch-free surface. After this, the substrate is pasted on the sample holder using silver paste and heated up to 150 °C for drying. This sample is transferred to the UHV chamber through the transfer mechanism, and the sample preparation process was carried out. The characterizations performed at each step of the sample preparation are schematically shown in Figure 5.1. The base pressure of the UHV chamber was 9.8×10^{-11} mbar. The surface of the substrate was prepared by sputtering at an energy of 1 keV (ion etching with argon gas) at partial pressure of 1×10^{-6} mbar and heating up to 920 K. Sputtering and heating for 1 hour and subsequent annealing at 920 K for 10 minutes were performed. LEED images were taken of the clean GaAs (100) substrate at 3.6×10^{-9} mbar. The substrate preparation yields a combination of $\{1 \times 6\}$ and $\{4 \times 6\}$ reconstruction of GaAs (100) surface, as shown in Figure 5.1 (a) and a*. There can be a random coalescence of domains with two different reconstructions of GaAs (100) [85].

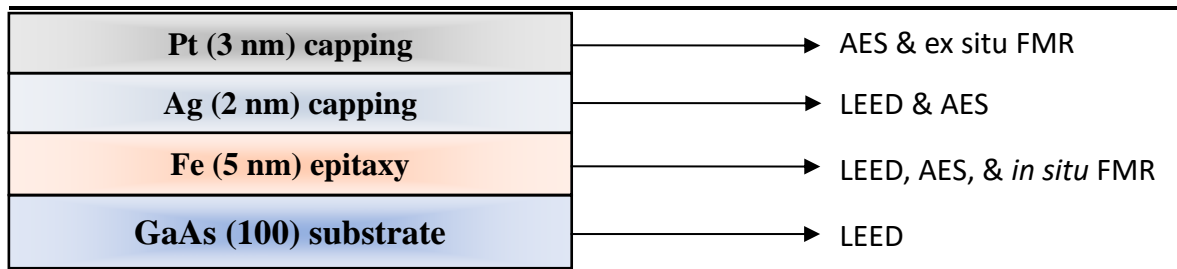


Figure 5.1 Schematic of prepared sample and characterization followed the sample preparation *in situ* and *ex situ*.

The Fe film of thickness 5 nm was grown on the prepared substrate at room temperature with a deposition rate of 0.11 nm/min observed with the quartz monitor. LEED images were taken after Fe deposition to verify the epitaxial growth. Sharp LEED spots of the Fe film, as shown in Figure 5.2 (b), (c), indicate an excellent epitaxial growth of BCC Fe on GaAs (100). Fe's 1×1 LEED pattern with an aspect ratio of 1.02 ± 0.05 confirms perfect cubic (100) BCC structure. AES was also measured after LEED of Fe film at 2.6×10^{-9} mbar and room temperature. The Auger peaks of Fe at 47 eV and 704 eV are clearly visible in Figure 5.3 (a) and (b). After Auger measurement, the sample was transferred to the FMR position for angular- and frequency-dependent FMR measurements with an external field applied parallel to the film plane. The pressure during FMR measurements was between 7×10^{-10} and 7×10^{-11} mbar.

After all the FMR measurements on uncapped the Fe film had been performed (100 hours in total), the sample was transferred back to LEED and deposition position. The LEED image taken after 101 hours at 176 eV (Figure 5.2 (d)) shows a very similar pattern with an aspect ratio of 1.03 ± 0.05 , confirming no structural (lattice distance) change of film surface with time. As was summarized in Chapter 4.5, the magnetic properties measured during this time can be considered as stable for the uncapped Fe film under UHV condition at room temperature. 2 nm Ag film was deposited on top of the Fe film at room temperature with a deposition rate of 0.11 nm/min. The lattice parameter of FCC Ag (4.085 \AA) is close to the Fe lattice constant multiplied by $\sqrt{2}$, therefore Ag film can be grown epitaxially with 45° in-plane structure rotation with respect to Fe.

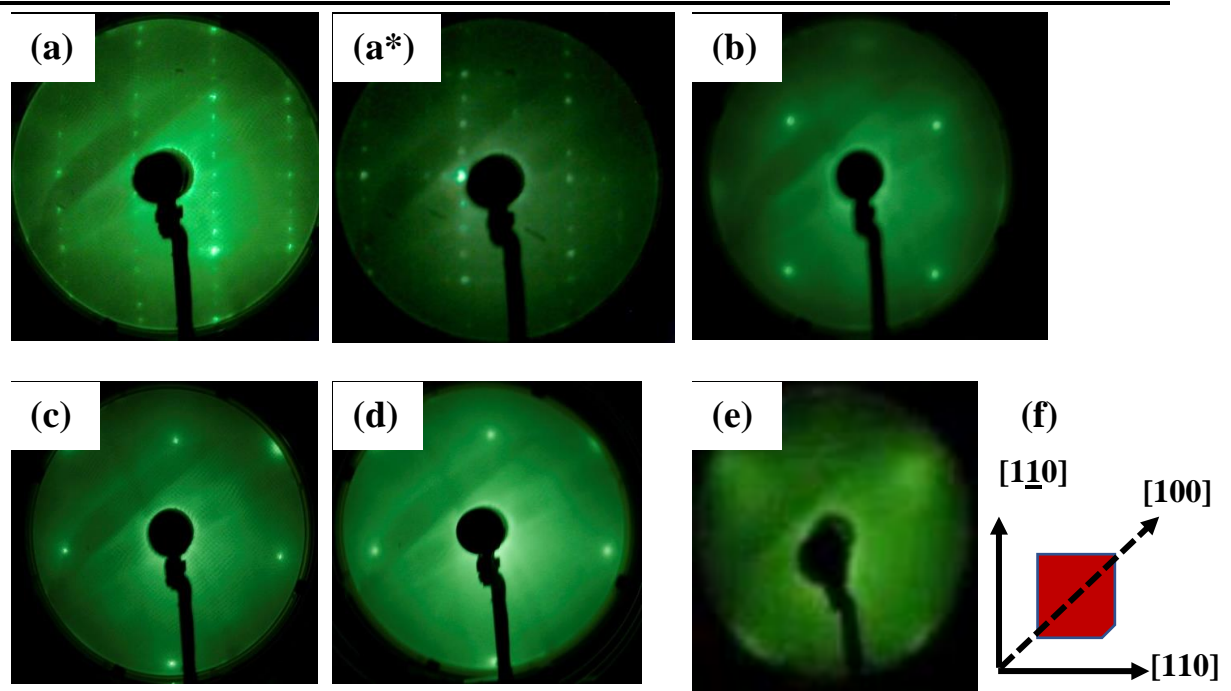


Figure 5.2 LEED image of (a) GaAs (100) at 108 eV, (a*) GaAs (100) at 64 eV, (b) 5 nm Fe/GaAs (100) at 116 eV, (c) 5 nm Fe/GaAs (100) at 176 eV, (d) Fe/GaAs (100) at 176 eV after 101 hours, (e) 2 nm Ag on 5 nm Fe/GaAs (100) at 62 eV, (f) crystallographic directions of GaAs (001).

Figure 5.2 (e) shows the LEED pattern taken after Ag deposition at an energy of 62 eV. It indicates a diffusive crystal growth of Ag on Fe film because of low Ag thickness (2 nm \approx 10 ML). The sharpness of LEED spots indicates the lateral periodicity of atomic terraces, and the length of atomic terraces is given by the coherence length of the electron beam at 100 eV. Therefore, diffusive growth would mean that the lateral epitaxy is absent. After Ag deposition, the Auger measurement indicates a clear Ag peak at 352 eV, as shown in Figure 5.3 (a). Since the Auger electron beam (3 keV) can penetrate up to 5 nm of the film, Fe peaks were also visible at higher energy, as shown in Figure 5.3 (b). Along with the Fe peak, the oxygen peak at 512 eV is also observed, which can be due to contamination at the surface during FMR measurement. It would require roughly 2.8 hours for a monolayer of contamination to deposit on the surface of a prepared film at a pressure of 1.33×10^{-10} mbar. This means that the film will have several monolayers of contamination even at UHV conditions after a few hours. For example, during 100 hours of FMR measurement, the Fe film will have \sim 35 ML of contamination on top which can be mainly

associated with H₂, CO, CO₂, if the sticking coefficient is one for all coverage. However, with a higher coating with gas, the sticking coefficient gets smaller.

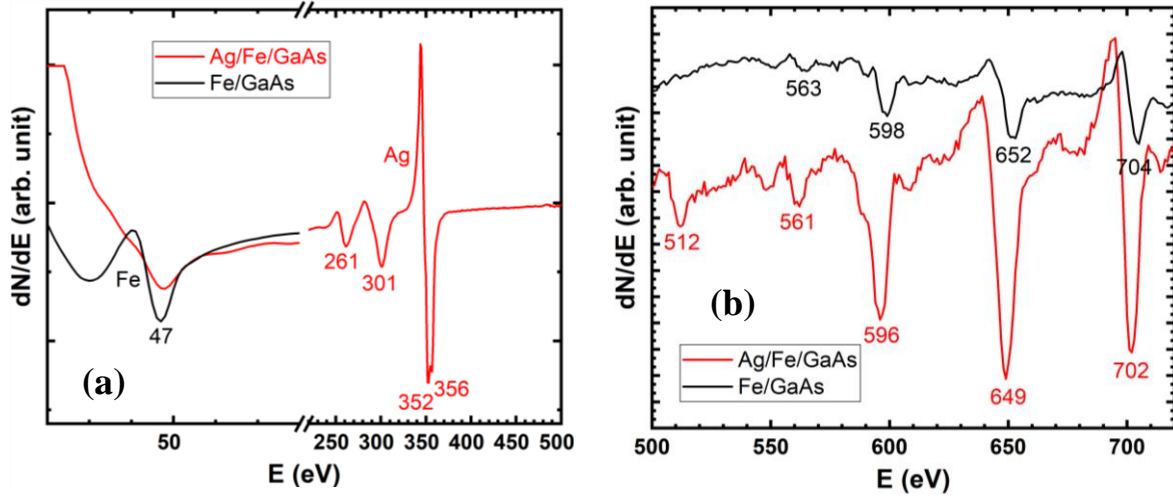


Figure 5.3 AES of 5 nm Fe on GaAs (100) taken after Fe deposition and after 2 nm Ag deposition.

After LEED and Auger measurement, a 3 nm Pt capping layer was deposited on top of Ag at a rate of ~ 0.07 nm/min on the same day to prevent oxidation of Ag. The lattice parameter of FCC Pt (3.92 \AA) provides a significant lattice mismatch (4.0%) between Ag and Pt. This does not allow epitaxial growth of Pt on Ag (100) surface. The larger atomic size of Pt (Van der Waals radius = 175 pm) also gives various dislocation planes in the film. Therefore, no LEED pattern is seen after Pt deposition. Figure 5.4 (a) and (b) shows the Auger scan of the complete sample Pt/Ag/Fe/GaAs (100) taken a day after Pt deposition at room temperature. Carbon peaks are observed along with Pt and Ag in the Auger spectrum, which is unavoidable even at UHV conditions. To clean the sample surface, 10 minutes of ion etching with Argon gas was performed at an energy of 1 keV with a partial pressure of 1×10^{-6} mbar at room temperature. AES taken after sputtering is shown in Figure 5.4 (a) and (b) (red line). The ratio of carbon to Pt AES peaks amplitude gets smaller after sputtering the sample, indicating the reduction of carbon. Capped sample Pt/Ag/Fe/GaAs (100) was taken out from the UHV chamber for *ex situ* FMR measurements using the coplanar waveguide set-up explained in section 3.4.2.

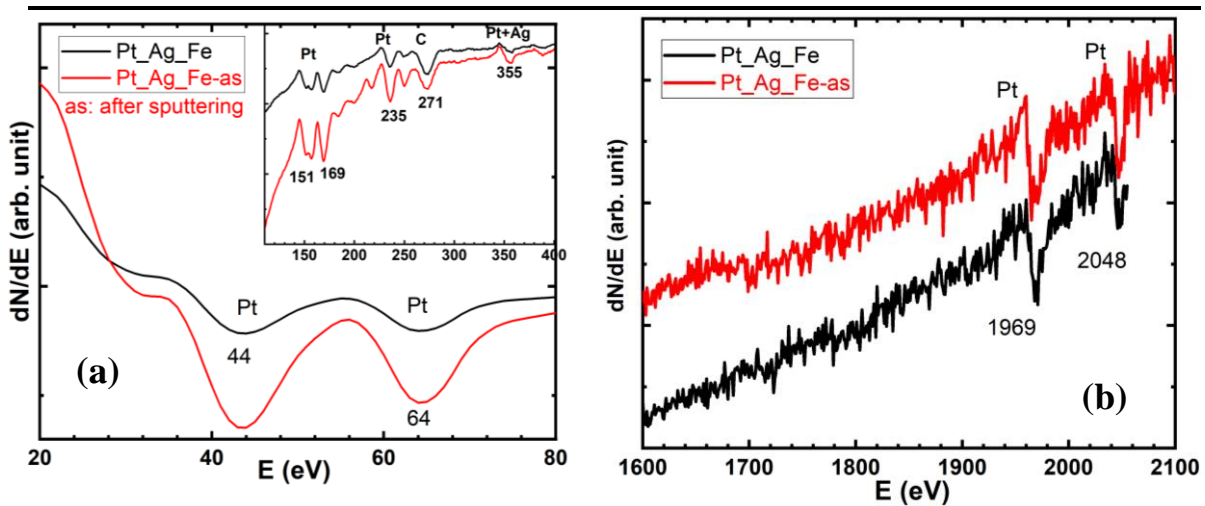


Figure 5.4 AES of 3 nm Pt/Ag/Fe/GaAs (100) taken after Pt deposition and after 10 minutes sputtering at room temperature.

5.2 Magnetic anisotropy with and without capping layer

In-plane angular-dependent FMR measurements were performed on uncapped and capped samples at room temperature to determine the magnetic anisotropy constants. The uncapped Fe film was characterized using *in situ* FMR (section 3.3.3) under UHV conditions, whereas the capped Fe film was measured using the *ex situ* CPW set up (section 3.4.2), both at a microwave frequency of ~ 13 GHz with an external magnetic field applied parallel to the film plane. For *in situ* FMR measurements, the modulation frequency and amplitude of 9 kHz and 2 mT were used, respectively, with a calibrated microwave power of 13.4 dBm. For *ex situ* FMR, the modulation frequency and amplitude were set to 12.1 kHz and 2 mT, respectively, and calibrated microwave power of 8.4 dBm was used. The time constant and conversion time on the lock-in amplifier was set to 40.96 ms and 81.92 ms, respectively for both *in situ* and *ex situ* measurements. Microwave absorption spectra were recorded at fixed microwave frequency, calibrated before each set of measurements, and sweeping the external magnetic field. The specimen was rotated with respect to the magnetic field for the in-plane FMR angular-dependent measurement.

Figure 5.5 shows the normalized amplitude of FMR spectra (open circles) and complex Lorentzian lines fit (solid lines) for the uncapped and capped Fe film at three different

crystallographic directions according to Figure 5.2 (f). The signal in FMR spectra is proportional to $\partial\chi''/\partial B$ (χ'' = imaginary part of magnetic susceptibility, $B = \mu_0 H$). A complex Lorentzian function [86] (equation 5.1) with a phase factor ϕ describes a resonance curve where ϕ can arise from the phase shift between microwave source and detected signal [87].

$$L_c(H) = \frac{A_c[\Delta H \cos \phi + (H - H_{res}) \sin \phi]}{\Delta H^2 + (H - H_{res})^2} \quad (5.1)$$

where A_c is the complex amplitude, H_{res} denotes the resonance field position $B_{res} = \mu_0 H_{res}$, and ΔH is the linewidth $\Delta H = \frac{\sqrt{3}}{2} \Delta H_{pp}$. The asymmetry in FMR lineshape can arise from eddy currents [88]. Modulation of the external magnetic field is used to enhance the signal-to-noise ratio of the signal which results in the derivative of the signal being measured. An asymmetric lineshape can also be observed if the sample surface has a slight tilt with respect to stray field direction (the x - y plane in our case). For *in situ* FMR measurement a perfect horizontal alignment of the sample holder in the x - y plane is difficult. The effect of distance on the stray field causes an asymmetric lineshape. The lineshape also becomes asymmetrical when the magnetization direction is not parallel to the scanning direction. The field derivative of a complex Lorentzian function (equation 5.1) is given by:

$$\frac{dL_c(H)}{dH} = \frac{2A(-H + H_{res})\Delta H \cos(\phi) - A(H - H_{res} - \Delta H)(H - H_{res} + \Delta H)\sin(\phi)}{((H - H_{res})^2 + \Delta H^2)^2} \quad (5.2)$$

This derivative function (equation 5.2) has been utilized to fit the resonance lineshape as shown in Figure 5.5 to determine the amplitude A , resonance field $\mu_0 H_r$, and linewidth ΔH . The resonance field position at [110] direction of uncapped 5 nm Fe/GaAs (100) film $\mu_0 H_r = 135 \text{ mT}$ shown in Figure 5.5 agree well with the resonance field value of 4 nm Fe/GaAs (100) sample produced for time dependent study discussed in section 4.5 $\mu_0 H_r = 130 \text{ mT}$ shown in Figure 4.15. This suggests that good quality Fe films are easily reproducible in the UHV set-up.

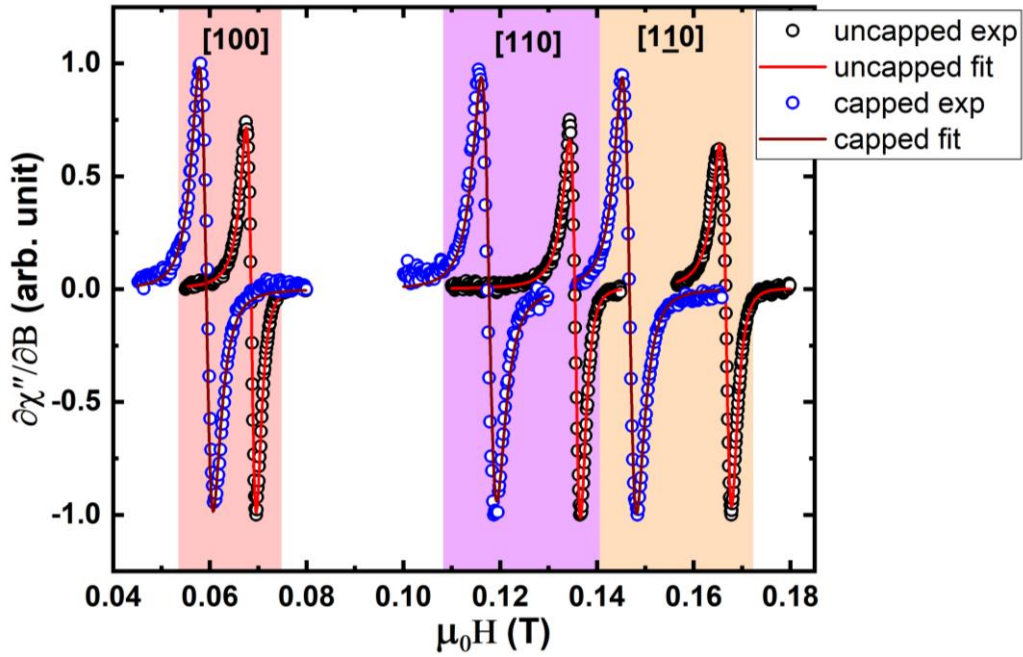


Figure 5.5 FMR spectra of the uncapped and capped 5 nm Fe/GaAs (100) film in three different crystallographic directions of the sample, as shown in Figure 5.2(f).

As shown in Figure 5.6, there is a clear shift of resonance position to lower field value while going from uncapped film to capped film. The decrease in the resonance field can be due to i) the magnetization changes or ii) the change in magnetic anisotropy. Zakeri et al. [65] studied the influence of the Ag capping layer on the magnetic anisotropy of Fe/GaAs (100) using *in situ* FMR. They found a reduction of the Curie temperature of a 2.8 ML Fe film after 1 ML Ag capping. The reduction of the Curie temperature to about 195 K was observed along with the decrease of the magnetization of the thin film. However, this effect occurs only for such thin Fe films, as shown in [89]. For Fe film thicker than 7 ML, the magnetization is close to the bulk value (1.71×10^6 A/m) [62, 90] and remains constant for thicker films. Hence, the change in magnetization for the 5 nm (~35 ML) Fe film after Ag capping is negligible. The only possible reason for the shift in the resonance field after capping is the change of magnetocrystalline anisotropy. To determine the effect of the capping layer on the magnetic anisotropy parameters, angular-dependent FMR data were analyzed.

Figure 5.6 shows 180° azimuthal angular-dependent resonance field $\mu_0 H_r$ of the uncapped and capped Fe film (open circles) and fit (solid lines) to the data according to the free energy density equation 2.18. The exact microwave frequency used to measure the uncapped sample (*in situ* FMR) was 13.069 GHz and for capped sample (*ex situ* FMR) was 13.009 GHz. A slight difference of 60 MHz will not give a considerable shift of the resonance field. The fit has been performed assuming a constant magnetization $M = 1.6 \times 10^6$ A/m and g-factor $g = 2.09$. The easy axis of magnetization M at zero field is [100] direction. The magnetic anisotropy constants determined for uncapped and capped Fe films are given in Table 5-1. Since Fe and Ag are immiscible [91], a sharp interface between Fe/Ag at equilibrium is expected [92]. Therefore, no noticeable change in the structural and magnetic properties after Ag capping on Fe film is expected.

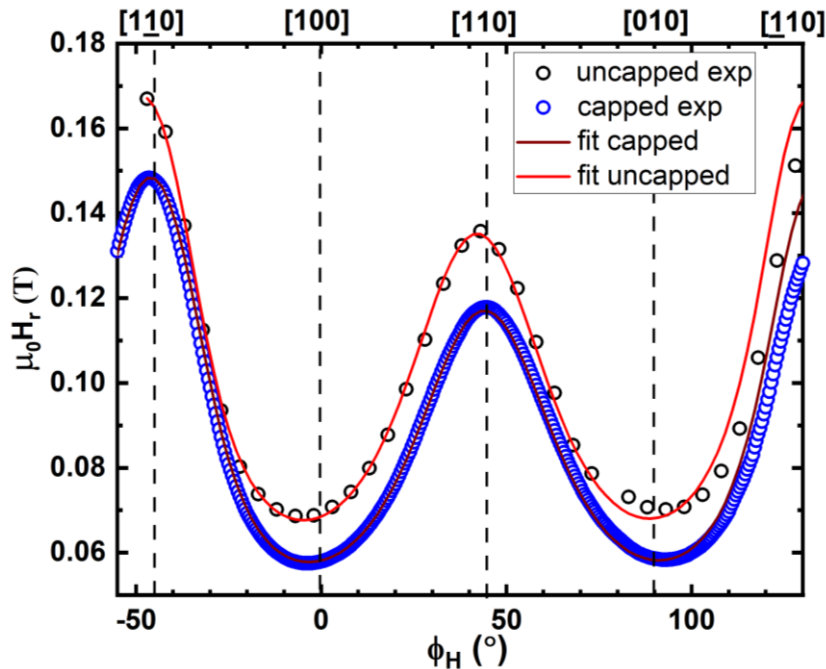


Figure 5.6 Azimuthal angular dependence of the resonance field of uncapped 5 nm Fe/GaAs (100) measured *in situ* and capped film Pt/Ag/Fe/GaAs (100) measured *ex situ* at a microwave frequency of 13 ± 0.02 GHz. The solid lines are the fits to the experimental data (open circles) using equation 2.18. The error bar of the resonance field data points is smaller than the symbol size.

The small in-plane uniaxial anisotropy $K_{2\parallel}$ of the Fe film grown on GaAs (100) results from the tensile strain produced at the Fe/GaAs interface (in-plane compression and

expansion in the perpendicular direction). This strain at the interface originates from the surface reconstruction of GaAs [93] and compressive strain after Fe deposition due to lattice mismatch between Fe and GaAs [22]. The vertical lattice parameter below 20 ML is approximately 3% larger than the bulk value [90]. This in-plane uniaxial strain from the interface is strong enough to sustain in-plane uniaxial anisotropy in 5 nm Fe film after capping with 2 nm Ag. Hence, $K_{2\parallel}$ remains unchanged after the capping layer (Table 5-1).

The cubic anisotropy $K_{4\parallel}$ is decreased by about ~10% after Ag and Pt deposition. The cubic anisotropy results mainly from the volume contribution due to Fe's four-fold cubic symmetry in thicker film [31]. However, for thin films below 2-3 nm, the surface-interface contribution dominates [16]. The slight decrease in cubic anisotropy after capping is from the volume contribution due to the change of density of states of Fe [94] at the Fe/Ag interface.

In contrast to the small change of the cubic and in-plane uniaxial anisotropy, there is a significant change of the out-of-plane uniaxial anisotropy $K_{2\perp}$ after Ag and Pt capping. The perpendicular anisotropy also contains volume and surface-interface contributions. The change of $K_{2\perp}$ is coming mainly from surface contribution due to change at Fe/vacuum interface. The uniaxial interface perpendicular anisotropy strongly depends on the composition of the interfaces. The most substantial anisotropy was observed for the Fe (001)/vacuum interface ($9.6 \times 10^{-4} \text{ J/m}^2$), followed by the Fe-Ag interface ($8.1 \times 10^{-4} \text{ J/m}^2$) and by the Fe-Au interface ($4.7 \times 10^{-4} \text{ J/m}^2$), all at RT [95]. The uniaxial perpendicular anisotropy in BCC Fe is an intrinsic effect caused by broken symmetry at the Fe/vacuum interface and not by growth peculiarities [96]. Fe-GaAs surface-interface and volume contributions do not play a significant role here, since the in-plane lattice parameter is close to the bulk value (section 5.1). The uniaxial character of the anisotropy due to the volume and Fe/GaAs interface will be more dominant for thinner Fe films. The change of the surface contribution to $K_{2\perp}$ can be also the result of a change in the surface roughness. The roughness creates an in-plane demagnetizing field at the edges of terraces, thereby reducing the shape anisotropy. Bruno et al. [97] calculated the dependence of the surface anisotropy K_s on the roughness parameter σ and the lateral correlation length ξ :

$$K_s = E_{shape} \frac{3}{4} \sigma \left[1 - f \left(2\pi \frac{\sigma}{\xi} \right) \right] \quad (5.3)$$

where $E_{shape} = \frac{1}{2} \mu_0 M^2$ is the shape anisotropy and the function $f \left(2\pi \frac{\sigma}{\xi} \right)$ becomes 1 when $\frac{\sigma}{\xi}$ tends to 0 for a very smooth surface, and 0.1 for a surface with a roughness parameter being of the order of the lateral correlation length. In our case, the total perpendicular anisotropy is reduced by about 78% ($\Delta K_{2\perp} = 2.1 \times 10^5 \text{ J/m}^3$), indicating the smoothening of the Fe film surface after capping. Thus, both mentioned effects lead to a change of the electronic structure of Fe (100) at the Fe/Ag interface which in turn changes the magnetocrystalline anisotropy.

The capping of the Fe film only with Ag leads to the oxidation of the sample [98] (aging effect), which causes a significant change in magnetic properties. Therefore, the sample was capped with 3 nm of Pt to protect the film against oxidation. Fe/Ag/Pt can be grown with separate layers and sharp interfaces between them [99] at room temperature. Since Pt growth on Ag (100) surface is not epitaxial, it does not affect the magnetic anisotropy of Fe/Ag heterostructure. However, spin transfer from Fe to the Ag or Pt layer is possible due to magnetization precession. This will be discussed in section 5.4 where linewidth dependence on frequency has been analyzed to determine damping contributions.

Sample	$K_{2\parallel} (\mathbf{10^4 J/m^3})$	$K_{2\perp} (\mathbf{10^5 J/m^3})$	$K_{4\parallel} (\mathbf{10^4 J/m^3})$
(5) Fe/GaAs	1.32 ± 0.05	2.73 ± 0.07	3.46 ± 0.03
(3) Pt/(2) Ag/(5) Fe/GaAs	1.25 ± 0.03	0.58 ± 0.08	3.07 ± 0.04

Table 5-1 Room temperature magnetic anisotropy constants of 5 nm Fe film grown on GaAs (100) before and after capping. The integers in the first column denote the thickness of the layer in nm.

5.3 Frequency-dependent FMR measurements and g-factor

The spectroscopic splitting factor ‘g’, or g-factor, measures the energy splitting of a degenerate state in a magnetic field H . It gives the sign and magnitude of the precession of the magnetic moment around the direction of the external magnetic field [37]. As described in sections 2.2 and 2.3, the g-factor comprises the information on the orbital and spin moment contribution (equation 2.15) to the total magnetic moment and can be determined using frequency-dependent FMR measurements. The orbital contribution to the total magnetic moment in a perfect cubic symmetry is quenched, giving the spin only value ($g = 2.0023$). Spin-orbit coupling leads to a deviation of the g-factor from 2.0023 in 3d metals, for example, BCC Fe $g = 2.09$, HCP Co $g = 2.18$, and FCC Ni $g = 2.18$ [100]. To determine the g-factor, a frequency-dependent resonance field along with the anisotropy data from angular-dependent measurement should be analyzed. Therefore, resonance has been measured at several frequencies of both the uncapped and capped sample in the film plane.

Figure 5.7 shows the frequency-dependent FMR of uncapped 5 nm Fe film grown on GaAs (100) measured *in situ* with a magnetic field applied parallel to $[1\bar{1}0]$ direction in the film plane. The greyscale represents the normalized amplitude of the microwave absorption, proportional to $\partial\chi''/\partial B$. The non-aligned mode of resonance is observed at the low-frequency region (< 9.5 GHz) along the hard axis. These signals (unsaturated mode) arise when the magnetization is not parallel to the external magnetic field but still, the resonance condition is fulfilled. These modes disappear at the higher field when the magnetization is perfectly aligned to the hard axis $[1\bar{1}0]$ direction. Frequency-dependent FMR measures the collective response of the spin system in which spin precession around the internal anisotropy field is included. The occurrence of unsaturated resonance modes yields a possibility to increase the accuracy of the measurements, as two or even three modes can be used for fitting. However, the analysis of the saturated resonance field is sufficient to extract all the information about anisotropy, g-factor, and damping parameters.

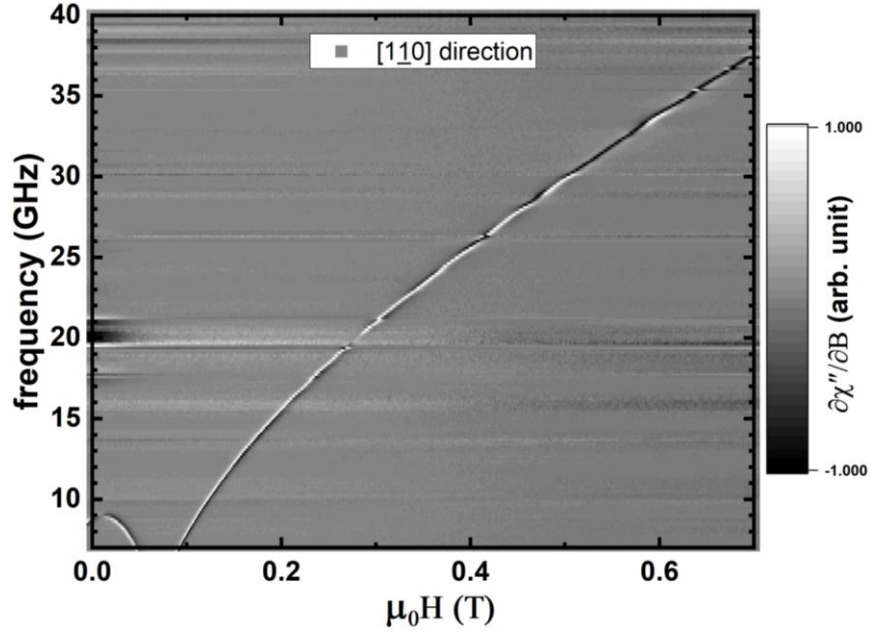


Figure 5.7 Frequency-dependent FMR of uncapped Fe/GaAs (100) measured *in situ* with the magnetic field applied parallel to [110] direction in the film plane. The greyscale represents the normalized amplitude of the microwave absorption derivative proportional to $\partial\chi''/\partial B$.

The FMR lines from these measurements were fitted with the derivative of complex Lorentzian function described by equation 5.2 to extract the amplitude, resonance field H_r , and linewidth ΔH_{FWHM} . The frequency-dependent resonance field plot can be fitted using the dispersion relation (equations 2.20 and 2.21) for different directions of the applied magnetic field. The resonance condition in a tetragonal symmetry for different angles of M and H has been described by M. Farle [37]. Figure 5.8 and Figure 5.9 show the square of frequency versus resonance field plot and its fitting according to the equations (2.20) and (2.21). The g-factor for three different crystallographic directions determined from fitting are listed in Table 5-2. In case of the capped Fe sample, the g-factor is very close to the Fe-bulk value ($g = 2.09$), whereas there is an increase of the g-factor for the uncapped film. In case of [100] easy direction, the increase of g-factor value with respect to bulk reaches ~4%, which indicates an increased orbital moment. As described by equation 2.15, the g-factor is determined by the ratio of orbital to spin moment. This results in a ratio of $\mu_l/\mu_s = 0.085 \pm 0.01$ for the uncapped sample in [100] direction which reflects the enhancement of orbital moment by ~100% ($\mu_l/\mu_s = 0.043$ for bulk Fe [101]). The spin and orbital moments of Fe film grown in GaAs (100) at ultrathin limit have been investigated by several groups using

XMCD [102-105]. However, the measurements were performed on Fe films with metal capping layers, e.g., Au or Cr. It has been shown by S. Tacchi et al. [106] that the Au capping layer on top of Fe film leads to a significant reduction of in-plane uniaxial magnetic anisotropy. In case of 7 ML Fe film, the uniaxial anisotropy is completely suppressed whereas in 20 ML film it is reduced to a half value.

Although there is an enhancement of orbital moment by 300% in 8 ML Fe film due to increased localization of electronic states at Fe/GaAs interface [104], the spin moment remains bulk-like [102]. For Fe bulk, the orbital moment is $\mu_l = 0.085 \mu_B$ and spin moment is $\mu_s = 1.98 \mu_B$ giving g-factor of 2.09. We have obtained the g-factor values in close agreement to previous studies. In our case the uncapped Fe film of thickness ~35 ML gives g-factor of 2.17 in the easy direction (~4% increase from bulk value) indicating enhanced orbital moment contribution due to reduced symmetry at the surface and interface. The first principle calculation predicted an enhancement of orbital moment at the surface of BCC Fe[107]. The surface states which are not completely quenched are responsible for the enhancement of surface magnetism. In the case of intermediate [110] and hard [110] direction, the increase in g-factor is $\leq 1.4\%$ for the uncapped sample. Anisotropic behavior of the g-factor in the film plane was shown [37], which can arise due to the anisotropic density of states at the Fe/GaAs interface [17]. The capped sample gives a g-factor value close to bulk Fe (2.09). Ag overlayer delocalizes the surface states of Fe which reduces the enhanced magnetic moment of Fe(100) surface [108]. These effects are directly related to the large atomic size of Ag (172 pm) compared to Fe (126 pm). Pt capping after Ag is not expected to affect the magnetic moment of Fe since it does not have any direct bond with Fe, and the Ag layer with 2 nm thickness equivalent to ~10 ML does not bear any magnetic moment.

Therefore, we conclude that the anisotropic enhancement of the g-factor of the uncapped Fe film is due to the strong spin-orbit coupling effect at the Fe/GaAs interface and the increased orbital moment contribution at the Fe surface. The Ag capping layer significantly suppresses the surface states and leads to a bulk-like g-factor. The role of the Ag overlayer is to delocalize the Fe surface states leading to increased surface magnetization [108].

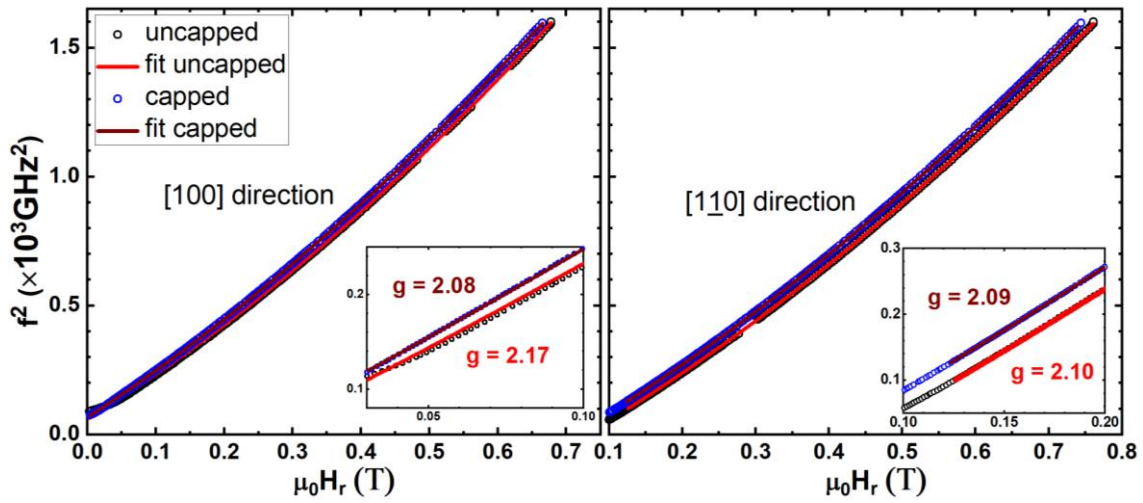


Figure 5.8 The square of microwave frequency versus the resonance field in the easy and hard direction of uncapped and capped 5 nm Fe/GaAs (100). The error bar for all the data points is smaller than the symbol size. The solid lines are the fit to the data according to the equations (2.20) and (2.21).

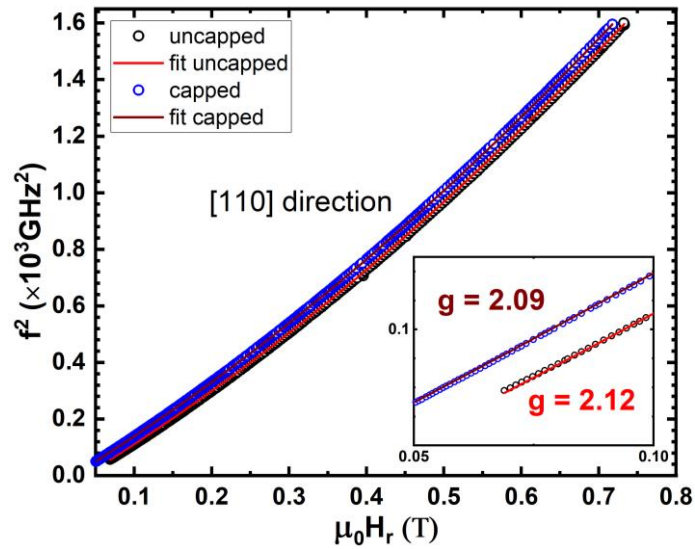


Figure 5.9 The square of microwave frequency versus the resonance field in the intermediate direction of uncapped and capped 5 nm Fe/GaAs (100). The error bar of data points is smaller than the symbol size. The solid lines are the fit to the data according to equations (2.20) and (2.21).

g-factor	[100]	[110]	[<u>110</u>]
(5)Fe/GaAs (100)	2.168 ± 0.010	2.117 ± 0.002	2.103 ± 0.001
(3)Pt/(2)Ag/(5)Fe/GaAs (100)	2.076 ± 0.001	2.093 ± 0.001	2.092 ± 0.001

Table 5-2 Spectroscopic splitting g-factor of 5 nm Fe/GaAs (100) before and after capping, measured in three different crystallographic directions. The integers in brackets denote the thickness of the layer in nm.

5.4 Effect of capping layer on relaxation mechanism (Gilbert damping)

The FMR linewidth allows to determine the magnetic relaxation parameters, e.g., Gilbert damping ' α ', spin pumping, and two-magnon scattering. The linewidth of the uncapped and capped Fe film is strongly angular-dependent in the film plane with four-fold and two-fold components, as shown in Figure 5.10. The anisotropic linewidth is typical for Fe/GaAs (100) coming from the in-plane uniaxial symmetry superimposed on four-fold symmetry. The increased linewidth of the capped film compared to the uncapped film is due to a change in Fe surface states. The linewidth in accordance with the LLG equation is related to the relaxation time τ as [109]

$$\Delta H = \frac{2}{\gamma\tau} \tag{5.4}$$

Therefore, the increased linewidth due to Gilbert damping indicates a decrease in surface relaxation time and g-factor. This is inline with the g-factor reduction after capping explained in section 5.3 (see Table 5-2). The crystal defects within the film or non-uniformities also play a significant role in ferromagnetic resonance absorption and its linewidth. In our case, since Fe and Ag film is epitaxially grown on GaAs substrate, the linewidth is smaller for an uncapped sample, while after capping with Pt which is not a single crystal, it increases considerably.

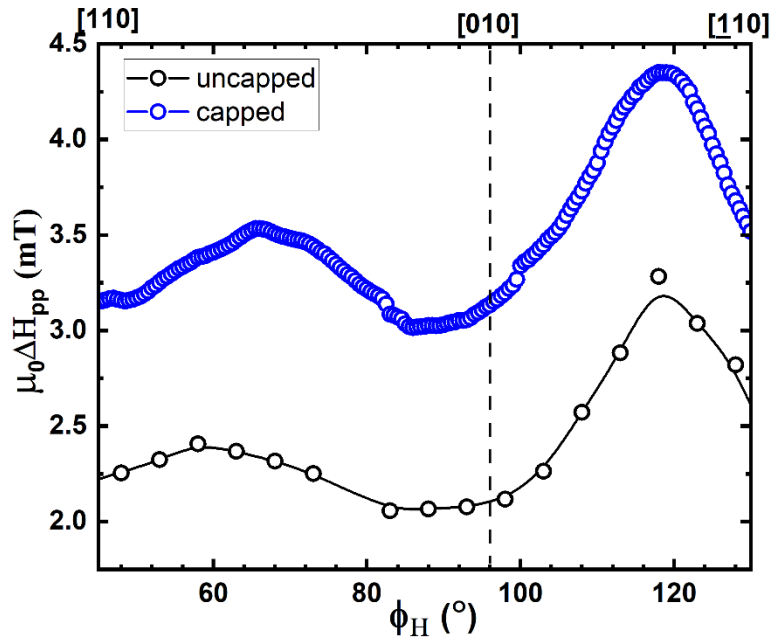


Figure 5.10 Angular dependent peak-to-peak linewidth of uncapped 5 nm Fe/GaAs (100) measured *in situ* and capped Pt/Ag/Fe sample measured *ex situ* at a microwave frequency of 12 GHz. The error bar for each data point is smaller than the symbol size.

The linear dependence of linewidth on the frequency provides the intrinsic damping parameter α (section 2.4.1). It is to be noted that the linear behavior of FMR linewidth with the frequency is only valid when the external magnetic field is parallel to the magnetization. However, at a lower magnetic field, the so-called dragging effect contributes to non-linearities in the frequency dependence of the linewidth. Figure 5.11 (a), (b), and Figure 5.12 show the frequency dependence of the linewidth of uncapped and capped 5 nm Fe film measured at three different crystallographic orientations and a linear fit in the higher frequency region. The increase of the linewidth at low frequencies observed for [100] direction is caused by the dragging effect, while for [110] direction it is due to the non-aligned ferromagnetic resonance mode [17]. The magnetization direction in a weak external field (at low frequency) is primarily determined by the anisotropy fields, while for the higher magnetic field the magnetization tends to align with the external field.

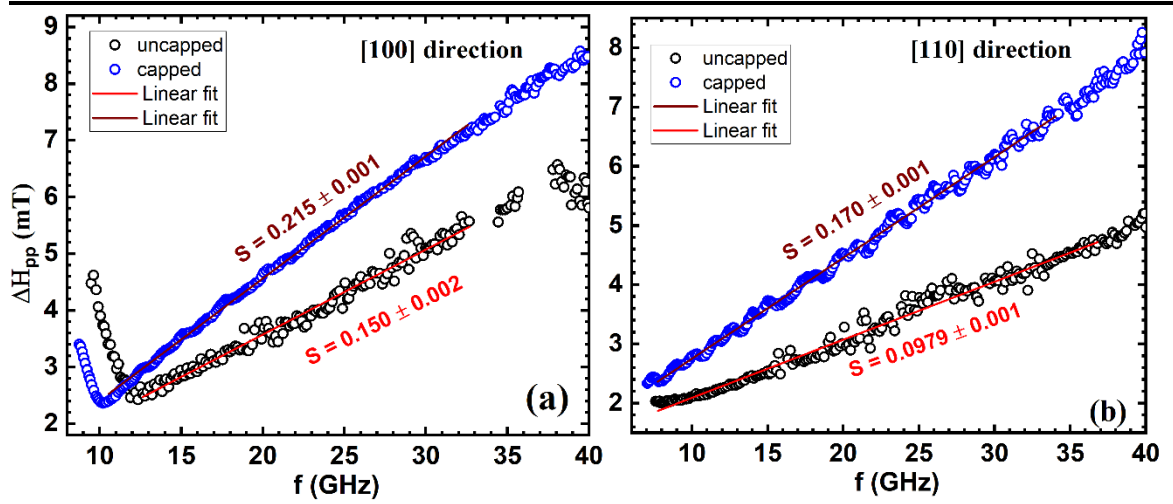


Figure 5.11 Frequency-dependent peak-to-peak linewidth of uncapped and capped 5 nm Fe/GaAs (100) in (a) the easy [100] and (b) intermediate [110] direction.

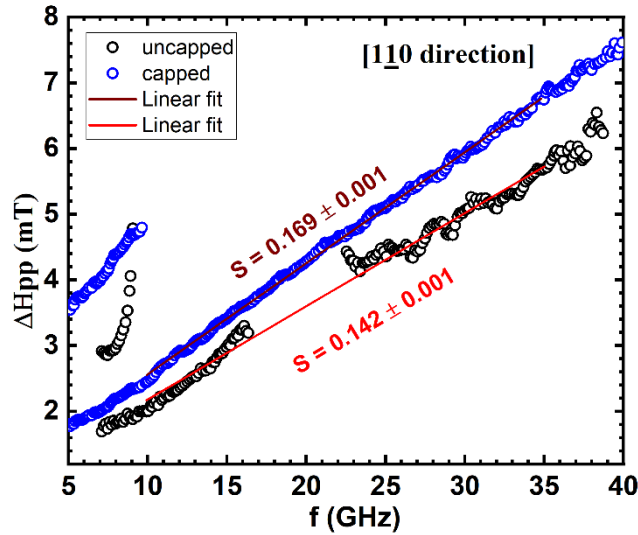


Figure 5.12 Frequency-dependent peak-to-peak linewidth of uncapped and capped 5 nm Fe/GaAs (100) in the hard [110] direction.

According to equation 2.24, the FMR linewidth is directly proportional to the microwave frequency and inversely proportional to the magnetization. Fitting the peak-to-peak linewidth versus frequency using equation 2.25 by taking the second term of right-hand side as slope gives Gilbert damping parameter α as:

$$\alpha = \frac{\sqrt{3}}{2} \frac{\gamma}{2\pi \times 10^9} * slope \quad (5.4)$$

where

$$\gamma = g \frac{\mu_B}{\hbar} \tag{5.5}$$

This indicates a directly proportional relation of Gilbert damping parameter α and linear slope of peak-to-peak linewidth versus frequency (ΔH_{pp} vs f) plot, i.e., bigger the slope is, the higher the α value will be. Using the g-factor determined from the frequency-dependent resonance field (Table 5-2) and slope from Figure 5.11 and Figure 5.12 (Table 5-3), α is calculated using equation 5.4 for the uncapped and capped sample in three different crystallographic directions tabulated in Table 5-5. The capped film has a larger Gilbert damping in comparison to the uncapped film. In the case of [100] direction, there is a 44% increase of α from uncapped to capped Fe film, while there is a 71% increase in the [110] direction. The increase in α indicates a decrease in relaxation time and an increase in spin-orbit interaction. α is governed by the spin-orbit interaction, which couple phonons to the spin-system, i.e., the stronger the spin-orbit interaction, the more energy is dissipated, thus damping the precession of the spins. The enhancement of Gilbert damping is due to Pt capping having high spin-orbit coupling. Since Ag has a large spin diffusion length of about 132-152 nm [1], the angular momentum of Fe can be pumped into the Pt layer causing spin current. The damping of ferromagnetic Fe is enhanced by spin pumping [110, 111], where pure spin currents are excited in the Fe layer and absorbed at the interface layer. Another reason for the increased magnitude of α could be the interface's electronic band effect. Garate et al. [112] proposed a simple model describing Gilbert damping parameter as $\alpha \sim n(E_F)\xi^2\tau^{-1}$ under certain conditions, where $n(E_F)$ is the density of states at Fermi level E_F , ξ is the strength of spin-orbit interaction, and τ is the electron momentum scattering time. Therefore, the change in the density of state at the Fe surface after capping it with Ag as well as Pt significantly affects the intrinsic damping. Along with this, the enhanced spin-orbit interaction after Pt capping increase α . Increase in α also indicates a decrease in electron scattering time after capping. The observed small anisotropy of the damping parameter α in Fe is also due to the anisotropic density of states $n(E_F)$ of the Fe film [17]. *Ab initio* calculations show that the interfacial spin-orbit interactions modify the electronic structure on varying the magnetization orientation, due to the anisotropy of the interfacial Fe d states [17]. We conclude that the electronic structure of Fe atoms at the Fe/vacuum and Fe/Ag interface plays a significant role in modifying the magnetic properties of thin Fe films.

Slope (mT/GHz)	[100]	[110]	[<u>110</u>]
5 nm Fe/GaAs (100)	0.150 ± 0.002	0.098 ± 0.001	0.142 ± 0.001
Pt/Ag/Fe/GaAs (100)	0.215 ± 0.001	0.170 ± 0.001	0.169 ± 0.001

Table 5-3 The slope of linear fit extracted from frequency-dependent linewidth of uncapped and capped 5 nm Fe film measured for three different crystallographic orientations.

ΔH_0 (mT)	[100]	[110]	[<u>110</u>]
5 nm Fe/GaAs (100)	0.574 ± 0.042	1.112 ± 0.022	0.763 ± 0.035
Pt/Ag/Fe/GaAs (100)	0.253 ± 0.014	1.045 ± 0.015	0.875 ± 0.008

Table 5-4 Inhomogeneous broadening ΔH_0 of uncapped and capped sample determined by the linear fit of frequency-dependent linewidth.

$\alpha (\times 10^{-3})$	[100]	[110]	[<u>110</u>]
5 nm Fe/GaAs (100)	3.94 ± 0.01	2.51 ± 0.002	3.56 ± 0.001
Pt/Ag/Fe/GaAs (100)	5.23 ± 0.001	4.31 ± 0.001	4.28 ± 0.001

Table 5-5 Gilbert damping parameter α of uncapped and capped sample in three different crystallographic directions.

5.5 Summary

In this chapter, an effect of Ag and Pt capping on the magnetic anisotropy, g-factor, and damping of 5 nm Fe film grown on GaAs (100) has been investigated using FMR. The

sample was grown, characterized, and capped *in situ* to prevent oxidation, which provided access to the genuine properties of a pure Fe film. The magnetocrystalline anisotropy is significantly changed after capping the Fe film with Ag and Pt mainly due to the suppression of the surface contribution to the perpendicular anisotropy. The capping layer has a negligible effect on the in-plane magnetic anisotropy (cubic and uniaxial). It was observed that the uncapped Fe film exhibit an enhanced g-factor (~4%) in comparison to bulk Fe while the capped film shows g-factor close to the bulk value. The enhancement of the g-factor is due to an increased orbital moment of Fe film at the surface. The anisotropy of g-factor in uncapped Fe film is observed which vanishes upon capping the film with Ag and Pt. Finally, the increase in Gilbert damping of Fe film is observed after capping it with Ag and Pt. This is attributed to the enhanced spin-orbit interaction and decrease in relaxation time after capping a ferromagnetic layer Fe with normal metal Ag and heavy metal Pt. All these effects are directly related to the electronic band structure of Fe atoms at the surface and interface. Therefore, we conclude that the change in electronic structure after capping significantly modifies the magnetic anisotropy (~78% in out-of-plane direction), g-factor (~4% in [100] easy direction), and damping contributions (~40-70%) of Fe films after capping.

6 Influence of substrate doping on the magnetic properties of Pt/Ag/Fe/GaAs (110) heterostructure

In this chapter, the experimental results of the magnetic and structural characterization of an epitaxial Pt/Ag/Fe/GaAs (110) heterostructure with different doping of the GaAs (110) substrate (undoped, p-doped, and n-doped) is studied using *ex situ* ferromagnetic resonance and *in situ* LEED and AES. Magnetic anisotropy, g-factor, and magnetic relaxation parameters were determined for three different samples with a substrate doping concentration of 10^7 cm^{-3} (undoped), 10^{19} cm^{-3} (Zn-doped), and 10^{18} cm^{-3} (Si-doped). It was found that the in-plane uniaxial magnetic anisotropy is significantly changed (10-30%) with different doping levels in GaAs. From frequency-dependent ferromagnetic measurements, an isotropic g-factor was found, and no dependence of g-factor on the type of substrate doping is observed. A single relaxation channel, i.e., intrinsic Gilbert damping, is identified by frequency-dependent resonance linewidth analysis. Along the easy direction, the Gilbert damping is decreased by ~20% in the p-doped sample compared to the undoped sample, while there is no change in the n-doped sample with respect to the undoped sample within the error bar.

6.1 Introduction

Prinz and Krebs et al. [113] in 1981 first reported the epitaxial growth of single-crystal BCC Fe on GaAs (110) with a lattice mismatch of 1.4%. They found the optimum growth of good quality 20 nm Fe film at a substrate temperature between 175 and 225°C. Higher substrate temperatures resulted in faceted growth with grooves along [110] direction. However, Höllinger et al. [15] have successfully grown epitaxial Fe film on GaAs (110) at room temperature in the thickness range of 4-64 ML. Both [15, 113] studies showed that the growth of Fe (110) starts with the formation of 3D islands and coalescence after a few monolayers. It has been reported that by depositing Fe at elevated temperatures (175-200°C), the GaAs (110) surface is disrupted, and an intermixed region is formed with Fe-As-Ga compounds at the interface [80, 114]. Films grown at lower substrate temperature have a better Fe/GaAs interface (less alloying); however, epitaxial quality is compromised.

Therefore to produce a good quality epitaxial Fe film without any interdiffusion at the interface, Winking et al. [115] introduced a two-step process, where Fe is grown at 130 K substrate temperature followed by annealing to room temperature. This process yielded 2D layer-by-layer growth with an abrupt nonreacted heterointerface. Grünebohm et al. [116] also predicted using DFT that Fe can be grown on GaAs (110) with an abrupt and non-intermixed interface at higher flux and low temperature.

The magnetic measurements on Fe/GaAs (110) show that these films exhibit a reorientation of the easy axis from the [001] to the [110] direction at room temperature between 24-50 ML [15]. This spin-reorientation transition is due to a transition from a perpendicular magnetic anisotropy (PMA) to an in-plane magnetic anisotropy (IPMA) with increasing thickness. DFT calculation on $\frac{1}{4}$ ML of Fe adatoms on a free GaAs (110) surface indicates no quenching of the magnetic moments [116]. Grünebohm et al. explain this with the fact that the (110) surface is stoichiometric which leads to a reduction of sp_2 hybridization. The DFT calculations were performed at 0 K, therefore, the interdiffusion effect will be enlarged at finite temperatures. Iffländer et al. [117] investigated the influence of the type of substrate doping on the Kerr signal in ultrathin Fe film grown on GaAs (110). He found no dependence of Kerr rotation on the type of doping (n-type, p-type, and intrinsic GaAs) in the thickness range of 2.5-2.7 ML Fe films. However, in his case, the films were grown at low temperatures using the method proposed by Winking [115]. It is important to know if the same independence of magnetic properties is valid for room-temperature-grown Fe films. Therefore, we have studied the influence of doping on the magnetic properties (anisotropy and damping) of Pt and Ag capped 5 nm Fe films grown on GaAs (110) at room temperature using FMR.

6.2 Sample growth and structural characterization

Three samples (Pt/Ag/Fe heterostructure) with different doping of the GaAs substrate, namely undoped, p-doped, and n-doped, were prepared with the same method described as follows. A commercial 4×4 mm² GaAs (110) substrate was pre-cleaned with absolute ethanol in an ultrasonic bath and pasted on the UHV sample holder with silver paste.

Initially, the substrate was sputtered at an energy of 1 keV (sample current $\sim 1 \mu\text{A}$) with argon partial pressure of 1×10^{-6} mbar. The sputtering with a perpendicular incidence of beam was carried out along with heating up to 960 K for 1 hour and then the sample was annealed at 960 K for half an hour. The characterizations performed during and after sample preparation is schematically shown in Figure 6.1. LEED images were taken on the clean GaAs (110) substrate at room temperature and pressure $\leq 7.0 \times 10^{-9}$ mbar. The prepared substrate yields a well-ordered $\{1 \times 1\}$ surface with no surface reconstruction as expected from (110) GaAs (Figure 6.2 a-c). The LEED image of three samples (Figure 6.2 a-c and d-f) were taken at different energies according to the best visible diffraction pattern for that sample. However, the LEED should not depend on the doping of the substrate. A 5 nm Fe film was grown on the prepared substrate using electron beam evaporation at room temperature with a deposition rate of $\sim 0.1 \text{ nm/min} \pm 10\%$. The pressure during deposition was maintained at $\leq 7.5 \times 10^{-10}$ mbar. The thickness of the film was monitored using a quartz thickness monitor. Subsequently, 3 nm Ag, and 4 nm Pt, were deposited on top of the Fe film at room temperature below 5×10^{-9} mbar inside the chamber. LEED images taken on the clean GaAs (110) substrate and 5 nm Fe film for all three samples are shown in Figure 6.2. After taking the AES spectra of the complete heterostructure (Pt/Ag/Fe/GaAs), the sample was taken out of the chamber. The FMR measurement was carried out *ex situ* using CPW setup as described in section 3.4.2. A similar procedure was followed for two more samples with different doping of the substrate. Room temperature was maintained during deposition as well as all the measurements.

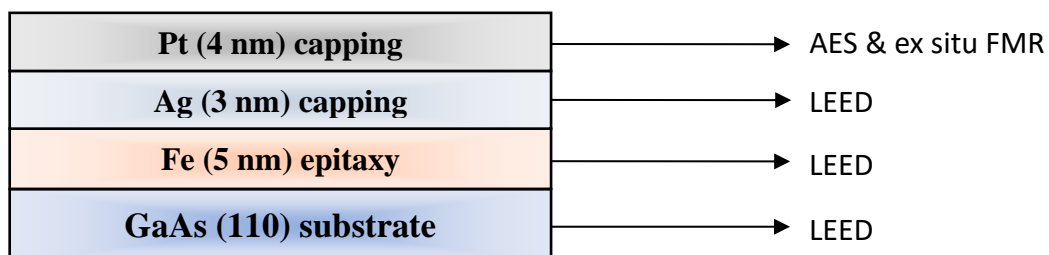


Figure 6.1 Schematic of prepared sample and characterization followed during sample preparation *in situ* and *ex situ*.

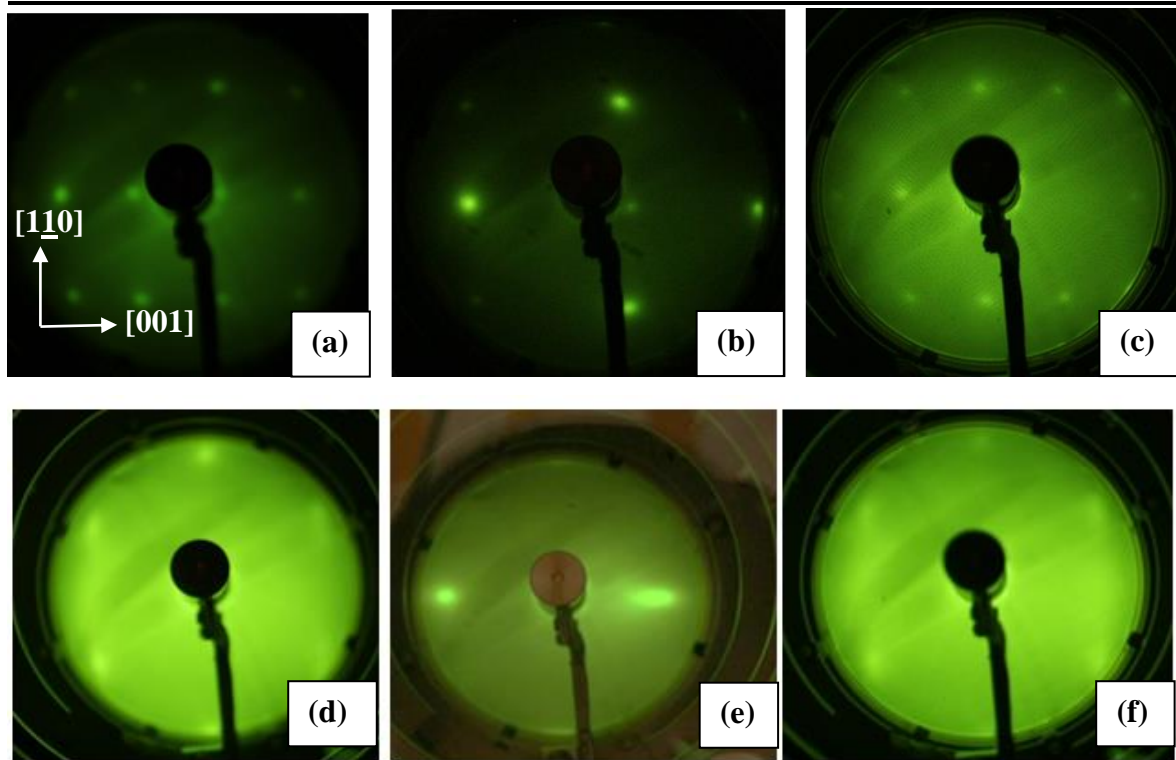


Figure 6.2 LEED images taken *in situ*: (a) GaAs (110) undoped at 97 eV, (b) GaAs (110) p-doped at 78 eV, (c) GaAs (110) n-doped at 130 eV, (d) 5 nm Fe/GaAs (110) undoped at 177 eV, (e) 5 nm Fe/GaAs (110) p-doped at 75 eV, (f) 5 nm Fe/GaAs (110) n-doped at 156 eV.

LEED images of clean GaAs (110) substrate (Figure 6.2 a-c) show a cubic (110) plane with an aspect ratio of 1.40 ± 0.05 for all three samples. This confirms the same substrate surface formation in all three samples with different doping. LEED images taken after film deposition are shown in Figure 6.2 (d-f) indicating an epitaxial growth of Fe on GaAs (110). The ratio between the diffraction spots along [001] and [110] is close to $\sqrt{2}$, typical for BCC Fe (110). The Fe film was capped with 3 nm of Ag and 4 nm of Pt immediately after the LEED measurement since it is already known from previous results (chapter 4) that Fe (110) films change magnetic properties after some hours of being in UHV at room temperature. AES was taken from the complete heterostructure sample as shown in Figure 6.3. The spectrum was recorded in an energy range of 30-700 eV; however, no peaks of Fe were seen in the whole scan. Since electrons (1 keV from electron gun) can penetrate up to ~ 5 nm in the film, only Pt and Ag peaks can be observed. This also confirms that the Fe film is fully covered with Ag and Pt layers. Furthermore, no carbon peak is observed indicating a contamination-free sample after deposition in high vacuum conditions.

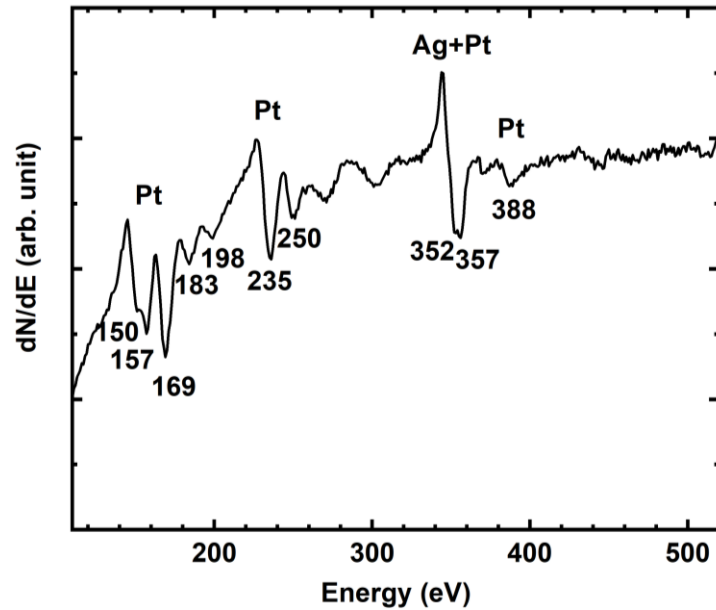


Figure 6.3 AES spectrum taken *in situ* after deposition of the complete sample Pt/Ag/Fe/GaAs (110) undoped.

6.3 Magnetic anisotropy of Pt/Ag/Fe/GaAs (110) heterostructure

FMR was measured *ex situ* with the external magnetic field $\mu_0 H$ applied parallel to the film plane. Angular-dependent FMR spectra were measured at an angle step of 1° and ~ 13 GHz. The modulation frequency, phase, and amplitude were set to 12.10 kHz, 320° and 2 mT, respectively. The time constant and conversion time on the lock-in amplifier was set to 40.96 ms and 81.92 ms, respectively. For angular-dependent measurement, the sample was rotated with respect to the magnet using a goniometer. Figure 6.4 shows the result of the complete 180° angular-dependent FMR measurement of Pt/Ag/Fe/GaAs (110) p-doped sample taken at 12.902 GHz frequency. The grey scale corresponds to the normalized amplitude of the microwave absorption derivative, proportional to $\partial\chi''/\partial B$. Similar results were obtained for the other two samples (undoped and n-doped). The angular dependence clearly shows the signal as expected for the (110) direction. The inset of Figure 6.4 shows the schematic of (110) surface plane with three crystallographic directions of the sample (red box). The absolute minima lie equivalently along $[001]$ and $[00\bar{1}]$ directions, so there is 180° symmetry. The absolute minimum here indicates the easy direction of magnetization without external field, which is independent of the position of the maxima, and the local minima

along [110] direction denote intermediate direction. The maxima seem to be a hard direction, but they are not. There is a slight shift from the maximum point ($\varphi = 54.7^\circ$ is hard axis) because of the diagonal angle in the (110) plane. The grey scale plot clearly shows a single resonance line throughout all directions indicating good quality epitaxial Fe growth and no intermixing of capping layer with uniform Fe film. Each individual FMR spectrum was fitted separately using complex Lorentz function (equation 5.2) to determine the resonance field and linewidth.

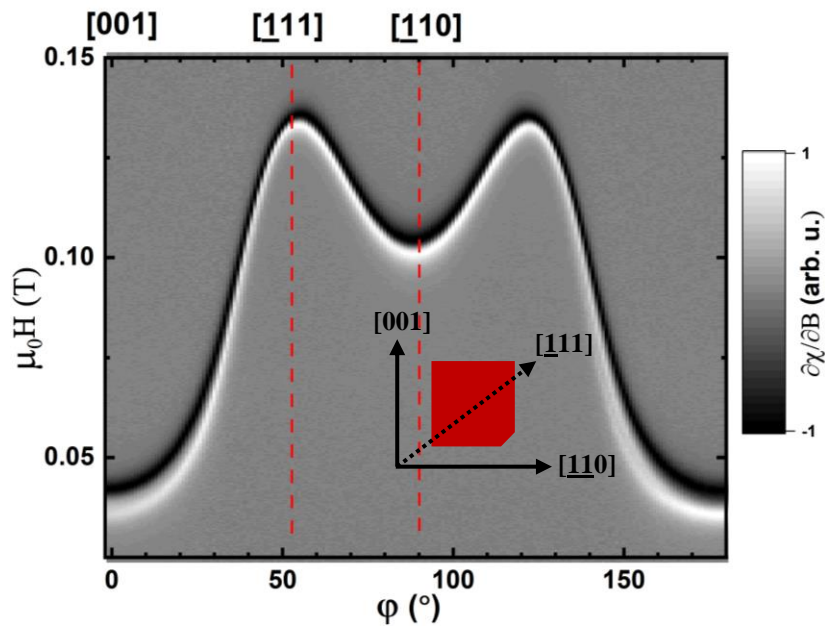


Figure 6.4 In-plane angular-dependent *ex situ* FMR measurement of 4 nm Pt/3 nm Ag/5 nm Fe/GaAs (110) p-doped sample taken at 12.902 GHz and room temperature. The grey scale corresponds to the normalized FMR amplitude. Inset gives a schematic representation of crystallographic directions of the (110) surface.

Figure 6.5 shows the normalized FMR spectra (open circles) and complex Lorentzian fit using equation 5.2 (solid lines) for undoped, n-doped, and p-doped sample in three different crystallographic directions. In order to describe a complex resonance curve with both absorption and dispersion part, complex Lorentz function with phase factor is appropriate. The role of eddy currents in these films is insignificant due to lower thickness of Fe films. The eddy currents are produced in ferromagnetic materials during resonance measurement by the microwave fields and it strongly depends on the skin depth δ . The skin

depth is the depth from the surface of conductor at which the microwave amplitude is decayed to 1/e of its original value.

$$\delta = \sqrt{\frac{2}{\omega\sigma\mu_r\mu_0}}$$

(6.1)

where σ is the electrical conductivity and $\mu_r = 1 + \chi$ is the relative permeability. For typical transition metals, δ is in the range of one micron if excited with 10 GHz. With increasing microwave frequency, the skin depth decreases as seen from equation 6.1. Also, it depends on the susceptibility of the ferromagnets which further increases during FMR experiments. This in turn lowers the skin depth in our case.

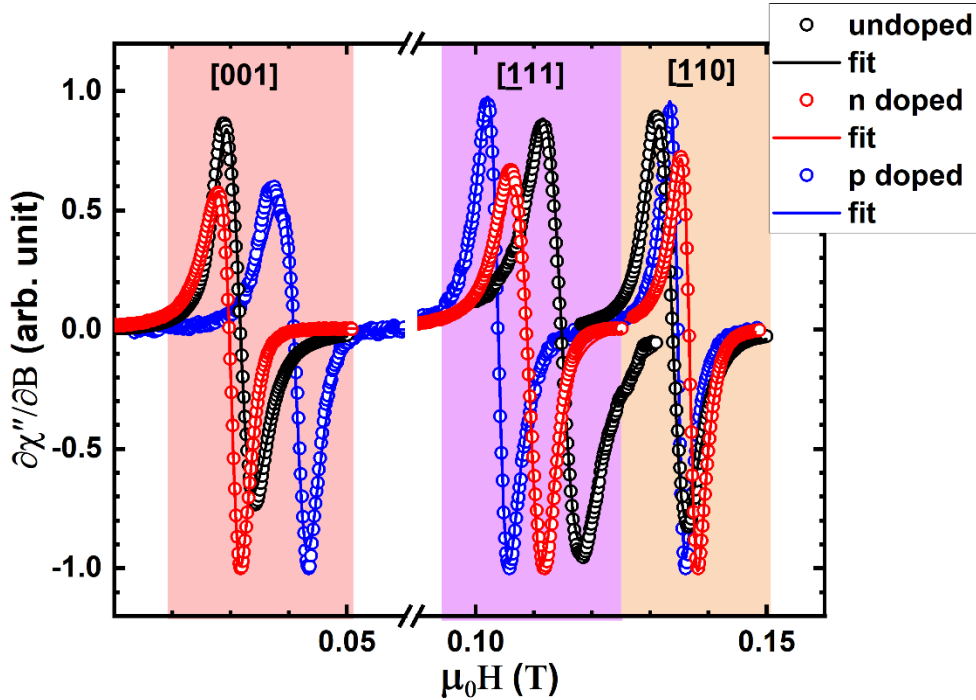


Figure 6.5 FMR spectra of Pt/Ag/Fe/GaAs (110) undoped, n-doped, and p-doped sample in three different crystallographic directions. The solid line represents complex Lorentzian fit to the experimental data.

Figure 6.6 shows the angular-dependent resonance field curve for undoped, n-doped, and p-doped samples and their fit (solid lines) using the energy density described by equation 2.19. The fitting was performed assuming a constant magnetization $M = 1600 \text{ kA/m}$ and

g-factor $g = 2.09$. Frequency used during measurement was inserted in the fitting program i.e., 13.086, 12.937, and 12.903 GHz for undoped, n-doped, and p-doped samples, respectively. The angle between uniaxial in-plane and cubic direction was set to $\delta = 90^\circ$. The anisotropy parameters determined from the fitting are given in Table 6-1.

It has been discussed that a spin reorientation takes place in Fe films grown in GaAs (110) in the ultrathin limit. The critical thickness at which the transition of easy axis from [110] to [001] direction occurs is dependent on the sample preparation, especially the growth temperature [15]. In our case, the easy axis lies at [001] in-plane direction, indicating that the film thickness is above the critical thickness for transition. This behavior explains the existence of two competing anisotropy energies in the film which favors alignment of magnetization along different crystal axes. Therefore, the energy density equation used to fit angular dependent resonance data includes the superposition of in-plane cubic and uniaxial anisotropies.

Sample	$K_{2\parallel} (\times 10^4 J/m^3)$	$K_{2\perp} (\times 10^5 J/m^3)$	$K_{4\parallel} (\times 10^4 J/m^3)$
undoped	2.41 ± 0.03	1.43 ± 0.10	3.47 ± 0.04
p-doped	1.58 ± 0.03	1.50 ± 0.05	3.25 ± 0.03
n-doped	2.15 ± 0.04	1.31 ± 0.1	3.49 ± 0.07

Table 6-1 Room temperature anisotropy parameters of Pt/Ag/Fe/GaAs (110) undoped, p-doped, and n-doped samples determined by fitting angular dependent resonance field using equation 2.19.

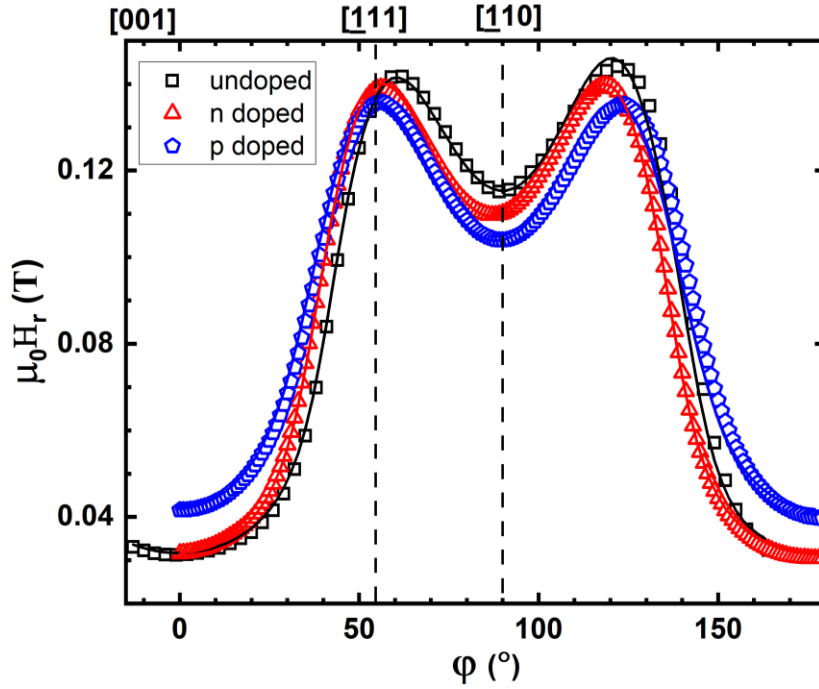


Figure 6.6 Angular-dependent resonance field of Pt/Ag/Fe/GaAs (110) undoped, n-doped, and p-doped sample. The solid line shows the best fit to the data according to equation 2.19 yielding anisotropy parameters tabulated in Table 6-1.

We have obtained a significant change in the in-plane uniaxial anisotropy $K_{2\parallel}$ with doping the substrate (see Table 6-1). The magnetocrystalline anisotropy mainly arises from spin-orbit interaction that couples the magnetic moment of the electron to the crystal lattice [37]. Therefore, the shift of uniaxial anisotropy can be either due to a change in crystal structure or spin moment. Theoretical studies have shown that doping can effectively modulate magnetic anisotropy [118]. DFT calculations reveal that the chemical potential shift associated with the doping is responsible for the reduced magnetic anisotropy by decreasing the energy gain from the spin-orbit induced band splitting [118]. In our case, the interface-driven spin-orbit coupling in Fe film will be modified by the electron or hole doping in GaAs, altering the electronic structure (bands) of Fe at the Fe/GaAs interface and resulting in the change of magnetic anisotropy in three samples. However, theoretical calculations are needed to verify this scenario. The change in cubic anisotropy $K_{4\parallel}$ and out-of-plane anisotropy $K_{2\perp}$ is negligible within the error bar. This is because the crystal structure of Fe film in all three samples is the same. We have confirmed this also with LEED measurements where the ratio of lattice length remains the same for all three samples.

6.4 Magnetic relaxation (Gilbert damping)

Now we turn to frequency-dependent measurement results. Figure 6.7 shows the frequency-dependent resonance field for all three samples with the magnetic field applied parallel to [001], [$\bar{1}$ 11], and [110] directions in the film plane. The measurements were performed *ex situ* in the range of 1-40 GHz at room temperature. Fitting the resonance curve using dispersion relation equations (2.20) and (2.21) reveals an isotropic g-factor of 2.08 ± 0.05 for all three samples. This indicates the same spin to orbital moment ratio $\mu_l/\mu_s = 0.04$ for all samples. As already discussed in section 5.3, the capping layer suppresses the surface states of the Fe film, and this leads to the bulk-like g-factor.

To determine the magnetic relaxation, FMR linewidth as a function of frequency has been analyzed. Figure 6.8 shows the frequency-dependent linewidth of all three samples in [001], [$\bar{1}$ 11], and [110] directions. The solid lines are linear fits to the data. The peak-to-peak linewidth versus frequency curve in the complete frequency range (1-40 GHz) gives linear behavior described by intrinsic or viscous damping and inhomogeneous broadening. The non-linearities are also present at the lower magnetic field due to the dragging effect where the magnetization angle varies with the applied field. The Gilbert damping term leading to a frequency-dependent peak-to-peak linewidth can be described by equation 2.25. ΔH_0 (inhomogeneous broadening) can arise from sample imperfection such as mosaicity and defects. In our case, the hole or electron doping can significantly affect the inhomogeneity present in the sample leading to different ΔH_0 in different samples. Table 6-3 gives the value of ΔH_0 calculated from linear fit of frequency-dependent linewidth (Figure 6.8). It has been found that the inhomogeneous linewidth broadening can be angular-dependent or anisotropic in ferromagnetic thin films [119, 120]. The reason for that is explained by angular dispersion of the induced uniaxial magnetic anisotropy.

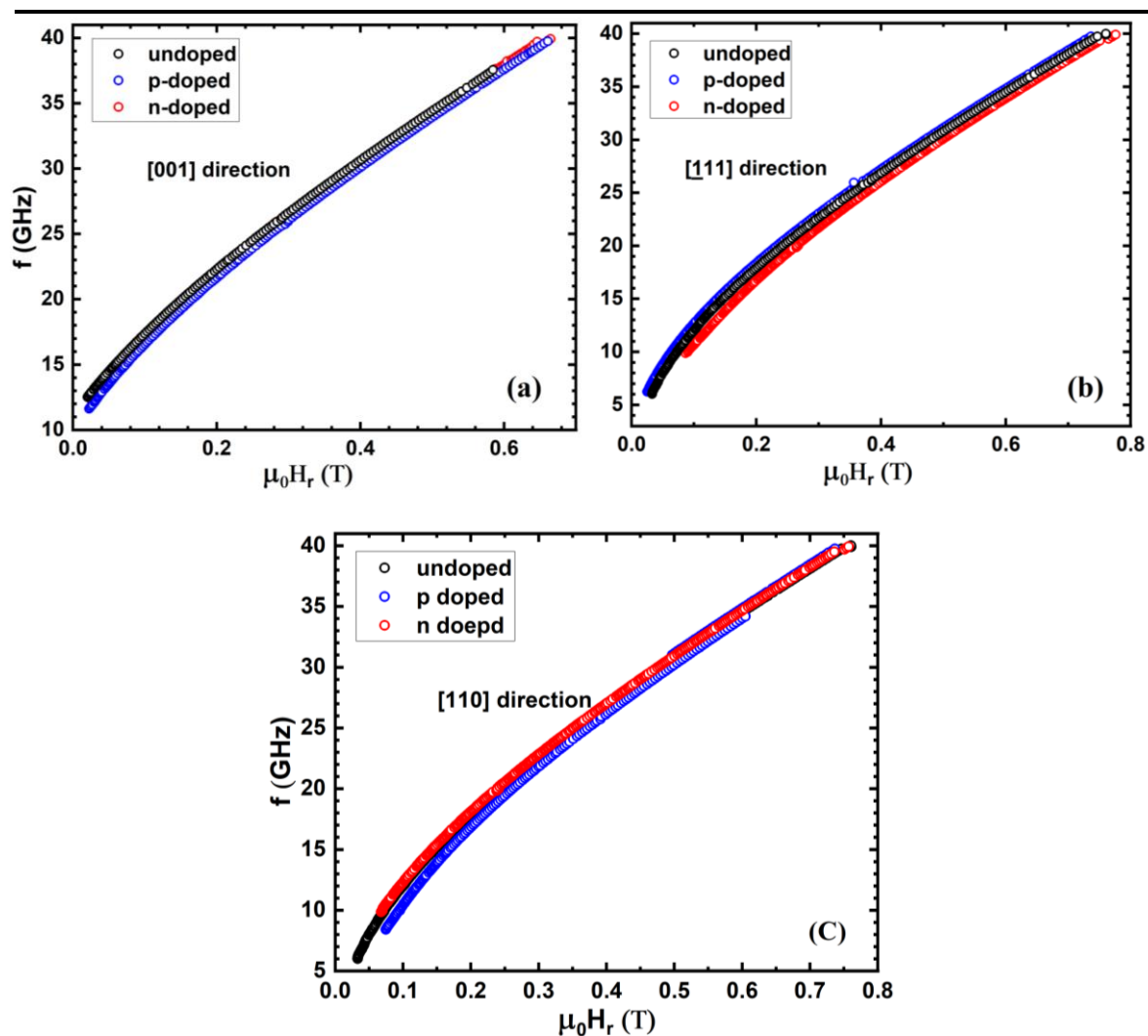


Figure 6.7 Frequency-dependent resonance field of Pt(4 nm)/Ag(3 nm)/Fe(5 nm) heterostructure grown on undoped, p-doped, and n-doped GaAs (110) substrate measured in-plane in (a) [001] easy, (b) $[1\bar{1}1]$ hard, and (c) [110] intermediate direction. The error bar for all data points is smaller than the symbol size.

Slope (mT/GHz)	[001]	$[1\bar{1}1]$	[110]
undoped	0.153 ± 0.001	0.080 ± 0.001	0.150 ± 0.002
p-doped	0.123 ± 0.002	0.135 ± 0.001	0.136 ± 0.001
n-doped	0.149 ± 0.001	0.1534 ± 0.0002	0.155 ± 0.001

Table 6-2 The slope of the linear fit of the frequency-dependent linewidth of Pt/Ag/Fe/GaAs (110) undoped, n-doped, and p-doped samples measured for three different crystallographic orientations (Figure 6.8).

ΔH_0 (mT)	[001]	[111]	[110]
undoped	1.563 ± 0.001	4.4 ± 0.03	4.421 ± 0.059
p-doped	2.070 ± 0.065	0.7 ± 0.02	0.701 ± 0.034
n-doped	1.328 ± 0.026	0.5 ± 0.007	2.284 ± 0.036

Table 6-3 Inhomogeneous broadening ΔH_0 of Pt/Ag/Fe/GaAs (110) undoped, n-doped, and p-doped samples determined by the linear fit of frequency-dependent linewidth.

The Gilbert damping parameter α calculated from a linear fit of frequency-dependent linewidth using equation 5.4 is tabulated in Table 6-4. The anisotropic damping behavior in our samples is also correlated with the in-plane uniaxial anisotropy field and the density of states [17, 18]. The obtained α values for capped Fe films is close to bulk Gilbert damping for Fe film $\alpha_{bulk} = (3.7 \pm 0.2) \times 10^{-3}$. The doping of the substrate has no direct relationship with the Gilbert damping parameter of the Fe film. However, it is known from Kambersky [50, 51] that the Gilbert damping in metals due to spin-orbit coupling is dependent on interband and intraband scattering mechanisms. For the interband scattering mechanism, magnetization dynamics can excite electron-hole pairs across different bands resulting in resistivity-like Gilbert damping. Its magnitude scales with the inverse of electron momentum scattering time τ_e , i.e., increased electronic scattering results in higher damping [121]. On the contrary, the intraband scattering mechanism is understood through the breathing Fermi surface model [122], where electron-hole pairs are excited in the same band, yielding conductivity-like Gilbert damping. It scales directly with τ_e ; i.e., reduced electronic scattering results in higher damping. All these effects at the Fe/GaAs interface due to different doping concentrations in GaAs can modify the Gilbert damping of the whole sample. Although this mechanism can explain the effect, detailed measurements and modelling is required to exactly find the origin of the observed change due to substrate doping.

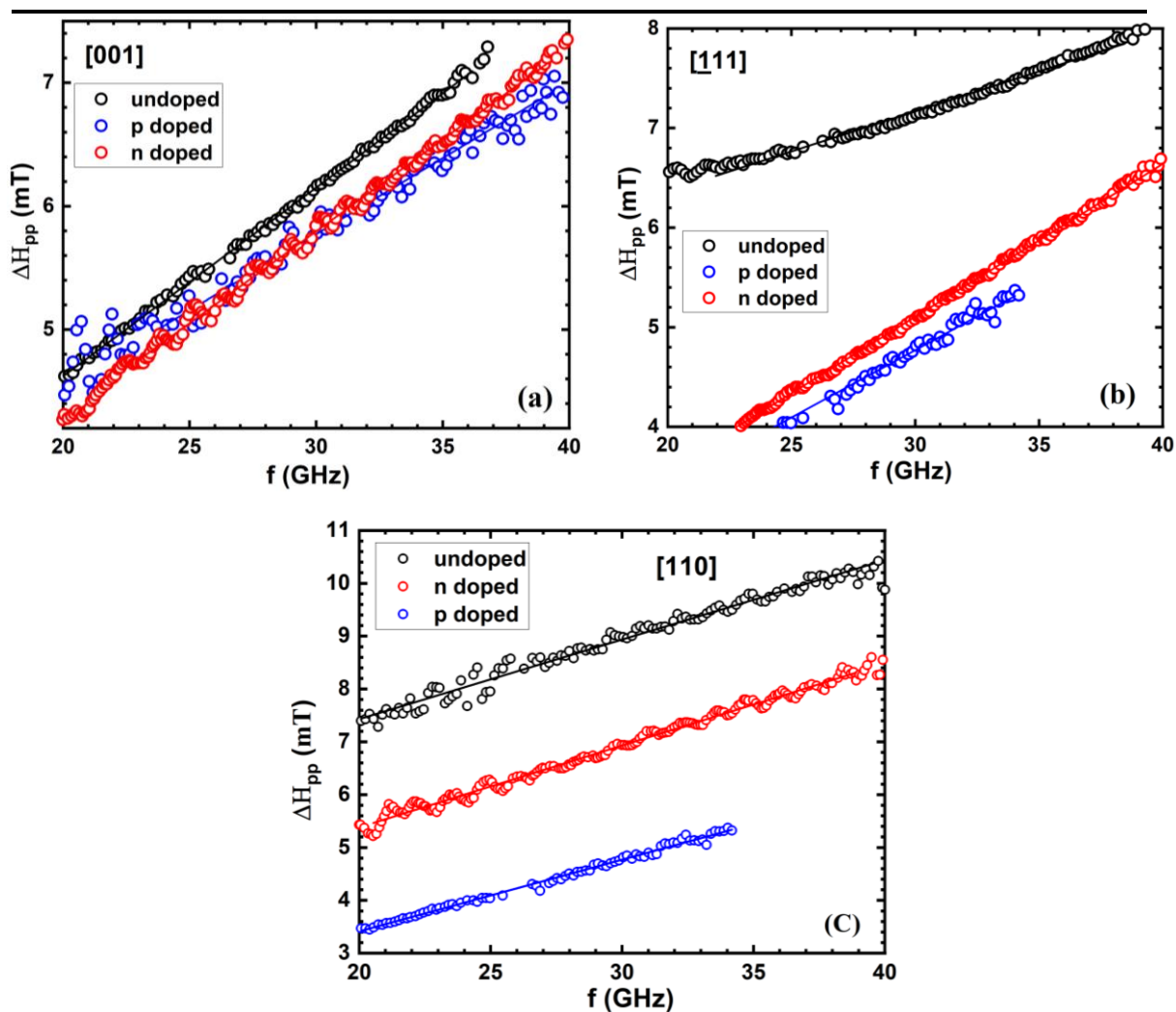


Figure 6.8 Frequency-dependent peak-to-peak linewidth (open circles) and its linear fit (solid line) of Fe/GaAs (110) undoped, p-doped, and n-doped sample in (a) [001] direction, (b) [111] direction, and (c) [110] direction.

$\alpha (\times 10^{-3})$	[001]	[111]	[110]
undoped	3.86 ± 0.05	2.02 ± 0.05	3.78 ± 0.05
p-doped	3.10 ± 0.05	3.40 ± 0.05	3.43 ± 0.05
n-doped	3.76 ± 0.05	3.87 ± 0.05	3.90 ± 0.05

Table 6-4 Gilbert damping parameter of Pt/Ag/Fe/GaAs (110) undoped, n-doped, and p-doped samples in three different crystallographic directions.

6.5 Summary

In this chapter, the effect of substrate doping on the magnetic anisotropy, g-factor, and damping of 5 nm capped Fe film grown on GaAs (110) has been investigated using FMR. The samples (4 nm Pt/3 nm Ag/5 nm Fe/GaAs) were grown *in situ* using MBE and characterized using *ex situ* FMR. A quantitative shift of magnetic properties has been observed in the doped sample as compared to the undoped sample. However, the actual origin or reason behind the observed effect is not clear. The magnetocrystalline anisotropy varies significantly with the doping of the substrate (10-30%) which might be due to the shift of Fermi level at the interface resulting in a change of the electronic structure of the Fe interface. The Gilbert damping parameter is also increased or decreased in the doped sample which can be due to interfacial spin-orbit interaction.

7 Conclusion and outlook

This thesis deals with the growth and characterization of Fe films grown on GaAs (100) and GaAs (110) substrate. *In situ* LEED, AES, and FMR techniques in UHV were utilized to extract the structural and magnetic properties of Fe films. The first goal of the thesis was to study the magnetic anisotropy in Fe films grown on GaAs (110) and (100) under high vacuum environment as a function of time. As a second goal, the influence of capping layer on the magnetic anisotropy, g-factor, and Gilbert damping of Fe/GaAs (100) was determined. Finally, the effect of substrate doping on the magnetic properties of Pt/Ag/Fe/GaAs (110) has been studied. The g-factor and Gilbert damping were determined using *in situ* frequency-dependent FMR measurements. For this purpose, the *in situ* FMR setup has been upgraded with a 40 GHz microwave short within the scope of this thesis.

The time-dependence of magnetic properties of Fe films grown on GaAs (110) and GaAs (100) was investigated using *in situ* FMR. Uncapped Fe films of different thicknesses were grown and measured at room temperature under UHV conditions. The results of Fe/GaAs (110) and Fe/GaAs (100) were compared regarding magnetic stability under UHV. After deposition in UHV, a continual variation of magnetocrystalline anisotropy was observed for Fe/GaAs (110) kept in a vacuum with time, while Fe/GaAs (100) shows a constant anisotropy over several hours. The transition speed of anisotropy change in Fe/GaAs (110) depends on the thickness of the Fe film. It was found that the morphological relaxation of the film surface results in a change of surface/interface anisotropy of 4 nm Fe/GaAs (110). Yet this transition is very slow and lasts over 6 days. The rapid change during the initial 24 hours leads to an unusual sign reversal of in-plane uniaxial anisotropy [72]. However, the transition for films with the lower thickness (1 and 2 nm) was found to be faster than for the 4 nm film. This could be due to the quick stabilization of crystal symmetry after deposition and the strong interface effect. Unlike Fe (110), Fe/GaAs (100) shows a negligible shift of anisotropy over several hours. The uniform growth is responsible for magnetic stability in Fe (100) film.

The structural and magnetic property of Fe film is significantly affected by the surface reconstruction of GaAs surface [16, 30]. Based on the comparison of the results of 4 nm Fe/GaAs (110) with 4 nm Fe/GaAs (100), the following conclusions have been made:

- Fe on GaAs (110) with no surface reconstruction gives 3D island growth resulting in a rough film. On the contrary, Fe on GaAs (100) with a surface reconstruction $\{1 \times 6\}$ gives layer-by-layer growth leading to a smooth film.
- Fe/GaAs (100) is magnetically more stable in time than Fe/GaAs (110) under UHV conditions at room temperature.
- The structural and morphological changes at the film surface are directly correlated to the magnetic anisotropy of Fe (110) film.

This time-dependent results allow to choose a suitable heterostructure for spintronic application where the magnetic anisotropy can be tuned with time.

Furthermore, the effect of the Pt/Ag capping layer on the magnetic anisotropy, g -factor, and Gilbert damping on 5 nm Fe film grown on GaAs (100) has been investigated using *in situ* FMR. *In situ* setup allows the characterization with or without a capping layer on the same film without breaking the vacuum. This gives a good comparison with the least possible oxidation. Depending on the surface reconstruction of GaAs (100) [83], the in-plane cubic and uniaxial anisotropy vary. It was demonstrated that the capping layer has an insignificant effect on the in-plane anisotropy while showing a considerable reduction of ~78% in the out-of-plane anisotropy. This is due to the change of the surface states of Fe film after capping.

An enhanced g -factor was observed for uncapped Fe films because of the increased orbital moment at the surface. The enhanced orbital moment is attributed to the increased electron localization at the surface due to reduced symmetry. However, these surface states are delocalized by Ag capping resulting in a reduction of Fe moment leading to bulk-like g -factor ($g = 2.09$). The intrinsic Gilbert damping parameter was also found to be dependent on the capping layer. The capping of non-magnetic metal Ag and a heavy metal Pt leads to an increase of the Gilbert damping term. This increase is attributed to the enhanced spin-orbit coupling and decrease in the relaxation rate at the interface. The remarked effects of

the capping layer on the magnetic anisotropy, g-factor, and damping parameter are directly correlated to the significant shift in the electronic band structure of Fe film at the surface and interface of the heterostructure.

In addition, the effect of doping GaAs substrate on the magnetic anisotropy, g-factor, and Gilbert damping of Pt/Ag/Fe/GaAs (110) heterostructure was studied. For this purpose, the samples were deposited in UHV using MBE and measured *ex situ* using CPW setup, which allows for measurements in the frequency range of 1-40 GHz. The determined anisotropy constants, g-factor, and Gilbert damping parameter α have been quantitatively explained. A notable change in all the parameters except the g-factor was found. Isotropic bulk-like g-factor was found for all samples regardless of doping. The mechanism leading to this change in magnetic properties by substrate doping is not clear yet. We propose that the doping in GaAs induces a chemical potential shift of the Fermi level resulting in the modification of spin-orbit coupling at the Fe/GaAs interface, which affects the magnetic properties such as anisotropy and Gilbert damping.

Our investigation provides quantitative information of magnetic anisotropy, g-factor, and intrinsic Gilbert damping parameter α of Fe film grown in GaAs (110) and GaAs (100) as a function of time, capping, and substrate doping. The role of surface morphology and growth mode in magnetic anisotropy is quantified. The impact of interfacial spin-orbit coupling on the magnetic relaxation mechanism is identified. Moreover, an *in situ* frequency-dependent FMR measurement over a wide range of frequencies (7-40 GHz) on Fe film is presented for the first time. These results are important not only as fundamental information on such heterostructures which can be utilized to understand the aging of thin films under UHV conditions but also for applications in spintronic devices. The present investigation allows one to compare the magnetic anisotropy and damping on two surface orientations of GaAs.

For further studies, we propose a complete thickness-dependent investigation with capping in steps, e.g., 1,2,3,4 nm Ag and 1,3,5 nm Pt. The angular and frequency-dependent FMR measurement at each step will provide detailed information about how the magnetic

Conclusion & outlook

anisotropy, g-factor, and damping is varying with capping layers. It would also be interesting to look into the results with an insulating or ferromagnetic capping. Furthermore, theoretical calculations (band structure) on these heterostructures will explain the mechanism behind the observed effect. This will also provide a better understanding of physical phenomena occurring at the FM/SC interface.

8 Appendix

8.1 Magnetocrystalline anisotropy of Fe films

The observed magnetic anisotropy in Fe films grown on semiconductor substrates particularly Fe/GaAs (001) is a point of intense scientific discussion till now for the device application. Therefore, it is of high interest to understand the different contributions to the magnetocrystalline anisotropy as a function of thickness, temperature, roughness, substrate reconstruction, and capping layer. The main focus of this section is to quantitatively review the magnetic anisotropy parameters from published literature and compare them with the observed values in this thesis. The systematic approach will allow magnetism researchers to easily find various anisotropy contributions present in Fe films and compare as well as analyze them with respect to related systems.

The thickness dependence of magnetic properties in Fe film grown on GaAs is known since Xu et al. [28] showed that the ferromagnetism evolves with increasing thickness in Fe film in three phases (nonmagnetic phase for the initial $3\frac{1}{2}$ MLs, a short-range-ordered superparamagnetic phase, and a ferromagnetic phase above ~ 5 ML). The thickness dependence of magnetic anisotropy in Fe/GaAs samples is also well understood now after several experimental observations [15, 16, 20, 29, 35, 123, 124] using MOKE, FMR, and BLS. The two main contributions to the magnetocrystalline anisotropy in Fe/GaAs i.e., in-plane uniaxial anisotropy and four-fold cubic anisotropy varies in the opposite direction with increasing film thickness. The effective four-fold cubic anisotropy $K_{4\parallel}^{eff}$ is largest for a bulk Fe while it approaches zero or eventually turns negative in the ultrathin limit of Fe film. On the other hand, the effective uniaxial anisotropy $K_{2\parallel}^{eff}$ shows a strong increase with decreasing thickness. The effective cubic anisotropy is a collective contribution from effective volume and interfaces having opposite signs. The critical thickness at which the in-plane reorientation of four-fold easy and hard axis occurs t_c^{RO} gives the proportional relation between effective interface and volume contributions [125]:

$$\frac{-K_{4\parallel}^{eff\,int}}{K_{4\parallel}^{eff\,vol}} = t_c^{RO} \quad (8.1)$$

On the contrary, the in-plane uniaxial anisotropy contribution is a purely interfacial character ($K_{2\parallel}^{eff\,vol} = 0$). Due to its interface/surface sensitivity, the uniaxial anisotropy is significantly affected by the substrate preparation/surface reconstruction and substrate/film or film/capping interface. Table 8-1 gives the in-plane uniaxial and cubic anisotropy constant values for Fe film grown on GaAs (both (100) and (110) orientation) determined by various groups in the past and its comparison with this work. The difference in the sign of $K_{2\parallel}$ comes from different definitions of the free energy density function equation used to fit the angular dependent resonance field data (this work used equation 2.18 and equation 2.19). The percentage change in the cubic and uniaxial anisotropy increases with decreasing thickness of Fe film due to strong surface/interface effect particularly in Fe/GaAs (100) samples where the surface reconstruction of GaAs plays an important role in manipulating the in-plane uniaxial anisotropy. Other capping layers e.g. Au [106, 124], Cu [126] also showed a dramatic reduction of uniaxial anisotropy energy.

Another important contribution to the magnetocrystalline anisotropy in Fe/GaAs system is out-of-plane magnetic anisotropy. This is again a combination of volume and interface/surface contribution and has a thickness dependence. The total effective out-of-plane anisotropy of an Fe film grown on GaAs can be described as:

$$K_{2\perp}^{eff} = K_{2\perp}^{eff\,vol} + \frac{K_{2\perp}^{Fe/GaAs} + K_{2\perp}^{cap/Fe}}{t} \quad (8.2)$$

The volume contribution to the perpendicular uniaxial anisotropy $K_{2\perp}^v$ mainly originates from the in-plane stress or out-of-plane strain caused by vertical lattice parameter enhancement in the Fe film grown on GaAs (100). However, the surface/interface $K_{2\perp}^{int}$ contribution comes essentially from Fe/vacuum or Fe/capping interface where the spin-orbit interaction is strongly enhanced or reduced [90]. Therefore, the capping layer significantly

modifies the uniaxial out-of-plane anisotropy $K_{2\perp}$ observed in this work as well as previous studies as tabulated in Table 8-1.

The temperature dependence of magnetic anisotropy and its correlation with the magnetization was investigated by Zakeri et al. [127]. The Callen-Callen model [40] describes the temperature dependence of anisotropy coefficients and the magnetization by equation (2.11). The temperature dependence of perpendicular magnetic anisotropy $K_{2\perp}^{eff}$ is directly correlated to the temperature dependence of perpendicular strain component in Fe films according to:

$$K_{2\perp}^{MLE}(T) = \frac{3}{2} B_1 \epsilon_{\perp}(T) \tag{8.3}$$

where B_1 is the magneto-elastic coupling constant of the Fe film and ϵ_{\perp} is the perpendicular strain component.

The roughness in the film surface or interface coming from the surface reconstruction of GaAs substrate can induce in-plane magnetic anisotropy. The theory behind the observed roughness-induced anisotropy in ferromagnetic films was explained by Arias et. al. [128]. The surface modulation in the thin films results in fluctuation of the magnetization direction, thus generating stray dipolar fields. This dipolar mechanism is responsible for roughness-induced anisotropy [128] and has been used to tune the in-plane uniaxial anisotropy in Fe film [129]. A detailed discussion on the calculation of different contributions of spin-orbit and dipolar anisotropy in smooth, rough, and real films can be found in the appendix section of [19].

Sample	Frequency (GHz)	GaAs Orientation/ reconstruction	Fe (nm)	$K_{2\parallel}$ ($\times 10^4 J$ $/m^3$)	$K_{4\parallel}$ ($\times 10^4 J$ $/m^3$)	Ref
Fe-bulk					4.2	[130]
(30 ML) Fe [*]	9.3	{4 × 6} (100)	4.3	-0.4	4.7	[90]
(10 ML) Fe [*]	9.3	{4 × 6} (100)	1.4	-5.5	1.5	[90]
(34.8 ML) Fe	13	{4 × 6}, {1 × 6} (100)	5	1.3	3.5	This work
(2 ML) Ag/Fe [*]	9.3	{4 × 6} (100)	4.3	-0.4	4.6	[90]
(2 ML) Ag/Fe [*]	9.3	{4 × 6} (100)	2.9	-0.5	3.8	[65]
(9.8 ML) Ag/Fe	13	{4 × 6}, {1 × 6} (100)	5	1.3	3.1	This work
(20 ML) Au/Fe§		{4 × 6} (100)	4.7	2.6	3.05	[124]
(30 ML) Fe [*]	9.3	(110)	6.08	-0.78	3.2	[131]
(49.3 ML) Fe	12.88	(110)	10	1.71	4.05	[36]
(19.7 ML) Fe	13.05	(110)	4	1.25	3.57	This work
(28.8 ML) Fe†		(110)	4	2.4	2.0	[35]
(26.9 ML) Ag/Fe	9.5	(110)	6.08	1.8	3.1	[131]
(14.7 ML) Ag/Fe	13.08	(110)	5	2.3	3.6	This work

Table 8-1 Magnetocrystalline anisotropy of Fe film grown on GaAs measured at RT. All the samples mentioned were grown at RT. The thickness and energy unit conversion are as follows: for Fe (100) 1 ML = 1.435 Å, for Fe (110) 1 ML = 2.029 Å, for Ag 1 ML = 2.0425 Å, $1 \times 10^5 J/m^3 = 7.4 \mu eV/atom$, $1 J/m^3 = 10 erg/cm^3$.

*Different definition of free energy was used which yields opposite signs.

§Anisotropy was determined using MOKE.

† The sample was measured using BLS.

9 List of Figures

Figure 1.1 Zinc blende crystal structure of GaAs showing crystallographic directions and planes. The inset details the directions of the tetrahedral bonds on a Ga atom (taken from [19]).	2
Figure 1.2 Correlation between the coverage, morphology, and magnetic phase of Fe films grown on GaAs (001)-4x6 substrate at room temperature [28].	5
Figure 2.1 Schematic drawing of magnetization, applied field, and easy axis for a material.	8
Figure 2.2 Schematic representation of the coordinate system for the film planes.	12
Figure 2.3 Free energy surface of a cubic system with (a) $K_4 > 0$, (b) uniaxial in-plane anisotropy with $K_2 \gg 0$. The color scale does not contain any physical information.	13
Figure 2.4 Trajectory of magnetization according to equation 2.13 [42].	14
Figure 2.5 Schematic illustration of different relaxation processes. Reproduced from [45].	19
Figure 2.6 Schematic illustration of (a) LLG equation and (b) Bloch-Bloembergen process of spin-spin relaxation taken from [48].	19
Figure 2.7 Schematic diagram of FMR linewidth as a function of frequency taken from [58]. The dashed line corresponds to pure Gilbert damping represented by equation 2.24, the dotted curve corresponds to two-magnon scattering represented by equation 2.28, and the solid curve is the sum of all contributions. The shaded area shows the offset in the linewidth coming from inhomogeneous broadening.	23
Figure 3.1 The UHV set-up is showing essential elements in a cross-section of the vacuum chamber in the x-z plane. Manipulator (M), <i>in situ</i> screwdriver (SD), evaporator (EV), quartz monitor (QM), sputter gun (SG).	26
Figure 3.2 Schematic diagram of the evaporation process [42].	27
Figure 3.3 Block diagram of the UHV setup describing the connections in a simplified form. The UHV valves separate the UHV area from one part to another, venting valves BE facilitating the venting through dry Nitrogen, 'el' stands for electrically controlled valves which prevent unintentional ventilation of the main chamber in case of power failure, and FD is for the finely metered intake of gases like Ar for sputtering [42].	28

Figure 3.4 Experimental inelastic mean free path as a function of energy for different materials [61].	30
Figure 3.5 (a) Ewald construction for diffraction from a 2D surface (b) with lattice periodicity [62].	30
Figure 3.6 Schematic of the Auger process (a) high energy electron impacts on an atom (b) ionization of core-level electron (c) excess energy transferred to outer-shell electron leading to ejection [62].	31
Figure 3.7 The schematic detection path of FMR for <i>in situ</i> set-up. Microwave power is transmitted from the synthesizer via circulator (C) and to a short circuit (S). The sample is approached from above and is then in the high-frequency field. Additionally, in the glass area where the short circuit an external magnetic field (A) and a modulation field (B) are applied. The reflected microwave power is transmitted via the circulator (C) to the microwave diode (D) guided. The signal rectified there goes to the lock-in amplifier.	34
Figure 3.8 Atomic force microscopy diagram showing scanning cantilever with the optical lever (laser and photodiode), which amplifies tiny deflections of cantilever [64].	36
Figure 3.9 Schematic of <i>ex situ</i> FMR setup.	37
Figure 4.1 (a) Top view of GaAs (110) surface. (b) LEED pattern of cleaned GaAs (110) substrate at an energy of 117 eV.	41
Figure 4.2 (a) LEED pattern of 4 nm Fe/GaAs (110) taken at an energy of 186 eV. (b) AFM scan of the same film (1x1 μm area) oxidized in air. (c) Line profile of the blue line in the image (b) [72].	41
Figure 4.3 (a) Normalized FMR spectra of 4 nm Fe/GaAs (110) film 1 in the first hour after deposition. (b) Time-dependent FMR of 4 nm Fe/GaAs (110), starting from two hours after deposition with the magnetic field applied parallel to the [110] direction. Red dots show the resonance field of film 2 at different time intervals. Inset shows the overlapped FMR spectra of film 1 and film 2 measured after deposition in [110] direction. Single FMR spectra at the 2 nd , 12 th , and 62 nd hour of film 1 are shown separately.	42
Figure 4.4 Azimuthal angular dependence of the resonance field of 4 nm Fe/GaAs (110) film 2 at a microwave frequency of 13.054 GHz at different times. The solid lines are fit to the experimental data (open symbols) according to equation 2.19 [72].	44
Figure 4.5 (a) Angular-dependent peak-to-peak linewidth of 4 nm Fe/GaAs (110) film 2 at different periods. (b) Linewidth at intermediate and hard direction as a function of time..	45
Figure 4.6 AES spectrum of 4 nm Fe/GaAs (110) just after deposition and after 6 days under UHV conditions.	47

Figure 4.7 AES spectrum (a) showing Ga and As peaks before and after 2 nm Fe deposition on GaAs (110), and (b) showing Fe peaks after deposition and after 3 days in a vacuum. .48	48
Figure 4.8 Angular-dependent FMR of 2 nm Fe/GaAs (110) measured (a) after deposition and (b) 69 hours after deposition. Greyscale represents the normalized amplitude of microwave absorption.49	49
Figure 4.9 (a) Azimuthal angular dependence of the resonance field of 2 nm Fe/GaAs (110) at a microwave frequency of 12.069 GHz at different times. The solid lines are fit to the experimental data (open symbols). Only prominent resonance field positions were selected for fitting purposes. (b) FMR spectra taken at the intermediate direction ($\Phi_H = 90^\circ$) after deposition and after 69 hours.49	49
Figure 4.10 AES spectra of 1 nm Fe/GaAs (110) (a) Ga and As peaks before and after deposition. Inset shows the LEED pattern of 1 nm Fe/GaAs (110) taken at 113 eV after deposition. (b) Fe peaks before and after deposition as well as after 9 days in a vacuum...50	50
Figure 4.11 (a) Azimuthal angular dependence of the resonance field of 1 nm Fe/GaAs (110) at a microwave frequency of 12.069 GHz taken one day and 6 days after deposition. Open symbols are the experimental data, and the solid lines are the fit according to equation 2.19. (b) Angular-dependent linewidth of 1 nm Fe/GaAs (110) at different times. (c) FMR spectra of 1 nm Fe/GaAs (110) measured <i>in situ</i> after 1 day in [110] and [001] directions.52	52
Figure 4.12 Anisotropy constants of Fe/GaAs (110) as a function of time for different thicknesses of Fe. The error bars of $K_2 \parallel$ are smaller than the symbol size ($\pm 0.05 \times 10^4 \text{ J/m}^3$).54	54
Figure 4.13 (a) Auger spectrum of a clean As-rich GaAs (100) substrate surface. The numbers show the energy in eV of Ga and As peaks. The inset shows the spectrum of the same substrate recorded at lower energies indicating the presence of carbon and oxygen. (b) A LEED pattern of ordered (1×6) reconstructed GaAs (100) substrate taken at an energy of 63 eV.56	56
Figure 4.14 (a) Auger spectrum of 4 nm Fe/GaAs (100) just after deposition and 7 days after deposition. Inset of (a) shows the lower energy scan taken 7 days after deposition. (b) A LEED pattern of 4 nm Fe/GaAs (100) taken at an energy of 117 eV showing a well-ordered BCC structure.56	56
Figure 4.15 (a) FMR spectra of 4 nm Fe/GaAs (100) taken in [110] direction 50 minutes and 100 minutes after deposition (b) Time-dependent FMR of 4 nm Fe/GaAs (100) taken at room temperature and 12.931 GHz two with the magnetic field applied parallel to [110] direction. Greyscale reflects the normalized amplitude of the microwave absorption derivative, which is proportional to $\partial\chi''/\partial B$. Red dots show the resonance field position $\mu_0 H r$ of each spectrum. The error bars of $\mu_0 H r$ (red dots) are smaller than the symbol size.57	57

Figure 4.16 (a) Time-dependent FMR linewidth of 4 nm Fe/GaAs (100). Inset shows the LEED pattern of 4 nm Fe/GaAs (100) on the 7 th day after deposition taken at 207 eV. (b) <i>Ex situ</i> AFM scan of same film (1×1 μm area) oxidized in air and line profile of the blue line in the image.	57
Figure 5.1 Schematic of prepared sample and characterization followed the sample preparation <i>in situ</i> and <i>ex situ</i>	61
Figure 5.2 LEED image of (a) GaAs (100) at 108 eV, (a*) GaAs (100) at 64 eV, (b) 5 nm Fe/GaAs (100) at 116 eV, (c) 5 nm Fe/GaAs (100) at 176 eV, (d) Fe/GaAs (100) at 176 eV after 101 hours, (e) 2 nm Ag on 5 nm Fe/GaAs (100) at 62 eV, (f) crystallographic directions of GaAs (001).	62
Figure 5.3 AES of 5 nm Fe on GaAs (100) taken after Fe deposition and after 2 nm Ag deposition.	63
Figure 5.4 AES of 3 nm Pt/Ag/Fe/GaAs (100) taken after Pt deposition and after 10 minutes sputtering at room temperature.	64
Figure 5.5 FMR spectra of the uncapped and capped 5 nm Fe/GaAs (100) film in three different crystallographic directions of the sample, as shown in Figure 5.2 (f).	66
Figure 5.6 Azimuthal angular dependence of the resonance field of uncapped 5 nm Fe/GaAs (100) measured <i>in situ</i> and capped film Pt/Ag/Fe/GaAs (100) measured <i>ex situ</i> at a microwave frequency of 13±0.02 GHz. The solid lines are the fits to the experimental data (open circles) using equation 2.18. The error bar of the resonance field data points is smaller than the symbol size.	67
Figure 5.7 Frequency-dependent FMR of uncapped Fe/GaAs (100) measured <i>in situ</i> with the magnetic field applied parallel to [110] direction in the film plane. The greyscale represents the normalized amplitude of the microwave absorption derivative proportional to $\partial\chi''/\partial B$	71
Figure 5.8 The square of microwave frequency versus the resonance field in the easy and hard direction of uncapped and capped 5 nm Fe/GaAs (100). The error bar for all the data points is smaller than the symbol size. The solid lines are the fit to the data according to the equations (2.20) and (2.21).	73
Figure 5.9 The square of microwave frequency versus the resonance field in the intermediate direction of uncapped and capped 5 nm Fe/GaAs (100). The error bar of data points is smaller than the symbol size. The solid lines are the fit to the data according to equations (2.20) and (2.21).	73
Figure 5.10 Angular dependent peak-to-peak linewidth of uncapped 5 nm Fe/GaAs (100) measured <i>in situ</i> and capped Pt/Ag/Fe sample measured <i>ex situ</i> at a microwave frequency of 12 GHz. The error bar for each data point is smaller than the symbol size.	75

Figure 5.11 Frequency-dependent peak-to-peak linewidth of uncapped and capped 5 nm Fe/GaAs (100) in (a) the easy [100] and (b) intermediate [110] direction.	76
Figure 5.12 Frequency-dependent peak-to-peak linewidth of uncapped and capped 5 nm Fe/GaAs (100) in the hard [110] direction.	76
Figure 6.1 Schematic of prepared sample and characterization followed during sample preparation <i>in situ</i> and <i>ex situ</i>	82
Figure 6.2 LEED images taken <i>in situ</i> : (a) GaAs (110) undoped at 97 eV, (b) GaAs (110) p-doped at 78 eV, (c) GaAs (110) n-doped at 130 eV, (d) 5 nm Fe/GaAs (110) undoped at 177 eV, (e) 5 nm Fe/GaAs (110) p-doped at 75 eV, (f) 5 nm Fe/GaAs (110) n-doped at 156 eV.	83
Figure 6.3 AES spectrum taken <i>in situ</i> after deposition of the complete sample Pt/Ag/Fe/GaAs (110) undoped.....	84
Figure 6.4 In-plane angular-dependent <i>ex situ</i> FMR measurement of 4 nm Pt/3 nm Ag/5 nm Fe/GaAs (110) p-doped sample taken at 12.902 GHz and room temperature. The grey scale corresponds to the normalized FMR amplitude. Inset gives a schematic representation of crystallographic directions of the (110) surface.	85
Figure 6.5 FMR spectra of Pt/Ag/Fe/GaAs (110) undoped, n-doped, and p-doped sample in three different crystallographic directions. The solid line represents complex Lorentzian fit to the experimental data.	86
Figure 6.6 Angular-dependent resonance field of Pt/Ag/Fe/GaAs (110) undoped, n-doped, and p-doped sample. The solid line shows the best fit to the data according to equation 2.19 yielding anisotropy parameters tabulated in Table 6-1.	88
Figure 6.7 Frequency-dependent resonance field of Pt(4 nm)/Ag(3 nm)/Fe(5 nm) heterostructure grown on undoped, p-doped, and n-doped GaAs (110) substrate measured in-plane in (a) [001] easy, (b) [111] hard, and (c) [110] intermediate direction. The error bar for all data points is smaller than the symbol size.....	90
Figure 6.8 Frequency-dependent peak-to-peak linewidth (open circles) and its linear fit (solid line) of Fe/GaAs (110) undoped, p-doped, and n-doped sample in (a) [001] direction, (b) [111] direction, and (c) [110] direction.	92

10 List of Tables

Table 4-1 Comparison between two samples of resonance field and linewidth measured along [110] direction at different times. The error bars for all the values are less than 1%.	59
Table 5-1 Room temperature magnetic anisotropy constants of 5 nm Fe film grown on GaAs (100) before and after capping. The error bar of the magnetic anisotropy parameter is below %. The integers in the first column denote the thickness of the layer in nm.	69
Table 5-2 Spectroscopic splitting g-factor of 5 nm Fe/GaAs (100) before and after capping, measured in three different crystallographic directions. The integers in brackets denote the thickness of the layer in nm.	74
Table 5-3 The slope of linear fit extracted from frequency-dependent linewidth of uncapped and capped 5 nm Fe film measured for three different crystallographic orientations.	78
Table 5-4 Inhomogeneous broadening ΔH_0 of uncapped and capped sample determined by the linear fit of frequency-dependent linewidth.	78
Table 5-5 Gilbert damping parameter α of uncapped and capped sample in three different crystallographic directions.	78
Table 6-1 Room temperature anisotropy parameters of Pt/Ag/Fe/GaAs (110) undoped, p-doped, and n-doped samples determined by fitting angular dependent resonance field using equation 2.19.	87
Table 6-2 The slope of the linear fit of the frequency-dependent linewidth of Pt/Ag/Fe/GaAs (110) undoped, n-doped, and p-doped samples measured for three different crystallographic orientations (Figure 6.8).	90
Table 6-3 Inhomogeneous broadening ΔH_0 of Pt/Ag/Fe/GaAs (110) undoped, n-doped, and p-doped samples determined by the linear fit of frequency-dependent linewidth.	91
Table 6-4 Gilbert damping parameter of Pt/Ag/Fe/GaAs (110) undoped, n-doped, and p-doped samples in three different crystallographic directions.	92
Table 8-1 Magnetocrystalline anisotropy of Fe film grown on GaAs measured at RT. All the samples mentioned were grown at RT. The thickness and energy unit conversion are as follows: for Fe (100) 1 ML = 1.435 Å, for Fe (110) 1 ML = 2.029 Å, for Ag 1 ML = 2.0425 Å, $1 \times 10^5 \text{ J/m}^3 = 7.4 \mu\text{eV/atom}$, $1 \text{ J/m}^3 = 10 \text{ erg/cm}^3$	101

11 Bibliography

- [1] R. Godfrey and Johnson M., *Spin injection in mesoscopic silver wires: Experimental test of resistance mismatch*. Phys Rev Lett. **96** 13: p. 136601 (2006).
- [2] G.A. Prinz, *Spin-polarized transport*. Physics Today. **48** 4: p. 58-63 (1995).
- [3] K. Tivakornsasithorn, et al., *Magnetization reversal and interlayer exchange coupling in ferromagnetic metal/semiconductor Fe/GaMnAs hybrid bilayers*. Sci Rep. **8** 1: p. 10570 (2018).
- [4] J.A.C.Bland and B. Heinrich, *Ultrathin magnetic structures i*. Vol. 1. Springer, Berlin, Heidelberg, (1994).
- [5] M. Tanaka, *Recent progress in ferromagnetic semiconductors and spintronics devices*. Japanese Journal of Applied Physics. **60** 1 (2020).
- [6] Y. Guo, et al., *Spin-constrained optoelectronic functionality in two-dimensional ferromagnetic semiconductor heterojunctions*. Materials Horizons. **8** 4: p. 1323-1333 (2021).
- [7] G.A. Prinz, *Magnetoelectronics*. Science. **282** 5394: p. 1660 (1998).
- [8] S.A. Wolf, et al., *Spintronics: A spin-based electronics vision for the future*. Science. **294** 5546: p. 1488 (2001).
- [9] R. Fiederling, et al., *Injection and detection of a spin-polarized current in a light-emitting diode*. Nature. **402** 6763: p. 787-790 (1999).
- [10] H.J. Zhu, et al., *Room-temperature spin injection from Fe into GaAs*. Phys Rev Lett. **87** 1: p. 016601 (2001).
- [11] P.K. Wong, et al., *Spin-dependent transport in Fe/GaAs(100)/Fe vertical spin-valves*. Sci Rep. **6**: p. 29845 (2016).
- [12] C.H. Li, et al., *Spin injection across (110) interfaces: Fe/GaAs(110) spin-light-emitting diodes*. Applied Physics Letters. **85** 9: p. 1544-1546 (2004).
- [13] L. Chen, et al., *Robust spin-orbit torque and spin-galvanic effect at the Fe/GaAs (001) interface at room temperature*. Nat Commun. **7**: p. 13802 (2016).
- [14] L. Chen, et al., *Electric-field control of interfacial spin-orbit fields*. Nature Electronics. **1** 6: p. 350-355 (2018).
- [15] R. Höllinger, et al., *In-plane spin reorientation transitions in epitaxial Fe(110)/GaAs(110) films*. Journal of Applied Physics. **89** 11: p. 7136-7138 (2001).
- [16] M. Gester, et al., *Continuous evolution of the in-plane magnetic anisotropies with thickness in epitaxial Fe films*. Journal of Applied Physics. **80** 1: p. 347-355 (1996).
- [17] L. Chen, et al., *Emergence of anisotropic Gilbert damping in ultrathin Fe layers on GaAs(001)*. Nature Physics. **14** 5: p. 490-494 (2018).

-
- [18] L. Yang, et al., *Large anisotropy of magnetic damping in ultrathin epitaxial Fe/GaAs (0 0 1) film*. Journal of Physics D: Applied Physics. **53** 11: p. 115004 (2020).
- [19] G. Wastlbauer and Bland * J.A.C., *Structural and magnetic properties of ultrathin epitaxial Fe films on GaAs(001) and related semiconductor substrates*. Advances in Physics. **54** 2: p. 137-219 (2005).
- [20] J.J. Krebs, Jonker B.T., and Prinz G.A., *Properties of Fe single-crystal films grown on (100)GaAs by molecular-beam epitaxy*. Journal of Applied Physics. **61** 7: p. 2596-2599 (1987).
- [21] J.R. Waldrop and Grant R.W., *Interface chemistry of metal-GaAs schottky-barrier contacts*. Applied Physics Letters. **34** 10: p. 630-632 (1979).
- [22] G. Wedler, et al., *Stress evolution during Fe(001) epitaxy on GaAs(001)*. Applied Physics Letters. **78** 9: p. 1270-1272 (2001).
- [23] T. Ashraf, et al., *Growth, structure and morphology of epitaxial Fe(0 0 1) films on GaAs(0 0 1)c(4 x 4)*. J Phys Condens Matter. **27** 3: p. 036001 (2015).
- [24] A. Filipe, Schuhl A., and Galtier P., *Structure and magnetism of the Fe/GaAs interface*. Applied Physics Letters. **70** 1: p. 129-131 (1997).
- [25] S.C. Erwin, Lee S.-H., and Scheffler M., *First-principles study of nucleation, growth, and interface structure of Fe/GaAs*. Physical Review B. **65** 20 (2002).
- [26] K.-i. Sano and Miyagawa T., *Surface segregations during epitaxial growth of Fe/Au multilayers on GaAs(001)*. Japanese Journal of Applied Physics. **30** Part 1, No. 7: p. 1434-1441 (1991).
- [27] S. Mirbt, et al., *First-principles calculations of Fe on GaAs(100)*. Physical Review B. **67** 15 (2003).
- [28] Y. Xu, et al., *Evolution of the ferromagnetic phase of ultrathin Fe films grown on GaAs (100)-4x 6*. Physical Review B. **58** 2: p. 890 (1998).
- [29] R. Moosbühler, et al., *Epitaxial Fe films on GaAs(001): Does the substrate surface reconstruction affect the uniaxial magnetic anisotropy?* Journal of Applied Physics. **91** 10 (2002).
- [30] C. Godde, et al., *Structural changes and alloying of annealed iron layers on GaAs(001) and GaAs(110)*. Surface Science. **602** 21: p. 3343-3351 (2008).
- [31] K. Zakeri, et al., *Magnetic anisotropy of Fe/GaAs(001) ultrathin films investigated by in situ ferromagnetic resonance*. Journal of Magnetism and Magnetic Materials. **299** 1: p. L1-L10 (2006).
- [32] D.M. Gillingham, et al., *Smoothing of ultrathin Fe films grown on GaAs(100) observed by scanning tunneling microscopy and brillouin light scattering*. Physical Review B. **76** 21 (2007).
- [33] G. Chen, et al., *Revealing the volume magnetic anisotropy of Fe films epitaxied on GaAs(001) surface*. Applied Physics Letters. **98** 13 (2011).

-
- [34] G. Bayreuther, et al., *Uniaxial magnetic anisotropy in Fe/GaAs(001): Role of magnetoelastic interactions*. Physical Review B. **86** 5 (2012).
- [35] M. Madami, et al., *Thickness dependence of magnetic anisotropy in uncovered and cu-covered Fe/GaAs(110) ultrathin films studied by in situ brillouin light scattering*. Journal of Applied Physics. **99** 8 (2006).
- [36] F.M. Römer, et al., *In situ multifrequency ferromagnetic resonance and x-ray magnetic circular dichroism investigations on Fe/GaAs(110): Enhanced g-factor*. Applied Physics Letters. **100** 9: p. 092402 (2012).
- [37] M. Farle, *Ferromagnetic resonance of ultrathin metallic layers*. Reports on Progress in Physics. **61** 7: p. 755-826 (1998).
- [38] P. Bruno, *Tight-binding approach to the orbital magnetic moment and magnetocrystalline anisotropy of transition-metal monolayers*. Physical Review B. **39** 1: p. 865-868 (1989).
- [39] J.M.D. Coey, *Magnetism and magnetic materials*. Cambridge University Press, (2010).
- [40] H.B. Callen and Callen E., *The present status of the temperature dependence of magnetocrystalline anisotropy, and the $l(l+1)2$ power law*. Journal of Physics and Chemistry of Solids. **27** 8: p. 1271-1285 (1966).
- [41] T.L. Gilbert, *Classics in magnetics a phenomenological theory of damping in ferromagnetic materials*. IEEE Transactions on Magnetism. **40** 6: p. 3443-3449 (2004).
- [42] F.M. Römer, *Breitbandige in situ ferromagnetische resonanz und niederfrequente suszeptibilitätsmessungen an eisen auf iii-v halbleitern*, in *Faculty of Physics*, der Universität Duisburg-Essen: Duisburg. (2012).
- [43] S.V. Vonsovskii, *Chapter i - magnetic resonance in ferromagnetics*, in *Ferromagnetic resonance*, S.V. Vonsovskii, Editor. 1966, Pergamon. p. 1-11.
- [44] J. Smit, *Ferromagnetic resonance absorption in BaFe₁₂O₁₉, a highly anisotropic crystal*. Philips Res. Rep. **10**: p. 113-130 (1955).
- [45] K. Baberschke, *Investigation of ultrathin ferromagnetic films by magnetic resonance*. Handbook of Magnetism and Advanced Magnetic Materials. (2007).
- [46] F. Bloch, *Nuclear induction*. Physical Review. **70** 7-8: p. 460-474 (1946).
- [47] N. Bloembergen, *On the ferromagnetic resonance in nickel and supermalloy*. Physical Review. **78** 5: p. 572-580 (1950).
- [48] K. Lenz, et al., *Two-magnon scattering and viscous Gilbert damping in ultrathin ferromagnets*. Physical Review B. **73** 14 (2006).
- [49] E. Barati, et al., *Gilbert damping in magnetic layered systems*. Physical Review B. **90** 1 (2014).
- [50] V. Kamberský, *Spin-orbital Gilbert damping in common magnetic metals*. Physical Review B. **76** 13 (2007).

-
- [51] V. Kamberský, *On ferromagnetic resonance damping in metals*. Czechoslovak Journal of Physics B. **26** 12: p. 1366-1383 (1976).
- [52] B. Heinrich, Meredith D.J., and Cochran J.F., *Wave number and temperature dependent Landau-Lifshitz damping in nickel*. Journal of Applied Physics. **50** B11: p. 7726-7728 (1979).
- [53] Y. Tserkovnyak, Brataas A., and Bauer G.E.W., *Spin pumping and magnetization dynamics in metallic multilayers*. Physical Review B. **66** 22: p. 224403 (2002).
- [54] K. Gilmore, et al., *Anisotropic damping of the magnetization dynamics in Ni, Co, and Fe*. Physical Review B. **81** 17 (2010).
- [55] R. Meckenstock, et al., *Anisotropic Gilbert damping in epitaxial Fe films on InAs(001)*. Journal of Magnetism and Magnetic Materials. **272-276**: p. 1203-1204 (2004).
- [56] Y. Tserkovnyak, Brataas A., and Bauer G.E., *Enhanced Gilbert damping in thin ferromagnetic films*. Phys Rev Lett. **88** 11: p. 117601 (2002).
- [57] G. Woltersdorf and Heinrich B., *Two-magnon scattering in a self-assembled nanoscale network of misfit dislocations*. Physical Review B. **69** 18 (2004).
- [58] J. Lindner, et al., *Non-Gilbert-type damping of the magnetic relaxation in ultrathin ferromagnets: Importance of magnon-magnon scattering*. Physical Review B. **68** 6 (2003).
- [59] F.M. Römmer, *Aufbau einer Anlage zur Messung des magnetooptischen Kerr-Effektes für ex und in situ Messungen: Fe₃Si/MgO(001) und Co/GaAs(001)*, in *Fachbereich Physik*, Universität Duisburg-Essen: Duisburg. (2007).
- [60] G. Held, *Low-energy electron diffraction crystallography of surfaces and interfaces*, in *Bunsen-Magazin* Deutsche Bunsen-Gesellschaft für Physikalische Chemie e.V. p. 124-131. (2010).
- [61] M.K. K. Oura, A. V. Zotov, V. G. Lifshits, A. A. Saranin, *Surface science an introduction*. Springer, (2003).
- [62] T. Kebe, *SQUID-magnetometry on Fe monolayers on GaAs (001) in UHV*, in *Faculty of Physics*, Universität Duisburg-Essen. (2006).
- [63] T. Tański, et al., *Introductory chapter: Why atomic force microscopy (AFM) is one of the leading methods of surface morphology research of all engineering material groups*, in *Atomic-force microscopy and its applications*. 2019.
- [64] H.G. Hansma, *Atomic force microscopy and spectroscopy of silk from spider draglines, capture-web spirals, and silkworms*, in *Biotechnology of silk*. 2014, Springer Science, Business Media: Dordrecht.
- [65] K. Zakeri, et al., *Correlation between structure and magnetism in epitaxial Fe monolayers on GaAs(001)*. Superlattices and Microstructures. **41** 2-3: p. 116-121 (2007).

-
- [66] H.-P. Schönherr, et al., *Evolution of the surface morphology of Fe grown on GaAs (100), (311)a, and (331)a substrates by molecular beam epitaxy*. Journal of Applied Physics. **89** 1: p. 169-173 (2001).
- [67] M. Madami, et al., *In situ Brillouin scattering study of the thickness dependence of magnetic anisotropy in uncovered and Cu-covered Fe/GaAs(100) ultrathin films*. Physical Review B. **69** 14 (2004).
- [68] J. Weissman, et al., *Time stability of Fe films epitaxially grown on a GaAs substrate*. Materials Chemistry and Physics. **37** 2: p. 175-179 (1994).
- [69] O. Thomas, et al., *Interplay between anisotropic strain relaxation and uniaxial interface magnetic anisotropy in epitaxial Fe films on (001) GaAs*. Phys Rev Lett. **90** 1: p. 017205 (2003).
- [70] J. Lu, et al., *Anisotropic strain relaxation of thin Fe film on c(4×4) reconstructed GaAs (001) surface*. Physica E: Low-dimensional Systems and Nanostructures. **42** 2: p. 150-153 (2009).
- [71] R.A. Dragoset, et al., *Characterization of epitaxial Fe on GaAs(110) by scanning tunneling microscopy*. MRS Proceedings. **151**: p. 193 (1989).
- [72] B. Bhagat, et al., *Reversal of uniaxial magnetic anisotropy in Fe/GaAs (110) films driven by surface relaxation: An in situ ferromagnetic resonance study*. AIP Advances. **10** 7 (2020).
- [73] G.A. Prinz, Rado G.T., and Krebs J.J., *Magnetic properties of single-crystal {110} iron films grown on GaAs by molecular beam epitaxy (invited)*. Journal of Applied Physics. **53** 3: p. 2087-2091 (1982).
- [74] S.J. Steinmuller, et al., *Effect of substrate roughness on the magnetic properties of thin FCC Co films*. Physical Review B. **76** 5 (2007).
- [75] T. Kebe, et al., *Magnetization and magnetic anisotropy energy of ultrathin Fe films on GaAs(001) exposed to oxygen*. Journal of Physics: Condensed Matter. **18** 39: p. 8791-8802 (2006).
- [76] V.S. Smentkowski and Yates J.T., *The adsorption of oxygen on Fe(110) in the temperature range of 90 to 920 K*. Surface Science. **232** 1: p. 113-128 (1990).
- [77] M. Seo, Lumsden J.B., and Staehle R.W., *An aes analysis of oxide films on iron*. Surface Science. **50** 2: p. 541-552 (1975).
- [78] Y. Ding, Alexander C., and Klemmer T.J., *X-ray diffraction and ferromagnetic resonance study of sputtered (110) GaAs/Fe epitaxial films*. Journal of Applied Physics. **93** 10: p. 6674-6676 (2003).
- [79] K. Matsubara, et al., *Structure and magnetic properties of Fe epitaxial thin films prepared by uhv rf magnetron sputtering on GaAs single-crystal substrates*. Thin Solid Films. **519** 23: p. 8299-8302 (2011).
- [80] M.W. Ruckman, Joyce J.J., and Weaver J.H., *Interdiffusion and reaction at the Fe/GaAs(110) interface*. Physical Review B. **33** 10: p. 7029-7035 (1986).

-
- [81] U. Gradmann, Korecki J., and Waller G., *In-plane magnetic surface anisotropies in Fe(110)*. Applied Physics A. **39** 2: p. 101-108 (1986).
- [82] J.M. Shaw and Falco C.M., *Structure, spin dynamics, and magnetic properties of annealed nanoscale Fe layers on GaAs*. Journal of Applied Physics. **101** 3 (2007).
- [83] P. Drathen, Ranke W., and Jacobi K., *Composition and structure of differently prepared GaAs(100) surfaces studied by leed and aes*. Surface Science. **77** 1: p. L162-L166 (1978).
- [84] E.M. Kneeder, et al., *Influence of substrate surface reconstruction on the growth and magnetic properties of Fe on GaAs(001)*. Physical Review B. **56** 13: p. 8163-8168 (1997).
- [85] T.L. Monchesky, *Physics of low dimensional systems*. Springer, (2001).
- [86] M.O. Liedke, et al., *Crossover in the surface anisotropy contributions of ferromagnetic films on rippled si surfaces*. Physical Review B. **87** 2: p. 024424 (2013).
- [87] M. Körner, *Morphology-induced magnetic phenomena studied by broadband ferromagnetic resonance*, in *Fakultät Mathematik und Naturwissenschaften, Technischen, Universität Dresden: Dresden*. (2013).
- [88] V. Flovik, et al., *Eddy current interactions in a ferromagnet-normal metal bilayer structure, and its impact on ferromagnetic resonance lineshapes*. Journal of Applied Physics. **117** 14 (2015).
- [89] K. Zakeri, et al., *Power-law behavior of the temperature dependence of magnetic anisotropy of uncapped ultrathin Fe films on GaAs(001)*. Physical Review B. **73** 5 (2006).
- [90] K.Z. Lori, *Magnetic monolayers on semiconductor substrates an in-situ fmr study of Fe based hetrostructures*, in *Faculty of Physics, Universität Duisburg-Essen*. (2007).
- [91] R. Gupta, et al., *Interface structure of Fe/Ag multilayers prepared by pulsed laser deposition*. Physical Review B. **67** 7: p. 075402 (2003).
- [92] N.C. Koon, et al., *Direct evidence for perpendicular spin orientations and enhanced hyperfine fields in ultrathin Fe(100) films on ag(100)*. Physical Review Letters. **59** 21: p. 2463-2466 (1987).
- [93] Q. Xue, et al., *Structures of the Ga-rich 4 x 2 and 4 x 6 reconstructions of the GaAs(001) surface*. Phys Rev Lett. **74** 16: p. 3177-3180 (1995).
- [94] W. Keune, et al., *Influence of interfaces on the phonon density of states of nanoscale metallic multilayers: Phonon confinement and localization*. Physical Review B. **98** 2: p. 024308 (2018).
- [95] B. Heinrich and Cochran J.F., *Ultrathin metallic magnetic films: Magnetic anisotropies and exchange interactions*. Advances in Physics. **42** 5: p. 523-639 (1993).

-
- [96] B. Heinrich, et al., *Magnetic anisotropies in single and multilayered structures (invited)*. Journal of Applied Physics. **70** 10: p. 5769-5774 (1991).
- [97] P. Bruno, *Dipolar magnetic surface anisotropy in ferromagnetic thin films with interfacial roughness*. Journal of Applied Physics. **64** 6: p. 3153-3156 (1988).
- [98] L. Ruppel, et al., *Structural, chemical, and magnetic properties of Fe films grown on InAs(100)*. Physical Review B. **66** 24 (2002).
- [99] I.A. Vladymyrskyi, et al., *Influence of intermediate ag layer on the structure and magnetic properties of Pt/Ag/Fe thin films*. Vacuum. **101**: p. 33-37 (2014).
- [100] H.P. Wijn, *Magnetic properties of metals: D-elements, alloys and compounds*. Springer Science & Business Media, (2012).
- [101] C.T. Chen, et al., *Experimental confirmation of the x-ray magnetic circular dichroism sum rules for iron and cobalt*. Physical Review Letters. **75** 1: p. 152-155 (1995).
- [102] J.S. Claydon, et al., *Direct observation of a bulk-like spin moment at the Fe/GaAs(100)-4x6 interface*. Phys Rev Lett. **93** 3: p. 037206 (2004).
- [103] J.S. Claydon, et al., *Magnetic moments of ferromagnetic, superparamagnetic, and submonolayer Fe on a GaAs (100) surface*. Journal of Applied Physics. **95** 11: p. 6543-6545 (2004).
- [104] Y.B. Xu, et al., *Giant enhancement of orbital moments and perpendicular anisotropy in epitaxial Fe/GaAs(100)*. Journal of Applied Physics. **89** 11: p. 7156-7158 (2001).
- [105] J.B. Laloe, et al., *Room-temperature study of the magnetic moment of ultrathin Fe films on GaAs*. IEEE Transactions on Magnetics. **42** 10: p. 2933-2935 (2006).
- [106] S. Tacchi, et al., *Influence of au capping layer on the magnetic properties of Fe/GaAs(001) ultrathin films*. Surface Science. **601** 18: p. 4311-4315 (2007).
- [107] S. Ohnishi, Freeman A.J., and Weinert M., *Surface magnetism of Fe(001)*. Physical Review B. **28** 12: p. 6741-6748 (1983).
- [108] S. Ohnishi, Weinert M., and Freeman A.J., *Interface magnetism in metals: Ag/Fe(001)*. Physical Review B. **30** 1: p. 36-43 (1984).
- [109] S.V.Vonsovskii, *Ferromagnetic resonance the phenomenon of resonant absorption of a high-frequency magnetic field in ferromagnetic substances*. PERGAMON PRESS, (1996).
- [110] M. Caminale, et al., *Spin pumping damping and magnetic proximity effect in pd and pt spin-sink layers*. Physical Review B. **94** 1 (2016).
- [111] B. Heinrich, et al., *Spin pumping at the magnetic insulator (YIG)/normal metal (Au) interfaces*. Physical Review Letters. **107** 6: p. 066604 (2011).
- [112] I. Garate and MacDonald A., *Gilbert damping in conducting ferromagnets. Ii. Model tests of the torque-correlation formula*. Physical Review B. **79** 6: p. 064404 (2009).

-
- [113] G.A. Prinz and Krebs J.J., *Molecular beam epitaxial growth of single-crystal Fe films on GaAs*. Applied Physics Letters. **39** 5: p. 397-399 (1981).
- [114] F.A. Volkening, et al., *Mössbauer study of ^{57}Fe single-crystal films grown on (110) GaAs by mbe*. Journal of Applied Physics. **67** 9: p. 5646-5648 (1990).
- [115] L. Winking, et al., *Fe films grown on GaAs(110) in a two-step process: Improved structural and magnetic properties*. Applied Physics Letters. **92** 19 (2008).
- [116] A. Grünebohm, Herper H.C., and Entel P., *Ab initio study of the interface properties of Fe/GaAs(110)*. Physical Review B. **80** 6 (2009).
- [117] T. Iffländer, *Electronic and magnetic properties of the Fe/GaAs (110) interface*, in *Fakultät für Physik*, Georg-August-Universität Göttingen. (2015).
- [118] S.Y. Park, et al., *Controlling the magnetic anisotropy of the van der waals ferromagnet Fe_3GeTe_2 through hole doping*. Nano Lett. **20** 1: p. 95-100 (2020).
- [119] P.E. Wigen, *Dipole-narrowed inhomogeneously broadened lines in ferromagnetic thin films*. Physical Review. **133** 6A: p. A1557-A1562 (1964).
- [120] J.R. Fermin, et al., *Ferromagnetic resonance linewidth and anisotropy dispersions in thin Fe films*. Journal of Applied Physics. **85** 10: p. 7316-7320 (1999).
- [121] B. Heinrich and Frait Z., *Temperature dependence of the fmr linewidth of iron single-crystal platelets*. physica status solidi (b). **16** 1: p. K11-K14 (1966).
- [122] V. Kamberský, *On the landau–lifshitz relaxation in ferromagnetic metals*. Canadian Journal of Physics. **48** 24: p. 2906-2911 (1970).
- [123] F. Bensch, Moosbühler R., and Bayreuther G., *Onset of magnetic anisotropy in epitaxial Fe films on GaAs(001)*. Journal of Applied Physics. **91** 10 (2002).
- [124] M. Brockmann, et al., *In-plane volume and interface magnetic anisotropies in epitaxial Fe films on GaAs(0 0 1)*. Journal of Magnetism and Magnetic Materials. **198**: p. 384-386 (1999).
- [125] G. Bayreuther, et al., *Magnetocrystalline volume and interface anisotropies in epitaxial films: Universal relation and néel’s model (invited)*. Journal of Applied Physics. **93** 10: p. 8230-8235 (2003).
- [126] T.L. Monchesky, et al., *Magneto-resistance and magnetic properties of Fe/cu/Fe/GaAs(100)*. Physical Review B. **60** 14: p. 10242-10251 (1999).
- [127] K. Zakeri, et al., *Temperature-dependent correlation of magnetic anisotropy and magnetization in Fe monolayers on $\{4\times 6\}$ GaAs(001)*. Journal of Magnetism and Magnetic Materials. **316** 2: p. e334-e337 (2007).
- [128] R. Arias and Mills D.L., *Theory of roughness-induced anisotropy in ferromagnetic films: The dipolar mechanism*. Physical Review B. **59** 18: p. 11871-11881 (1999).
- [129] M.O. Liedke, et al., *Magnetic anisotropy engineering: Single-crystalline Fe films on ion eroded ripple surfaces*. Applied Physics Letters. **100** 24: p. 242405 (2012).
- [130] C. Kittel, *Introduction to solid state physics*. (1996).

- [131] C. Tomaz, *In situ ferromagnetische resonanz an Fe-basierten monolagen auf GaAs(011) und (001)*, in *Fachbereich Physik*, Universität Duisburg-Essen: Duisburg. (2007).

12 List of publications and conference contributions

Babli Bhagat, Anna Semisalova, Ralf Meckenstock, Michael Farle, *Reversal of uniaxial magnetic anisotropy in Fe/GaAs (110) films driven by surface relaxation: An in situ ferromagnetic resonance study*, 2020. AIP Advances **10**, 075219

DOI: <https://doi.org/10.1063/5.0004261>

Babli Bhagat, Tanja Strusch, Michael Farle, Florian M. Römer (2018). *Influence of substrate doping on spin pumping in Pt\Ag\Fe\GaAs[110] heterostructure*, talk presented at 2018 DPG spring Conference, Berlin, Germany.

Babli Bhagat, Ralf Meckenstock, Michael Farle (2019). *In-situ study of Fe on GaAs (100) and GaAs (110)*, talk presented at 2019 DPG spring conference, Regensburg, Germany.

Babli Bhagat, Ralf Meckenstock, Anna Semisalova, Michael Farle (2019). *Comparative study of magnetic stability of Fe on GaAs (100) and GaAs (110) using in-situ FMR*, poster presented at the SpinS Workshop 2019, Mulheim a. d. Ruhr, Germany.

Babli Bhagat, Anna Semisalova, Ralf Meckenstock, Michael Farle (2019). *Magnetic stability of uncapped Fe on GaAs (100) and GaAs (110) in ultrahigh vacuum*, poster presented at CENIDE annual celebration, Essen, Germany.

DuEPublico

Duisburg-Essen Publications online

UNIVERSITÄT
DUISBURG
ESSEN

Offen im Denken

ub | universitäts
bibliothek

Diese Dissertation wird via DuEPublico, dem Dokumenten- und Publikationsserver der Universität Duisburg-Essen, zur Verfügung gestellt und liegt auch als Print-Version vor.

DOI: 10.17185/duepublico/77553

URN: urn:nbn:de:hbz:465-20240228-161652-8

Alle Rechte vorbehalten.